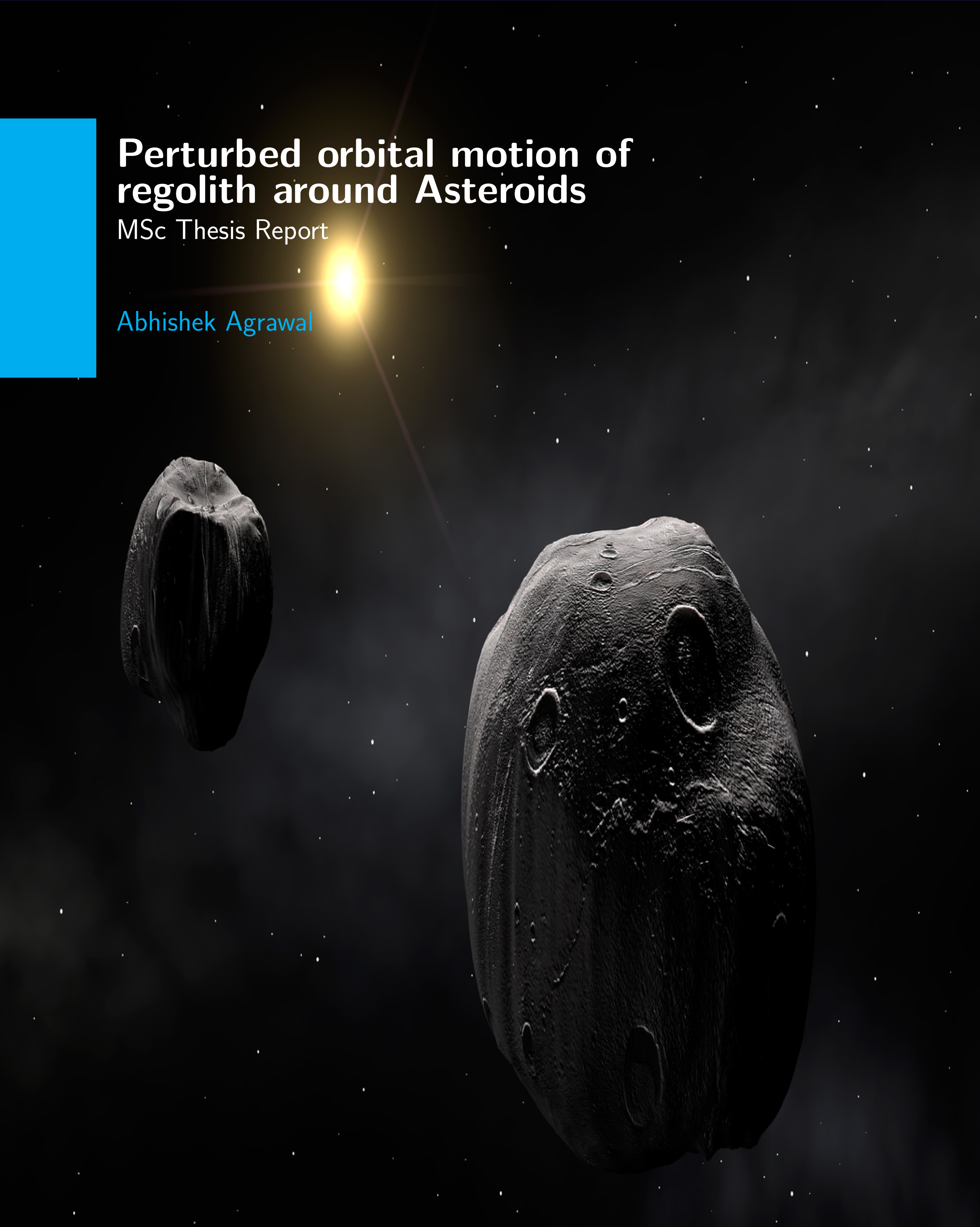

Perturbed orbital motion of regolith around Asteroids

MSc Thesis Report

Abhishek Agrawal

TU Delft
Delft University of Technology
Challenge the future

PERTURBED ORBITAL MOTION OF REGOLITH AROUND ASTEROIDS

MSc Thesis Report

by

ABHISHEK AGRAWAL

to obtain the degree of Master of Science
at the Delft University of Technology.

Student number:	4416600	
Thesis committee:	Dr. Ir. D.J. Scheeres,	University of Colorado, Boulder, supervisor
	Ir. R. Noomen,	TU Delft, supervisor
	Dr. Ir. ,	TU Delft
	Ir. ,	TU Delft

An electronic version of this thesis is available at `http://repository.tudelft.nl/`.

TU Delft

Cover image credit: Adopted from European Southern Observatory. Artist's Impression of the binary asteroid Antiope.

"If you wish to make an apple pie from scratch, you must first invent the universe."
Carl Sagan

PREFACE

After 45 years since the day man landed on the Moon, mankind created history, yet again. For the first time ever, a spacecraft was put into an orbit around a comet and a lander was deployed to its surface. This was the Rosetta mission; launched in March 2004, the spacecraft took an astonishing 10 years to travel to the comet 67P/Churyumov-Gerasimenko, finally arriving at the comet in August 2014. This is an immense achievement for the scientists and engineers involved in the Rosetta mission because space missions to small irregular bodies in our solar system, both comets and asteroids, pose significant dynamical challenges. For scientists, missions to comets and asteroids are of great interest since in-situ exploration of these small bodies can provide insight into the birth of our Solar System and answer some very important and fundamental questions such as those about the origins of life on Earth. Now even the private space industry is interested in these small bodies, such as in mining the vast reserves of untapped natural resources within the small bodies. For a student, designing and assessing orbits around a small irregular body, and in our case an asteroid, turns out to be one of the toughest problems in astrodynamics, making it a perfect research topic for an MSc Thesis.

This report serves to be a *Literature Study* in the framework of the Master's program at the Faculty of Aerospace Engineering, Delft University of Technology. It paves way for the upcoming thesis project, where the actual research work shall be carried out. I am grateful I could do this literature study under the supervision of my supervisor Ir. Ron Noomen and with support from Dr. Jinglang Feng. Their experience in the subject matter has been of tremendous help to me. In writing this report, I have tried my very best to ensure that the material in the report is presented in a manner which is pleasant to read and understand. I hope you can gain some valuable knowledge from reading this report.

Abhishek Agrawal
Delft, August 2016

CONTENTS

List of Symbols

Roman

Symbol	Units	Description
a, b, c	m	Semi-axes of reference ellipsoid (ellipsoidal harmonics gravity potential model)
$\mathcal{B}$	-	Collection of all discrete mass distributions
C	-	Spherical harmonics expansion coefficient
E	-	Lamé function of first kind
$\boldsymbol{E}$	-	Edge Dyad in the polyhedron potential model
F	-	Lamé function of second kind
$\boldsymbol{F}$	-	Facet dyad in the polyhedron potential model
$\mathcal{G}$	$m^3 g^{-1} s^{-2}$	Universal Gravitational constant
L_e	-	Per-edge factor in polyhedron model
$\hat{\boldsymbol{n}}$	-	Unit normal vector
$\hat{\boldsymbol{n}}_e^f$	-	Unit normal vector to edge e of facet f of a polyhedron
P	-	Associated Legendre functions
$\mathbf{P}$	-	Field point in polyhedron potential model
r	m	Distance
$\vec{\boldsymbol{r}}$	m	Position vector
$\vec{\boldsymbol{r}}_i^f$	m	Vector from field point to vertices of a facet in polyhedron model
$\vec{\boldsymbol{r}}_i^e$	m	Vector from field point to vertices of an edge in polyhedron model
$\vec{\boldsymbol{r}}_e$, $\vec{\boldsymbol{r}}_f$	m	Vector from any point on edge e or f, respectively, to the field point in polyhedron model
R_D, R_F	-	Carlson elliptic integral functions
s	m	Conic equation parameter
S	-	Spherical harmonics expansion coefficient
t	s	Time
u	m	Parameter in equation for family of confocal quadrics to an ellipsoid (CDE potential model)

u_1, u_2, u_3	m	Real valued and unequal roots to the equation for family of confocal quadrics to an ellipsoid (CDE potential model)
U	m^2/s^2	Gravitational potential
U_1, U_2, U_3, U_4	m^2/s^2	CDE gravitational potential split in 4 parts
U_*	m/s^2	Gravitational acceleration component where ($* = x, y, z$)
v	m	Substitution parameter to get standard Carlson elliptic integral
v	m/s	Velocity
$\vec{\boldsymbol{v}}$	m/s	Velocity vector
V	m^3	Volume
x	m	Cartesian coordinate x
y	m	Cartesian coordinate y
z	m	Cartesian coordinate z

GREEK

Symbol	Units	Description
α	-	Ellipsoidal harmonics expansion coefficient
α, β, γ	m	Semi-major axes of an ellipsoid (CDE potential model)
δ	deg	Latitude (spherical harmonics gravitational potential model)
Δ	-	Function in CDE potential model
λ	deg	Longitude (spherical harmonics gravitational potential model)
$\lambda_1, \lambda_2, \lambda_3$	m	Ellipsoidal coordinates
λ_1^{ref}	m	Largest semi-major axis of reference ellipsoid (ellipsoidal harmonics gravity potential model)
$\lambda(\vec{\boldsymbol{r}})$ or λ	m	Real valued parameter; defines a confocal ellipsoid in the CDE potential model
μ	m^3/s^2	Gravitational parameter
ω	rad/s	Asteroid rotation rate or angular velocity
ω_f	-	Per-facet factor in the polyhedron model
$\vec{\boldsymbol{\omega}}$	rad/s	Angular velocity vector
ϕ_B^I	-	Rotating frame (ARF) to Inertial frame (AIF) transformation matrix

ϕ_I^B	-	Inertial frame (AIF) to Rotating frame (ARF) transformation matrix
ϕ	-	Function in CDE potential model
ρ	m	Distance to a discrete mass distribution
$\vec{\boldsymbol{\rho}}$	m	Distance vector to a discrete mass distribution
σ	kg/m^3	Density in polyhedron model
θ	deg	Rotating angle between the Asteroid-centric inertial and Rotating frame
ϑ	deg	Longitude of Sun with respect to the asteroid

Subscripts & Superscripts

Symbol	**Description**
B	Asteroid-centric Rotating frame (ARF)
e	Edge of a facet in a polyhedron shape model
f,f'	Facet or face of a polyhedron shape model
I	Asteroid-centric Inertial frame (AIF)
l	Degree of spherical harmonics expansion
m	Order of spherical harmonics expansion
n	Degree of ellipsoidal harmonics expansion
p	Order of ellipsoidal harmonics expansion
P	Particle or Regolith
S	Sun
x	Vector component along x-axis
y	Vector component along y-axis
z	Vector component along z-axis
$*_I^B$	AIF *'quantity'* expressed in ARF components
$*_B^I$	ARF *'quantity'* expressed in AIF components

List of Acronyms

AIF Asteroid-Centric Inertial Frame

ARF Asteroid-Centric Rotating Frame

AU Astronomical Unit

CCW Counter-Clockwise

CDE Constant Density Ellipsoid

CKBO Classical Kuiper-Belt Objects

EHAO Extremely-High Altitude Orbit

EOM Equations Of Motion

ESA European Space Agency

HAO High Altitude Orbit

JAXA Japan Aerospace Exploration Agency

LAF Low-Altitude Flyover

LAO Low Altitude Orbit

MAB Main Asteroid Belt

MAO Medium Altitude Orbit

MBO Main-Belt Objects

NAOS Near-Asteroid Orbit Simulator

NASA National Aeronautics and Space Administration

NEA Near-Earth Asteroids

NEAR Near Earth Asteroid Rendezvous

NEO Near-Earth Objects

OSIRIS-REx Origins, Spectral Interpretation, Resource Identification, Security, Regolith Explorer

SCI Small Carry-on Impactor

SDO Scattered Disk Objects

SF Surface Frame

SKG Strategic Knowledge Gap

SRP Solar Radiation Pressure

STBE Solar Third Body Effect

TAG Touch-And-Go

TNO Trans-Neptunian Objects

TUDAT Technische Universiteit Delft Astrodynamics Toolbox

UHAO Ultra-High Altitude Orbit

1

INTRODUCTION

At the dawn of the nineteenth century, Italian astronomer Giuseppe Piazzi was engrossed in observing the Taurus constellation to update a star catalog. On January 1 1801, atop the Palermo observatory in Sicily, he observed a light which wasn't mentioned in the catalog. He followed the strange light for a few more nights, eventually realizing that he had discovered a small planet between Mars and Jupiter. He named the minor planet *Ceres* and it became the first of its kind to be discovered by humans. Broadly speaking, it became the first *asteroid* to ever be discovered (Cunningham 2016). Soon after this discovery, three other minor planets were discovered in the gap between Mars and Jupiter. *Pallas* was discovered in 1802, followed by *Juno* in 1804, and finally *Vesta* in 1807. After the discovery of *Ceres* and *Pallas*, renowned astronomer William Herschel realized that these are a new species of celestial bodies and proposed to call them *asteroids* (which in Greek meant *star-like*) instead of *minor planets*. For nearly 40 years after the discovery of *Vesta*, no additional discoveries were made. Then once again in the second half of the nineteenth century, astronomers started discovering more and more of these asteroids until they realized that there is a whole *belt* of it between Mars and Jupiter (Bottke 2002).

Asteroids are rocky, airless celestial bodies in our Solar System that orbit the Sun and are quite small in size compared to the planets. They can be viewed as remnants of the processes that formed the inner planets of our Solar System (NASA, "Asteroids: In depth"). Asteroids are mostly irregularly shaped with a few exceptions, like Ceres, that have a nearly spherical shape. Figure 1.1 provides a view on the different morphologies of asteroids (NASA, "Asteroids: In depth"). They are typically categorized based on their location in the Solar System. A large number of asteroids are found in the region between Mars and Jupiter and are called as MBO (Main-Belt Objects). A relatively smaller number of asteroids, called NEA (Near-Earth Asteroids), have orbits that are very close to and/or crosses the heliocentric orbit of Earth. Asteroids at the L_4 and L_5 Lagrange points of Jupiter, sharing its orbit around the Sun, are termed as *Trojans*. Then we have *Centaurs*, asteroids whose orbit lies between or crosses that of the Giant planets in our Solar System. The fifth and the final category is of the TNO (Trans-Neptunian Objects) i.e. asteroids with orbit beyond that of Neptune and reaching as far as the Oort cloud (De Pater et al. 2015). The distribution of asteroids in the inner and outer Solar system is shown in Figure 1.2.

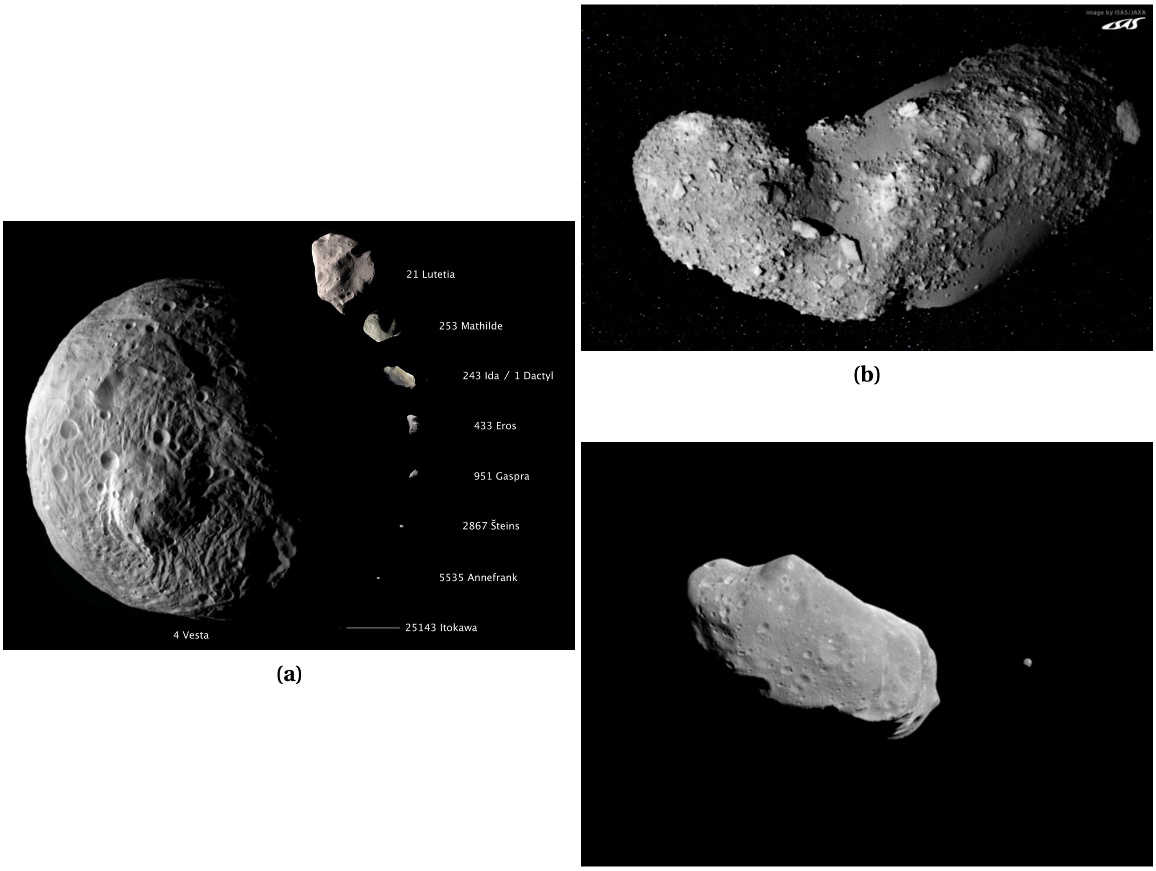

(a) **(b)** **(c)**

Figure 1.1: Satellite imagery depicting different morphologies of asteroids. (a) depicts the size and shape variations amongst a few known asteroids, (b) asteroid Itokawa with its rocky and rough surface, (c) asteroid Ida with its moon Dactyl orbiting around it (NASA, "Asteroids: In depth").

Due to their extremely small sizes, asteroids can not have high internal pressures and temperatures which means that they could have potentially preserved the early chemistry of our Solar System (Kubota et al. 2006). This makes them a valuable source for us to understand about the history and origin of our Solar System. It is hypothesized that during the early years of Earth's formation, carbon-based molecules and other volatile materials which serve as the basic building-blocks of life, could have been delivered to Earth through asteroid impacts (*JPL, "SSD"*). Finally, some asteroid types are rich in resources and contain vast supplies of precious metals (Kargel 1994) and water (Morbidelli et al. 2000), which could potentially be mined and used to aid further exploration and colonization of our Solar System (*JPL, "SSD"*). Thus in light of this, asteroid exploration, both in-situ and ex-situ, have gained significant importance not only amongst the scientific community but amongst the private space industry as well, with more and more future missions being planned for these small bodies. The NEAR (Near Earth Asteroid Rendezvous) spacecraft launched by NASA (National Aeronautics and Space Administration) in 1996, as part of their *Discovery* program, became the first spacecraft in history to orbit an asteroid (433 Eros) and eventually land on it. The spacecraft spent almost a year around Eros, providing extended and comprehensive observations of surface morphology, shape, internal structure and physical properties of the asteroid (Prockter et al. 2002). The Hayabusa mission (formerly MUSES-C) by JAXA (Japan Aerospace Exploration Agency) entered into orbit around asteroid Itokawa in 2005 and became the first mission to sample the surface of an asteroid, which were subsequently returned to Earth for analysis in 2010 (Yano et al. 2006). These missions have substantially increased our knowledge about the small bodies in our Solar System.

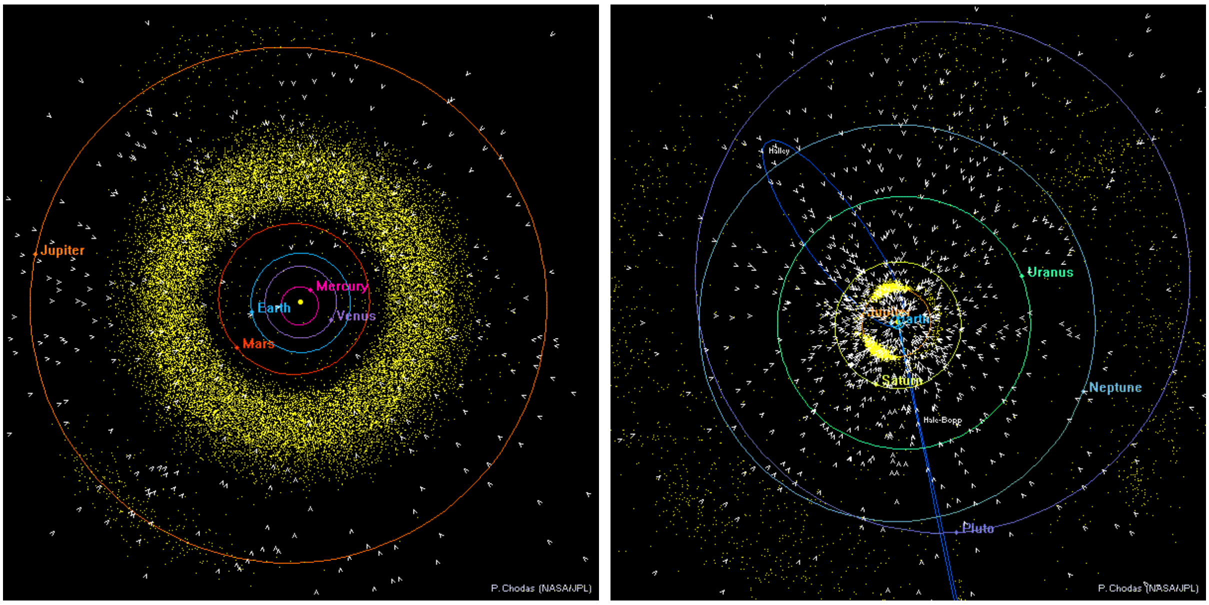

(a) **(b)**

Figure 1.2: Distribution of asteroids in (a) inner Solar System and (b) outer Solar System. Asteroid locations are shown by yellow-colored dots whereas the white-colored wedges pointing towards the Sun represent the comets. The diagrams are based on the small-bodies cataloged up until November 2016 (*JPL, "SSD"*).

Two more asteroid rendezvous missions launched quite recently, are however, of particular interest to this thesis. Following the success of Hayabusa, JAXA launched another sample return mission called Hayabusa-2 to asteroid *1999 JU3*, scheduled to be in orbit around it by mid-2018. It will perform a 1.5 year long close-proximity operation at the asteroid that includes surface sample acquisition, which will eventually be returned to Earth in a capsule, and a 2 [m] wide cratering event to observe the sub-surface (Tsuda et al. 2013). The OSIRIS-REx (Origins, Spectral Interpretation, Resource Identification, Security, Regolith Explorer) mission by NASA, directed towards asteroid *Bennu* and scheduled to enter into an orbit around it in late-2018, will also retrieve a surface sample and return it back to Earth. It will employ a TAG (Touch-And-Go) maneuver to acquire a sample within a 1.5 month long scheduled sampling period (Berry et al. 2013). Both the missions are aiming to find out if organic material, volatiles and water itself were brought to Earth by such asteroids. These mission employ techniques for sample acquisition that could potentially disturb the state of regolith on the surface of the asteroid and loft it into an orbit. For the success of these and all other missions in the future, it is imperative to understand the complex dynamical environment around asteroids, not only for spacecrafts, but also for the orbital motion of lofted regolith. NASA has identified the acquisition of such information as a SKG (Strategic Knowledge Gap) for NEO (Near-Earth Objects), specifically article *III-A-1: Expected particulate environment due to impact ejecta* in NASA, "SKG".

The study of lofted regolith around an asteroid is by no means a new research topic. In the studies done previously (Richter et al. 1995; Lee 1996; Scheeres et al. 1996; Scheeres et al. 2000; Korycansky et al. 2004; Yárnoz et al. 2014), we have witnessed certain minor drawbacks such as not always accounting for gravity and Solar perturbations together, or using an approximated analytical method to understand the dynamical environment that falls short on obtaining the entire spectra of initial conditions that could lead to different final outcomes (re-impact, escape or temporary capture) for lofted regolith, or not considering different size and density for the lofted regolith, and finally not considering the local direction with respect to a rotating asteroid in which the regolith is ejected. This thesis, thus, aims to include all of these shortfalls in a single study, and by using numerical simulation techniques, to add more fidelity in understanding what happens to regolith when it is lofted from the surface of an asteroid.

The study of orbiting regolith is important for understanding the displacement of material on surface of the asteroid in case of natural or spacecraft induced impact cratering events. In case of the latter, the ejecta from the impact cratering event could pose serious threat to spacecraft and/or its instruments. By knowing the orbital behavior of regolith in advance, mission designers can make informed decisions on the trajectory design of spacecraft to avoid or reduce failure scenarios. Another important benefit that comes from a study like this is in the field of asteroid mining, whereby the regolith's orbital motion and final fate can be exploited to sort different materials in real time. The results from this thesis will thus aid mission designers in planning future asteroid missions and in answering the following research question:

Can we explain the orbital behavior and eventual fate of lofted regolith around an asteroid in presence of gravity and Solar perturbations?

1.1 GUIDE TO READ THIS REPORT

This section will provide a guide to read this thesis report efficiently, for novice to experienced space engineers, to ensure relevant knowledge is not missed. This is just a guide to help you but you are more than welcome to read the report in whatever manner you deem necessary.

Part I

Motivation

2

HERITAGE

In the past, there have been multiple spacecraft missions to the small bodies in our Solar System which have collectively increased our understanding about them. While a large majority of these have been asteroid fly-by scenarios, a few have also been rendezvous missions (ESA 2014). This chapter will provide an overview on few of these missions followed by a brief literature review which shall be of interest to the thesis at hand. This will help us in justifying the research objectives mentioned in Chapter 3. Section 2.1 will discuss the asteroid rendezvous missions which have already taken place, Section 2.2 will discuss future rendezvous missions, and finally, Section 2.3 will discuss the state-of-the-art.

2.1 PAST MISSIONS

In all the history of space exploration there have been only three spacecraft missions that have rendezvoused with asteroids. In chronological order these are: NASA's NEAR-Shoemaker mission to asteroid Eros, JAXA's Hayabusa mission to asteroid Itokawa, and NASA's Dawn mission to asteroids Vesta and Ceres (Scheeres 2016). Out of these, only NEAR and Hayabusa had direct contact with the small bodies and acquired high-resolution imagery of surface regolith.

2.1.1 NEAR-SHOEMAKER

The NEAR-Shoemaker (henceforth NEAR) mission was launched in 1996 and rendezvoused with Eros in 2000. Its operational phase around the asteroid continued for about a year during which it obtained several high-resolution images of the surface and collected comprehensive measurements to estimate its internal mass distribution, shape model, gravity and spin state amongst other observations (Scheeres 2016). The bulk density of Eros was estimated to be $2.67 \pm 0.03 [g/cm^3]$ and its mass to be $(6.6904 \pm 0.003) \times 10^{15} [kg]$. The rotation state was estimated to be 1639.38922 ± 0.00015 [deg/day] which gives a rotational period of about 5.27 [hrs] (Miller et al. 2002). On 25 October 2000, NEAR executed a LAF (Low-Altitude Flyover) over Eros in which it acquired several high-resolution images that helped in understanding the surface morphology. The images confirmed the existence of a substantial amount of regolith on the surface with a typical thickness value of tens of metres over the bedrock, except of course on steep slopes. The regolith was found to be highly complex, in that it varied from fine material to metre-sized ejecta blocks (Veverka et al. 2001a). Robinson et al. 2001 estimates the size of the finer regolith to be around 1.0 [cm] or smaller from images that had a resolution of 1.2 [cm] per pixel. Figure 2.1 depicts the regolith morphology in one of the high-resolution imaging sequences from the LAF (Veverka et al. 2001b).

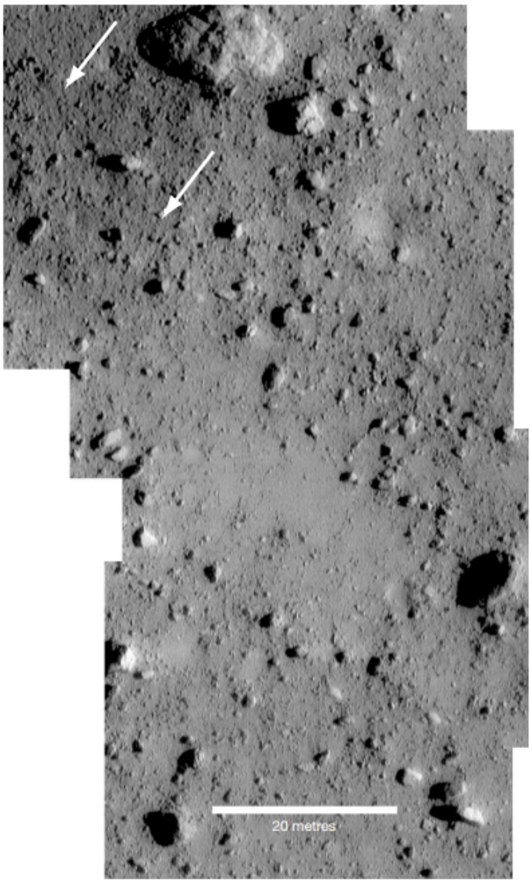

Figure 2.1: Mosaic of high-resolution images depicting the nature of regolith on the surface of Eros (Veverka et al. 2001b).

2.1.2 HAYABUSA

The Hayabusa spacecraft was launched by JAXA in 2003 and it arrived at asteroid Itokawa in 2005. After arrival, it performed close-proximity operations around the asteroid for approximately 3 months during which several measurements were taken to estimate the shape, mass, topography and elemental composition of the asteroid. During this period, the spacecraft also collected samples from the surface of the asteroid that were eventually returned back to Earth in 2010. The measurements at Itokawa estimated its mass to be 3.51×10^{10} [kg] and its bulk density to be 1.9 ± 0.13 [g/cm^3] (Fujiwara et al. 2006).

Two distinct types of terrains can be recognized on Itokawa, one which is rough and rich in boulders and the other which is smooth and mostly flat. This distinction can easily be seen in Figure 2.2. The smooth regolith regions, that account for approximately 20% of Itokawa's surface, composed of fragmented debris with grain sizes ranging from sub-centimetre to centimetre scales. One of the smooth regolith regions, called Muses Sea and from where the sample was also acquired, even consisted of a few metre-sized boulders that were hypothesized to have landed in the region as secondary ejecta (Miyamoto et al. 2006). The rougher terrain on Itokawa, which has a very sharp boundary with the smoother regolith filled regions (as evident in Figure 2.2), consists of boulders that range upto tens of metres in size (Fujiwara et al. 2006).

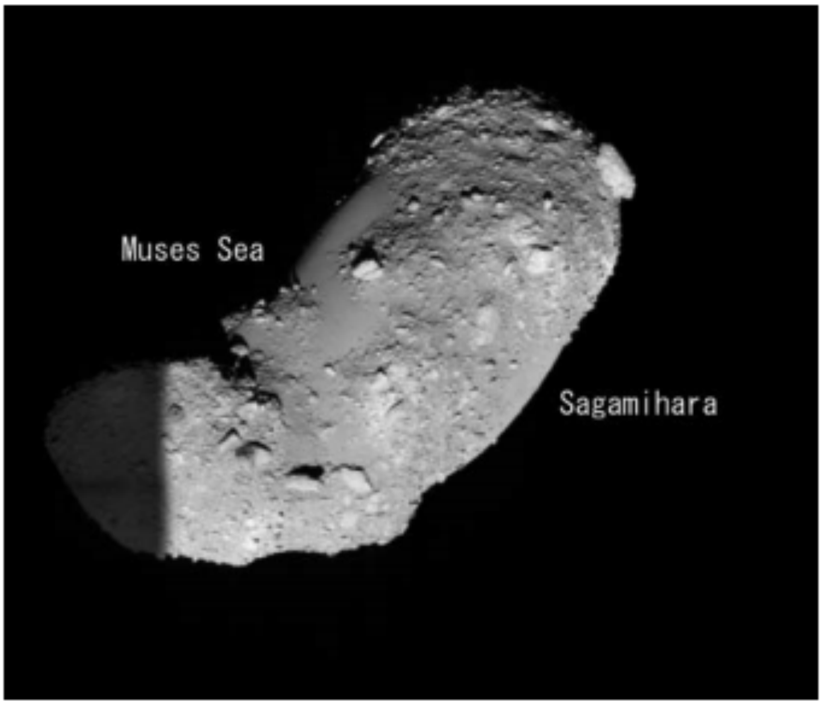

Figure 2.2: Image of Itokawa taken from a 7 [km] altitude depicting the nature of regolith on its surface. Muses Sea and Sagamihara are the two distinct smooth regolith regions on the asteroid (Fujiwara et al. 2006).

Hayabusa employed an *impact sampling mechanism* that would work across various types of terrains, from hard bedrock to fine regolith. The spacecraft consisted of a long cylindrical sampling horn with a conical tip. When the tip of the horn touched the surface of the asteroid, the deformation in the horn's fabric was detected by a laser range finder and within 0.3 [s] of this event, a 5.0 [g] projectile was fired towards the surface with a velocity of 300 [m/s] and the resultant ejecta was collected by the sampler (Yano et al. 2004). Yano et al. 2006 presents data from the sampling experiments that were performed on ground in 1g and micro-gravity environments. The experiments revealed that, for the projectile hitting at normal impact angles in micro-gravity, the impact ejecta mass of particles greater than 1.0 [cm] ranged from 2 - 11 [g] whereas for particles less than 1.0 [mm] the ejecta mass ranged from 100 - 10000 [g]. The impact target consisted of various analog materials from glass beads to lunar regolith simulant and an experiment like is a nice indicator of how artificial impact events can displace significant amount of fragmented debris on an asteroid.

2.2 FUTURE MISSIONS

We will now discuss two missions, Hayabusa-2 by JAXA and OSIRIS-REx by NASA. Both are currently en route to their respective target asteroids and after orbit insertion, they shall perform operations to collect surface samples.

2.2.1 HAYABUSA-2

Hayabusa-2 is the second asteroid sample return mission by JAXA, which to a significant extent, shares the successful technical legacy of Hayabusa. The target asteroid of the former is *1999 JU3* which is suspected to contain organic matter and hydrated minerals (Tsuda et al. 2013). The shape model of the asteroid, also designated as *Ryugu*, is shown in Figure 2.3 (Müller et al. 2017). A successful sample return from this asteroid may thus help us in understanding the origin of life and/or water on Earth. The spacecraft will enter into an orbit around its target by mid-2018, after which it will perform close-proximity operations for 1.5 years. The mission will entail 3 touchdowns for sample acquisition and a cratering event to observe the subsurface of the asteroid. The sampling mechanism is based on that of Hayabusa and each sampling attempt has the potential to acquire samples in the order of 100 [mg]. The samples are sealed-off and transported back to Earth in a re-entry capsule. The cratering operation is performed by a SCI (Small Carry-on Impactor). The SCI is deployed by the spacecraft at an altitude of 500 [m] and after a preset time, a detonation accelerates it to about 2 [km/s] prior to impact. It is estimated that this will result in a crater of about 2 [m] wide. Prior to the detonation of SCI, the spacecraft will move to a safe location on the opposite side of the asteroid from the impact point to avoid damage from impact ejecta and/or debris from the detonation. Apart from these, the spacecraft will perform other in-situ operations to characterize the asteroid and will also deploy a lander and three miniature rovers for technology demonstration (Tsuda et al. 2013).

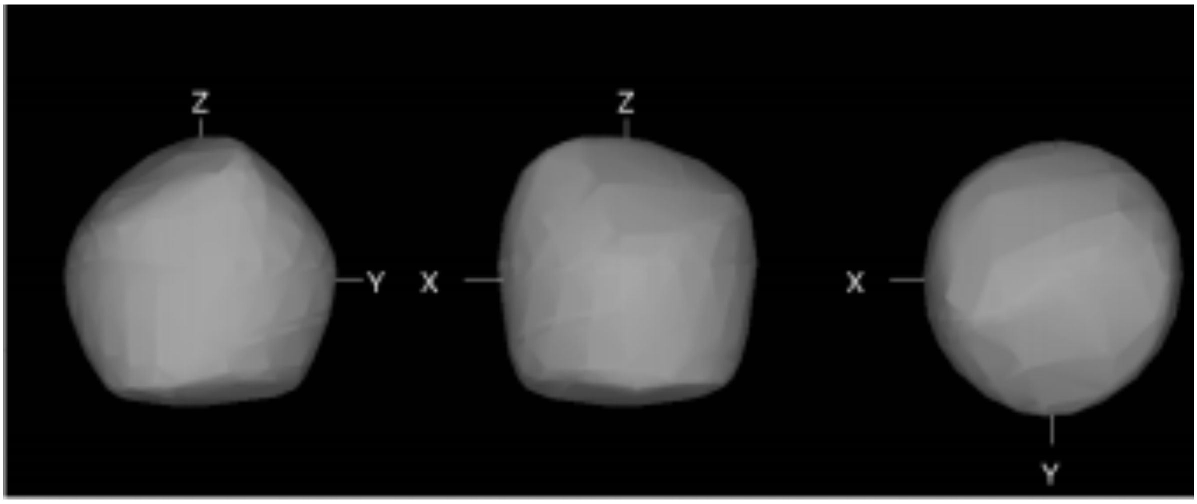

Figure 2.3: Ryugu shape model as estimated from the observations made by Herschel Space Observatory, supported by several ground-based measurements and data from other space-based assets (Müller et al. 2017).

2.2.2 OSIRIS-REx

OSIRIS-REx is part of NASA's New Frontiers program and will travel to NEA 1999 RQ_{36}, also known as Bennu. The shape model of the asteroid is shown in Figure 2.4 (Lauretta et al. 2015). The mission, amongst other scientific objectives, will return a regolith sample back to Earth that may provide insight into the initial states of planetary formation as well as answer questions on the origins of life. Since Bennu is a NEA, the sample collection and subsequent analysis will provide us information on asteroids that could potentially impact Earth. The spacecraft was launched in 2016 and is expected to reach its target by the end of 2018 (Berry et al. 2013). The asteroid has a semi-major axis of 1.126 [AU] which makes it an easily accessible asteroid as far as distance is concerned. But more than that, Bennu falls under the category of asteroids that are rich in volatiles and could potentially be related to objects that brought the seeds of life to Earth. Initial observations of Bennu through ground based telescopes, the Spitzer Telescope, the Arecibo Observatory and other assets revealed an abundance of regolith on the surface with grain sizes ranging from 4 - 8 [mm]. OSIRIS-REx will acquire the regolith sample using a TAG mechanism which uses pressurized Nitrogen gas to force the loosely held regolith into a collection chamber. The sampling will occur in 2020 and it will be retrieved on Earth in 2023 (Lauretta et al. 2012).

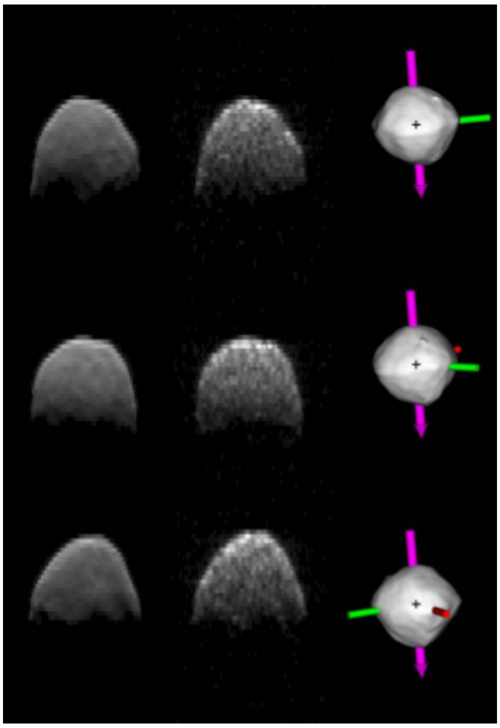

Figure 2.4: Bennu's shape as observed from the radar data collected by the Goldstone and Arecibo observatories (shown in middle column of the image). The left column displays the model that provides the best fit to the radar data and the right column shows the final estimated 3D model of Bennu as it would appear in the sky (Lauretta et al. 2015).

2.3 STATE OF THE ART / LITERATURE REVIEW

In this section we shall discuss a few research papers relevant to this thesis; the techniques they applied to understand the orbital behavior of impact ejecta and the shortcomings of these studies.

A good starting point to understand the topic at hand is provided by Scheeres et al. 2002. It reviews the gravity and perturbing force models along with the dynamical equations of motion for a particle in orbit around an asteroid & the model for generating initial conditions to launch ejecta from the surface of an asteroid. It also mentions about existing analytical methods to compute guaranteed escape and re-impact speeds for impact ejecta i.e. speeds at which particles would immediately escape or re-impact after being launched. Scheeres et al. 2002 also discusses the various numerical and analytical methods that have been used in literature for analyzing the motion of particles that stay in a pseudo-stable orbits for extended periods of time before meeting their final fate. It also presents various mechanisms that have been hypothesized for the capture-case scenario i.e. particles that stay in orbit around asteroids for a relatively long time, from hundreds of days to several asteroid years. The analysis of these capture orbits, in particular, has been done by considering the Solar perturbations and irregular gravity effects of the asteroid but always in isolation.

Richter et al. 1995 provides an analytical method to solve for the motion of particles around a non-rotating, spherical cometary nuclei which is on an eccentric, heliocentric orbit. In their paper, they ignore Solar tidal effects and assume that the particle motion around a homogeneous spherical body would experience weak perturbations from SRP (Solar Radiation Pressure). They give averaged equations for the variation of eccentricity and angular momentum vectors as a function of the true anomaly of comet around the Sun. The paper also discusses the limitations and validity of using their analytical approximation as well as the conditions for collision-free orbits for small and large dust particles around the comet. Although the study conducted by Richter et al. 1995 is for comets, it can be extended to asteroids as well and has been used by Morrow et al. 2001 for analyzing solar sail powered trajectories around them. Lee 1996 discusses the electrostatic levitation of dust particles from the surface of an asteroid. It uses two electrostatic field production methods used in the study of dust levitation on moon, and applies them to the case of an asteroid. The study does not involve the orbital motion of dust particles but it does provide conditions which could cause the dust particle to escape in the event of electrostatic levitation.

Scheeres et al. 1996 provides an extremely detailed and systematic study of particle dynamics close to the surface of asteroid Castalia. They include the effect of the irregular shape of the asteroid on orbital dynamics by using a spherical harmonics model of degree and order upto 4 in simulating the gravity potential. They also derive analytical results for computation of guaranteed return and escape speeds as a function of location of particle on the surface of the asteroid. The paper employs dynamical systems theory and investigates the use of stable manifolds associated with orbits around equilibrium points and intersecting the surface of the asteroid, to obtain the initial launch conditions for the particle that will lead to a temporary stable orbit around the asteroid. Scheeres et al. 2000 applies the radiation pressure approximation method developed by Richter et al. 1995 to study the temporary capture of particles in an orbit around a comet but improves it to account for the comet's rotation as well. The results obtained from the analytical approximation are compared with the results from the numerical simulation wherein the latter accounts for other perturbations as well such as Solar Tidal effect and gravity field variations. The comparison showed that the radiation pressure approximation method by Richter et al. 1995 is qualitatively correct and can be used for statistical studies at the very least. They were also able to establish qualitative ranges on ejecta velocity and angles that result in capture orbits, an example of which is shown in Figure 2.5.

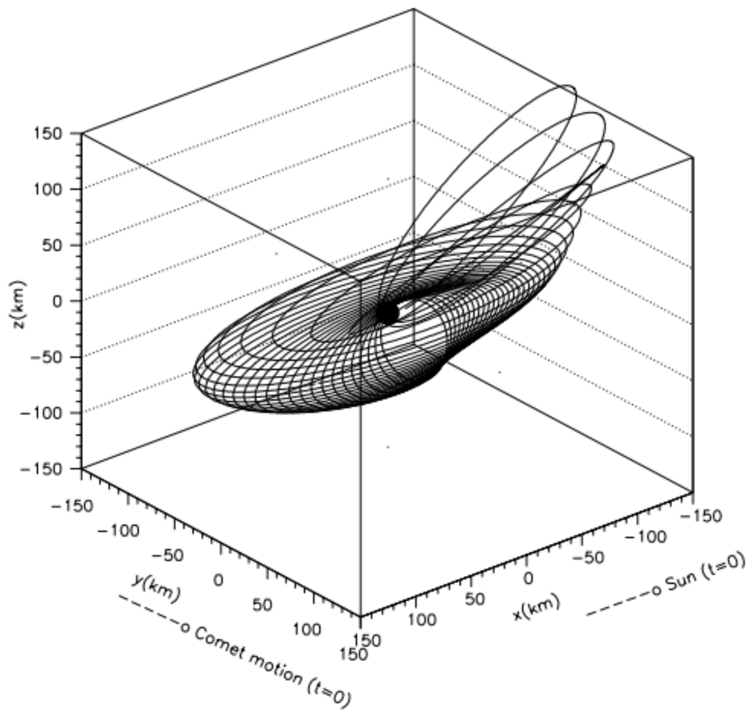

Figure 2.5: Example of single particle capture trajectory around comet Tempel-1 (Scheeres et al. 2000).

Korycansky et al. 2004 conducts a study to understand the distribution of impact ejecta and its connection with existing regolith on the surface of asteroid 433 Eros. The study involves the use of Monte Carlo simulation technique to observe the orbital evolution of a large number of test particles from randomly selected locations on the asteroid. They use a coarse polyhedron model of asteroid

Eros to model its gravitational field, thus accounting for gravity perturbations. However, the research does not account for perturbations from SRP. Yárnoz et al. 2014 studies the orbital motion of lofted regolith in the context of using Solar Radiation Pressure to passively sort asteroid material. They use semi-analytic methods to derive conditions that would cause regolith to either escape or re-impact the asteroid's surface. They make use of the radiation pressure approximation methodology developed by Richter et al. 1995 in their semi-analytical approach. However, the affect of an irregular shape of an asteroid, i.e. gravity perturbations, is not accounted for in their calculations.

In general, we witnessed minor drawbacks in these studies such as not always accounting for gravity and Solar perturbations together, or the derivation of an analytical solution which is not globally valid. Some studies involved both analytical and numerical methods for simulating orbital dynamics but even then the numerical approach was more for comparing the validity of the analytical solution and not as much for obtaining the full range of initial conditions that will lead to re-impact, escape or temporary capture of regolith around an asteroid. The affect of launch direction of regolith was also not considered in most of the studies, especially the ones that applied analytical methods. We have attempted to address these shortfalls to better understand the reasons for the complex orbital behavior of particles launched from the surface of an asteroid, by following a numerical simulations approach instead of an analytical approximation or a dynamical theory one (see Scheeres et al. 2002 for a brief discussion between the three methods for analyzing orbital behavior of asteroid ejecta). We have accounted for gravity and Solar perturbations while simulating trajectories for particles of different sizes and density. These perturbations have been considered in isolation as well as together to witness the effect of each individual perturbation on a particle trajectory. More details on the dynamics involved, the numerical simulator, and the methodology will be presented later in this report.

3

RESEARCH QUESTIONS & GOALS

The study of the dynamics of a particle, on or around an asteroid, can be broadly divided into three main regimes. The first regime involves the study of surface ejecta generation, from natural events such as interplanetary particle impacts, cratering by other asteroids & electrostatic dust levitation, or from space exploration events where the natural state of the regolith is disturbed by spacecraft sampling activities. The second regime involves the study of the subsequent orbital behavior of impact ejecta or lofted regolith under varying parameters such as launch conditions, asteroid rotational state & shape, regolith particle size and density, Solar phase etc. And finally, the third regime involves the study of particle dynamics when it re-impacts with the surface of the asteroid. This thesis will concern itself with the second regime of research, i.e., the natural orbital evolution of regolith lofted from an asteroid's surface.

As mentioned earlier in Chapter 1, understanding particulate environment around small-bodies has been identified by NASA as a strategic knowledge gap. Understanding and developing tools or knowledge to estimate the orbital behavior and final fate of lofted regolith with greater accuracy is important for future space exploration missions (see Section 2.2) that will involve direct interactions with asteroids, to avoid any damage to the spacecraft or surface robotic crew from orbiting particles. High-fidelity simulations of particulate motion can also help scientists in understanding the surface morphology of asteroids by helping them recreate cratering events. In Section 2.3, we highlighted the shortfalls in the research done on the topic so far and we identified a gap that needs to be filled, and hence, the following top level research question is set:

Can we explain the orbital behavior and eventual fate of lofted regolith around an asteroid in presence of gravity and Solar perturbations?

This top-level research question is divided into the following sub-questions that help in structuring the thesis:

1. Does the regolith, launched from different locations such as leading, trailing, longest and shortest edge of an asteroid, show characteristic differences with regard to its final fate?

2. Can clear demarcation be established between the re-impact, capture, and escape scenarios, for the lofted regolith, based solely on the initial conditions?

3. What causes the regolith to enter into a temporary capture orbit around the asteroid?

4. For the same launch conditions, how does the orbital behavior and final fate of the regolith differ for different particle sizes and densities?

5. For the same particle size and density, how does the orbital behavior and final fate change with different launch locations?

6. Can we establish a non-conservative analytical expression to determine guarantee escape speed in presence of perturbations?

7. Can we exploit the orbital behavior of lofted regolith for sorting material of different sizes and densities as an application for asteroid mining?

In order to answer these questions, the following main research goal is set:

Investigate the orbital motion of regolith launched from the surface of an asteroid using numerical simulations.

The sub-research goals are mentioned as follows:

1. Develop a modular and robust software tool that can propagate the trajectory of spherical particles around an asteroid for given initial conditions.

2. Develop software tools to plot and analyze numerical simulation results

3. Validate the software tools.

4. Perform simulations for particles launched from the asteroid's surface with different initial conditions, launch locations, and for different particle sizes & densities.

5. Perform qualitative and quantitative analysis on numerical simulation results.

6. Document results and inferences for thesis report and peer reviewed journal paper.

The vast majority of the time will be spent on designing the simulator and data processing & visualization tools (see Chapter 5), followed by their verification and validation (see Chapter 6). A relatively smaller time would then remain to perform the research and investigate the results, however the time remaining for this would be sufficient to answer all our research questions.

Part II

Dynamics Modeling & Simulator

4

Orbital dynamics around Asteroids

This chapter will focus on accurate modeling of the asteroid environment and the equations of motion of a particle around it in presence of gravitational and Solar perturbations.

4.1 Modeling Assumptions

The simulator designed as part of this research (see Chapter 5) involves some degree of approximation of the real-world dynamical environment around the asteroid. Every degree-of-freedom and complexity added to a simulator to resemble the real-world, will also act as a potential source of error. By designing a relatively simpler simulator, we can explain the characteristic behavior of regolith through fundamentals while keeping the sources of error to as low as possible. Ofcourse, we verify the simulator (see Chapter 6) but by including a higher degree of fidelity in the simulator, we increase the workload on the verification process as well, thereby reducing the scientific output in the end. Moreover, the current simulator and the results from it will act as a benchmark for a higher-fidelity simulator in the future. Thus, the approximations made in this thesis are mentioned as follows:

1. The asteroid body is modeled as a smooth triaxial ellipsoid to account for its non-uniform gravity. The triaxial model is chosen over the spherical and ellipsoidal harmonics approach because we want to study motion of regolith close to the surface of the asteroid; in particular the re-impact scenarios. This can't be done with the harmonics model as the gravitational potential diverges, within the circumscribing volume, from the true potential of an irregular body (see Section 4.3). We chose not to use a polyhedron model either, even though it can account for surface irregularities of an irregular body much better than the triaxial ellipsoid. This is because we want to decouple the fundamental phenomenon, associated with the motion of the regolith, from any effects of a truly irregular shape such as in the case of a polyhedron model.

2. Craters, surface depressions, mountains or any other terrain deformity on the asteroid is not considered in the simulation. The body is considered to have a uniform density. This is to simplify calculations of the gravitational acceleration.

3. The asteroid is rotating uniformly about its shortest axis. This is considered for simplicity and also because most Solar System bodies would dissipate energy to eventually enter a rotational state that is uniform and about its axis of maximum moment of inertia (Scheeres 2016). Hence, the approximation for the asteroid remains valid.

4. The regolith grains are assumed to be spherical in shape to simplify the SRP calculation as the cross-sectional area of a sphere would remain the same irrespective of its attitude. In addition to this, the grains are assumed to have albedo equal to one which means that any impinging Solar photons are completely reflected and this is done to account for maximum perturbation from SRP for a given location and Area-To-Mass ratio (see Section 4.4.2 for more details).

5. Multiple regolith particles are launched from a given location on the asteroid in the form of a cone to replicate ejecta from a cratering event. But all particles are assumed to be coming off from the same point, unlike that in the case of an actual cratering event. This is because the pretext of the thesis was that the regolith is lofted due to an activity from a spacecraft and such would result in relatively smaller craters (from artificial cratering events) or surface depressions. Thus assuming that all particles in this *"ejecta cone"* emerge from the same point on the asteroid is reasonable and simplifies the simulation.

6. The slant angle of the *"ejecta cone"* (henceforth the declination angle) from the local surface normal is kept constant at 45.0° (which is a middle value in the entire declination range from 0.0° - 90.0°). We want to consider a general case and not introduce another degree-of-freedom in terms of varying declination angles.

7. The loss of material and mass from the asteroid, when the regolith is lofted from the surface, is not modeled in the simulation since it is assumed that a very small amount of material will be displaced by a spacecraft activity. This assumption is based on the sample collected by the Hayabusa mission (see Section 2.1 and the references therein).

8. Interaction between individual regolith grain is not accounted for because we are simulating multiple particles being lofted at the same time and granular interaction on such a scale would be extremely complex and beyond the scope of this thesis.

9. Secondary motion of regolith, after re-impacting the surface is not modeled and it is assumed that the particles just come to a standstill.

10. The shadow region of the asteroid is not modeled which means that the solar perturbations are always acting on the regolith grain and this simplification was made since asteroids are extremely small compared to planets, and thus the orbiting particles wouldn't spend long periods of time in the shadow.

11. Perturbations are considered only from the Sun. SRP is important because regolith grains will have higher Area-To-Mass ratios, relative to a spacecraft, and so the radiation pressure would be significantly large for them. We model the third body attraction from the Sun (STBE (Solar Third Body Effect)) as well but not from any of the planets because we are assuming that the small body does not pass close to any planet, thus rendering the perturbations from them insignificant.

12. The apparent motion of the Sun around the asteroid is considered circular and in the equatorial plane of the asteroid and this was based on the orbital element measurements of all observed asteroids. Majority of these asteroids have small orbital eccentricities (Malhotra et al. 2016), quite a few of which have a nearly circular orbit. Jedicke et al. 1998 presents debiased measurements for the inclination of the MBO and shows that a large number of asteroids have near-zero inclinations.

4.2 REFERENCE FRAMES

Before describing the motion of regolith around the asteroid, its important to define the frames of reference with respect to which this motion is defined and the transformation of state vectors between these frames. We use two asteroid centric reference frames, both of which are depicted in Figure 4.1. Since we will be using a triaxial ellipsoid to model an asteroid (for details, see Section 4.3), the body-fixed rotating frame and the inertial frame with respect to this model are shown in Figures 4.2 and 4.3 respectively.

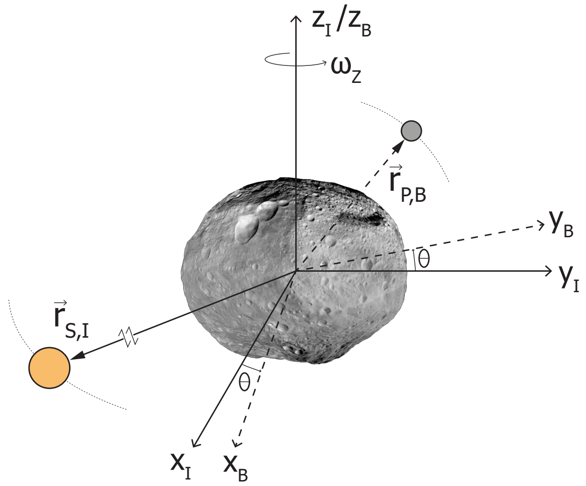

Figure 4.1: The diagram depicts two asteroid centric reference frames, one being Inertial (depicted by solid line and the subscript *I*) and the other being a body-fixed Rotating frame (denoted by dashed line and the subscript *B*). The position vector to a regolith particle is shown as $\vec{r}_{P,B}$, whereas the position vector to the Sun from the asteroid is shown as $\vec{r}_{S,I}$.

The two frames are defined as follows:

1. AIF (Asteroid-Centric Inertial Frame) - This is a non-rotating frame fixed inertially in space with its origin at the centre of mass of the asteroid . Figure 4.3 shows the orientation of the frame (in *x*-*y* plane) such that the *x-axis* is pointing to the Sun when the Longitude of the Sun (or effectively the True Anomaly of the apparent circular motion of the Sun around the asteroid) ϑ is zero. The *y-axis*, thus, points to the sun when $\vartheta = 90^o$ and finally the *z-axis* is obtained by following the right-hand rule, coming out of the sheet in 3D.

2. ARF (Asteroid-Centric Rotating Frame) - This frame is fixed to the rotating asteroid with its origin at the centre of mass of the asteroid and axes aligned with the principle axes of the asteroid. Figure 4.2 shows the orientation of this frame, assuming a triaxial ellipsoid model for our asteroid (for details see Section 4.3). The *x-axis* is pointing along the longest axis of the triaxial ellipsoid, and the *z-axis* is pointing along the shortest axis of the ellipsoid. It is also aligned with the z_I axis of AIF as shown in Figure 4.1. The *y-axis* points in the direction of the remaining third axis, satisfying the right-hand rule. The asteroid (and effectively the ARF) is rotating in a counter-clockwise sense, with respect to the AIF, with constant angular velocity ω about the z_B axis as depicted in Figure 4.1.

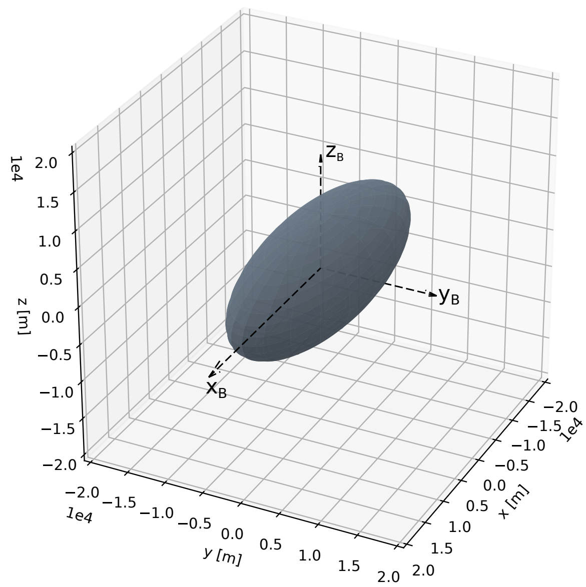

Figure 4.2: Representation of the body-fixed rotating frame for a triaxial ellipsoid model of an asteroid. $\boldsymbol{x_B}$ is aligned with the longest axis, $\boldsymbol{z_B}$ is aligned with the shortest axis and $\boldsymbol{y_B}$ is aligned with the remaining last axis of the ellipsoid, satisfying the right-hand rule.

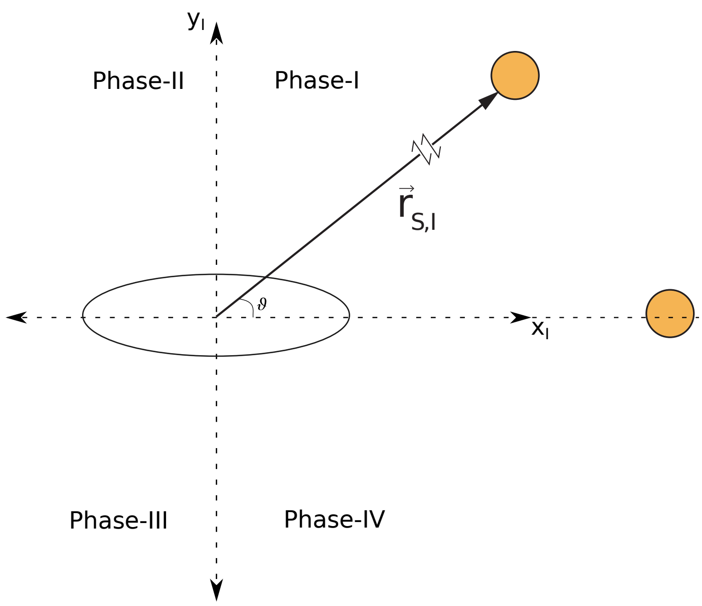

Figure 4.3: Asteroid-centric inertial frame x-y plane. The position vector to the Sun is shown as $\vec{\boldsymbol{r}}_{S,I}$. The apparent motion of the Sun around the asteroid, assumed a circular orbit, is also depicted with ϑ as the Longitude of Sun (or effectively the True Anomaly). The four phases are for a broader identification of the Sun's location with respect to the asteroid.

We have two different frames of reference because it is important to visualize the same orbital motion with respect to both an inertial frame and a non-inertial frame to get a better understanding of the underlying dynamics. In this regard, it is thus important to be able to transfer a state vector between the two frames. The transfer matrix to transform a state vector from ARF to AIF is given as follows (Schaub et al. 2003):

$$\begin{aligned} \phi_B^I &= \begin{bmatrix} \cos\theta & -\sin\theta & 0 \\ \sin\theta & \cos\theta & 0 \\ 0 & 0 & 1 \end{bmatrix} \\ \theta &= \omega t \end{aligned} \tag{4.1}$$

In Equation (4.1), θ is the angle of rotation between the ARF and the AIF at any given time t; and ω is the constant angular velocity of the rotating asteroid about z_I/z_B axis as shown in Figure 4.1. The position vector is then transformed, from ARF to AIF, as follows (Schaub et al. 2003):

$$\begin{bmatrix} x_I \\ y_I \\ z_I \end{bmatrix} = \begin{bmatrix} \cos\theta & -\sin\theta & 0 \\ \sin\theta & \cos\theta & 0 \\ 0 & 0 & 1 \end{bmatrix} \begin{bmatrix} x_B \\ y_B \\ z_B \end{bmatrix} \tag{4.2}$$

In Equation (4.2), x_I and x_B are the x-components of the position vector in AIF and ARF respectively; other components follow similar definitions. The velocity transformation takes place by first using the *transport theorem* and then multiplying the resultant with the transformation matrix ϕ_B^I (Schaub et al. 2003). The transformation is shown as follows:

$$\vec{\boldsymbol{v}}_I^B = \vec{\boldsymbol{v}}_B + \vec{\boldsymbol{\omega}} \times \vec{\boldsymbol{r}}_B \tag{4.3}$$

$$\vec{\boldsymbol{v}}_I = \phi_B^I \vec{\boldsymbol{v}}_I^B \tag{4.4}$$

Equation (4.3) is the application of the transport theorem to get the AIF velocity in ARF components ($\vec{\boldsymbol{v}}_I^B$). In that, $\vec{\boldsymbol{v}}_B$ is the velocity vector in the ARF, $\vec{\boldsymbol{\omega}}$ is the angular velocity vector for the asteroid's rotation (note that we have only uniform rotation about the z_B axis), and $\vec{\boldsymbol{r}}_B$ is the position vector defined in the ARF. In Equation (4.4), $\vec{\boldsymbol{v}}_I$ is the velocity vector in the AIF.

The transfer matrix to transform a state vector from AIF to ARF is just the transpose of ϕ_B^I as it is orthogonal (Schaub et al. 2003). It is given as follows:

$$\phi_I^B = \begin{bmatrix} \cos\theta & \sin\theta & 0 \\ -\sin\theta & \cos\theta & 0 \\ 0 & 0 & 1 \end{bmatrix} \tag{4.5}$$

Then the state vector transformation from AIF to ARF takes place as follows:

$$\vec{\boldsymbol{r}}_B = \phi_I^B \vec{\boldsymbol{r}}_I \tag{4.6}$$

$$\vec{\boldsymbol{v}}_B^I = \vec{\boldsymbol{v}}_I - \vec{\boldsymbol{\omega}} \times \vec{\boldsymbol{r}}_I \tag{4.7}$$

$$\vec{\boldsymbol{v}}_B = \phi_I^B \vec{\boldsymbol{v}}_B^I \tag{4.8}$$

where $\vec{\boldsymbol{v}}_B^I$ is the ARF velocity in AIF components, and $\vec{\boldsymbol{r}}_I$ is the position vector in the AIF.

4.3 GRAVITATIONAL POTENTIAL

The key feature that differentiates small bodies, or asteroids for our particular case, from planets is their highly irregular shapes and thus non-spherical mass distributions (Scheeres 2016). This is why the dynamics close to an asteroid are deemed as interesting and hence it is very important that the gravitational potential is modeled properly.

4.3.1 SPHERICAL AND ELLIPSOIDAL HARMONICS

One of the most common methods for modeling gravity potential of any celestial body is the *spherical harmonics* model. In that, a sphere whose radius is equal to the maximum dimension of the irregular body, circumscribes it and this sphere is called the *Brillouin sphere* (see Figure 4.4). The spherical harmonics model then induces deformities on the Brillouin sphere, thereby producing a non-spherical gravity field. The spherical harmonics gravity potential is stated as follows (Scheeres 2016):

$$U(r,\delta,\lambda) = \frac{\mu}{r}\sum_{l=0}^{\infty}\sum_{m=0}^{l}\left(\frac{r_0}{r}\right)^l P_{lm}(\sin\delta)[C_{lm}\cos m\lambda + S_{lm}\sin m\lambda] \tag{4.9}$$

where U is the gravitational potential calculated at a distance r from the centre of the Brillouin sphere at latitude δ and longitude λ, μ is the gravitational parameter of the irregular body or asteroid, r_0 is the radius of the Brillouin sphere, P_{lm} are the associated Legendre functions, C_{lm} and S_{lm} are the spherical harmonic coefficients which account for shape and density variations (Romain et al. 2001), and l and m are the degree and order, respectively, of the spherical harmonic expansion. The definitions and calculations for the associated Legendre functions and the harmonics coefficients has been explained in detail by Scheeres 2016 and is not repeated here for brevity. The majority of gravity field perturbations can be accounted for by just considering the second degree and order in the spherical harmonics expansion. The potential is then expressed as follows (Scheeres 2016):

$$U = \frac{\mu}{r}\left[1 + \left(\frac{r_0}{r}\right)^2\left\{C_{20}\left(1 - \frac{3}{2}\cos^2\delta\right) + 3C_{22}\cos^2\delta\cos(2\lambda)\right\}\right] \tag{4.10}$$

where the spherical harmonic coefficients can be obtained from the principle moments of inertia as defined in Scheeres 2016.

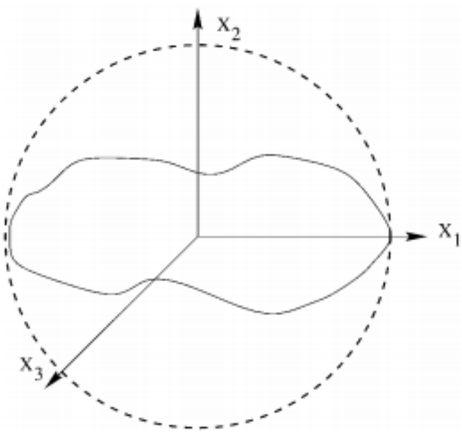

Figure 4.4: Brillouin sphere or the circumscribing sphere around an irregular body (Romain et al. 2001).

Now consider a general statement for the gravity field of any arbitrary mass distribution $\mathcal{B}$ (Scheeres 2016):

$$U = \frac{\mu}{V}\int_{\mathcal{B}}\frac{dV}{|\vec{\boldsymbol{r}} - \vec{\boldsymbol{\rho}}|} \tag{4.11}$$

where V is the volume, $\vec{\boldsymbol{r}}$ is the position vector to the point where the potential is being calculated, $\vec{\boldsymbol{\rho}}$ is the position vector to the discrete mass distribution within $\mathcal{B}$. If the potential is being calculated for a point that lies outside the maximum radius of the mass distribution being considered, then the integrand in Equation (4.11) can be expanded into the following Laplace series form (Scheeres 2016):

$$\frac{1}{|\vec{\boldsymbol{r}} - \vec{\boldsymbol{\rho}}|} = \frac{1}{r} \sum_{i=0}^{\infty} \left(\frac{\rho}{r}\right)^i P_{i0}\left(\frac{\vec{\boldsymbol{r}} \cdot \vec{\boldsymbol{\rho}}}{r\rho}\right) \tag{4.12}$$

where P_{i0} are the Legendre polynomials. Thus using Equation (4.12), the integral in Equation (4.11) can be restated as follows (Scheeres 2016):

$$\frac{1}{V} \int_{\mathcal{B}} \left(\frac{\rho}{r}\right)^i P_{i0}\left(\frac{\vec{\boldsymbol{r}} \cdot \vec{\boldsymbol{\rho}}}{r\rho}\right) dV \tag{4.13}$$

There is a one-to-one correspondence between the integral in Equation (4.13) and the ith degree and order spherical harmonics gravity field. Thus by looking at the Laplace series in Equation (4.12) and the integral in Equation (4.13), we can infer on the convergence or divergence of the spherical harmonics gravity field. Since the maximum radius of the mass distribution in case of the spherical harmonics model would be that of the circumscribing or Brillouin sphere, then for a point on this sphere, i.e. $r = |\vec{\boldsymbol{\rho}}|$, the Laplace series is not defined and for a point inside the sphere, i.e. $r < |\vec{\boldsymbol{\rho}}|$, the Laplace series diverges. This is the limitation for using the spherical harmonics model for an irregular body when one wants to compute orbital motion in close-proximity to the body. If the computation points are within the Brillouin sphere then the spherical harmonics series might diverge to a value that does not represent the true gravitational potential value and hence lead to errors in orbit computations. We can see from Figure 4.4 that the volume of divergence for irregularly shaped asteroids can be quite significant. Thus, this model is definitely not suitable for our research since we are dealing with close-proximity orbits and above all, particle re-impact scenarios.

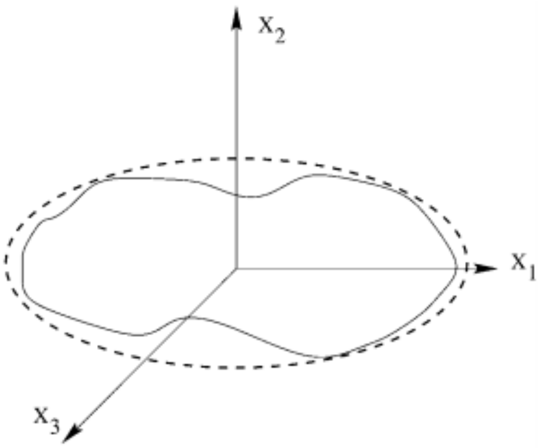

Figure 4.5: Brillouin ellipsoid or the circumscribing ellipsoid around an irregular body (Romain et al. 2001).

The above problem can be mitigated, to a certain extent, by using the *ellipsoidal harmonics* expansion for representing the gravity potential of an irregular body. An extremely detail account on this model is given by Dechambre et al. 2002. In the ellipsoidal harmonics model, instead of a sphere, a triaxial ellipsoid is used to circumscribe the irregular body and proves to be a better fit as shown in Figure 4.5. The ellipsoidal harmonics potential is then given as follows (Dechambre et al.

2002):

$$U(\lambda_1,\lambda_2,\lambda_3) = \mu \sum_{n=0}^{\infty} \sum_{p=1}^{2n+1} \alpha_{np} \frac{E_n^p(\lambda_1)}{E_n^p(\lambda_1^{ref})} \times E_n^p(\lambda_2)E_n^p(\lambda_3);\ \lambda_1 \leq \lambda_1^{ref} \tag{4.14}$$

$$U(\lambda_1,\lambda_2,\lambda_3) = \mu \sum_{n=0}^{\infty} \sum_{p=1}^{2n+1} \alpha_{np} \frac{F_n^p(\lambda_1)}{F_n^p(\lambda_1^{ref})} \times E_n^p(\lambda_2)E_n^p(\lambda_3);\ \lambda_1 \geq \lambda_1^{ref} \tag{4.15}$$

where $(\lambda_1, \lambda_2, \lambda_3)$ are the ellipsoidal coordinates, which are basically three real roots (solutions) in terms of s for the following conic equation (Garmier et al. 2002):

$$\frac{x^2}{s^2+a^2} + \frac{y^2}{s^2+b^2} + \frac{z^2}{s^2+c^2} = 1 \tag{4.16}$$

where (x, y, z) are the Cartesian coordinates and (a, b, c) are the semi-major axes of the reference ellipsoid circumscribing the irregular body (note that $a = \lambda_1^{ref}$). In Equations (4.14) and (4.15), $(\lambda_1, \lambda_2, \lambda_3)$ are analogous to the radius r, latitude δ and longitude λ, respectively, of Equation (4.9); α_{np} is the ellipsoidal harmonics expansion coefficient similar to the spherical harmonics coefficient C_{lm} and S_{lm}; $F_n^p()$ are the Lamé function of second kind of degree n and order p and is analogous to the attenuation term $(r_0/r)^l$ of the spherical harmonics expansion in Equation (4.9); $E_n^p()$ is the Lamé function of the first kind of degree n and order p; and finally, the product term $E_n^p(\lambda_2)E_n^p(\lambda_3)$ is analogous to the product term $P_{lm}(\sin\delta)[C_{lm}\cos m\lambda + S_{lm}\sin m\lambda]$ which in both cases models the surface harmonic (Garmier et al. 2002). A detailed description on definition and calculation of the ellipsoidal harmonic coefficients and the Lamé functions of the first and the second kind can be found in Dechambre et al. 2002 and is not repeated here for brevity.

Even in the case of ellipsoidal harmonics expansion model, the gravity potential calculated for a point inside the circumscribing ellipsoid can diverge from the true potential. But the advantage of this model over the spherical harmonics expansion is that the circumscribing reference ellipsoid reduces the volume of divergence around the irregular body, relative to a sphere, making close-proximity evaluations possible. However, relative to spherical harmonics expansion, the computation of the basis functions for ellipsoidal harmonics, i.e. the Lamé functions of the first and the second kind, is extremely complex. On top of that, with increasing degree of the harmonics model, the order of magnitude of the Lamé functions increases, which then runs the risk of arithmetic overflow, thereby impeding accurate calculations of the harmonic expansion for degrees above 10 to 15 (Reimond et al. 2016). However, in their research, Reimond et al. 2016 have devised a new method to calculate the basis functions using logarithmic expressions which allows accurate harmonic expansions for degrees of upto 500 but the computational complexity also increases tremendously as stated by them. Ultimately, since we wish to express the motion of particles close to the surface of the asteroid, which also involves surface interactions, the approach of ellipsoidal harmonics expansion also fails.

4.3.2 CONSTANT DENSITY POLYHEDRON

The gravity potential modeling methods discussed so far involved the use of surface harmonics on the circumscribing object (sphere or ellipsoid) to simulate a non-homogeneous gravity field for an irregular body. The major drawback with the harmonics approach was its divergence from the true potential value within the circumscribing volume. This problem can be mitigated all together by assuming a specific shape and density distribution for the irregular body in question. In this realm, there are the CDE and constant density polyhedron gravity potential models. Unlike the harmonics expansion approach, these potential models are valid upto and on the surface of the shape that has been assumed for the irregular body in question (Scheeres 2016). Hence, these models are perfect to study close-proximity motion of particles or spacecraft around an asteroid.

The irregular shape of an asteroid can be best represented by a polyhedron shape model (henceforth polyhedron) as shown in Figure 4.6. Surface irregularities in the form of craters, large boulders, mountains etc. can be easily modeled with this method. A polyhedron is basically a 3D body that consists of several *vertices* which form triangular faces or *facets* that are connected to each other through the *edges* of each face. A triangular facet thus comprises of three vertices, three edges and a surface normal as shown in Figure 4.7 (Scheeres 2016). A detailed derivation for the polyhedron gravitational potential model is given in Werner et al. 1996 and concisely presented in Scheeres 2016 as well. Hence, we will only present a summary of this method in this section.

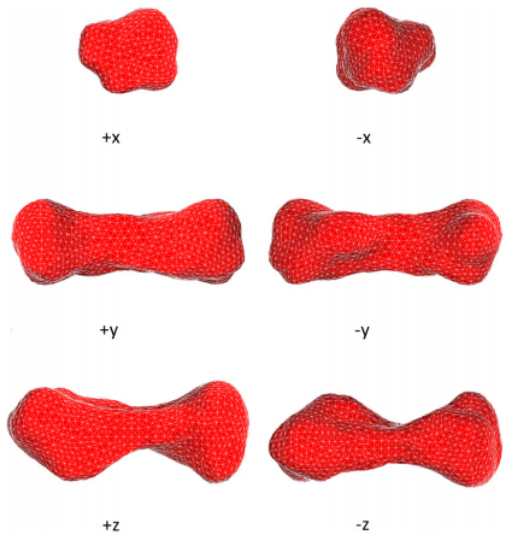

Figure 4.6: Polyhedron shape model estimated for asteroid *Kleopatra* and shown in $\pm x, \pm y, \pm z$ axis directions. Constant density has been assumed in this modeling process. Surface deformities are easily modeled by this method (Yu et al. 2012).

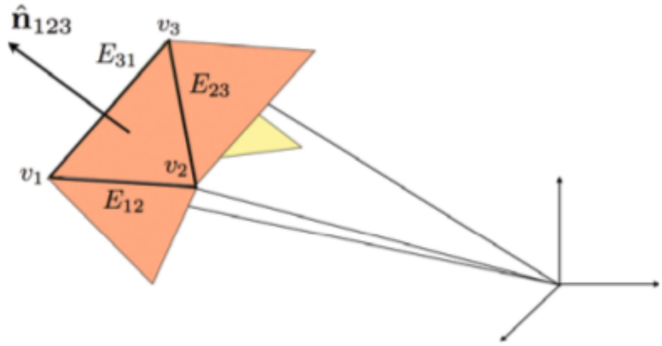

Figure 4.7: Single facet of a polyhedron model depicting three vertices, three edges and a surface normal, associated with each facet in general (Scheeres 2016).

Each face or facet *'f'* of the polyhedron is associated with three vertex vectors given as $\vec{\boldsymbol{r}}_i^f$, where $i = 1,2,3$, and a unit normal vector $\hat{\boldsymbol{n}}_f$. The vector $\vec{\boldsymbol{r}}_i^f$ goes from each vertex of a facet to the field point **P** where the potential has to be calculated. Each edge *'e'* is associated to two vertex vectors $\vec{\boldsymbol{r}}_i^e$, for $i = 1,2$, and this edge connects two adjacent faces f and f'. Again, the vector $\vec{\boldsymbol{r}}_i^e$ goes from the edge vertices to the field point **P**. The edge normal, corresponding to facet *f*, is denoted as $\hat{\boldsymbol{n}}_e^f$ such that it is perpendicular to the edge and the facet normal $\hat{\boldsymbol{n}}_f$ and is pointing away from the centre of the facet. For the same edge shared by facet f', the edge normal $\hat{\boldsymbol{n}}_e^{f'}$ points in a different direction than $\hat{\boldsymbol{n}}_e^{f}$ and may not be parallel to it. With these definitions, the general formula for the polyhedron gravitational potential is given as follows (Scheeres 2016):

$$U(\vec{\boldsymbol{r}}) = \frac{\mathcal{G}\sigma}{2}\left[\sum_{e\in edges} \vec{\boldsymbol{r}}_e\cdot \boldsymbol{E}_e\cdot \vec{\boldsymbol{r}}_e L_e - \sum_{f\in faces} \vec{\boldsymbol{r}}_f\cdot \boldsymbol{F}_f\cdot \vec{\boldsymbol{r}}_f \omega_f\right] \tag{4.17}$$

$$\boldsymbol{E}_e = \hat{\boldsymbol{n}}_f \hat{\boldsymbol{n}}_e^{f} + \hat{\boldsymbol{n}}_{f'} \hat{\boldsymbol{n}}_e^{f'} \tag{4.18}$$

$$\boldsymbol{F}_f = \hat{\boldsymbol{n}}_f \hat{\boldsymbol{n}}_f \tag{4.19}$$

$$L_e = ln\left(\frac{r_1^e + r_2^e + e_e}{r_1^e + r_2^e - e_e}\right) \tag{4.20}$$

$$e_e = |\vec{\boldsymbol{r}}_1^e - \vec{\boldsymbol{r}}_2^e| \tag{4.21}$$

$$\omega_f = 2\tan^{-1}\left(\frac{\vec{\boldsymbol{r}}_1^f\cdot(\vec{\boldsymbol{r}}_2^f \times \vec{\boldsymbol{r}}_3^f)}{r_1^f r_2^f r_3^f + r_1^f(\vec{\boldsymbol{r}}_2^f\cdot\vec{\boldsymbol{r}}_3^f) + r_2^f(\vec{\boldsymbol{r}}_3^f\cdot\vec{\boldsymbol{r}}_1^f) + r_3^f(\vec{\boldsymbol{r}}_1^f\cdot\vec{\boldsymbol{r}}_2^f)}\right) \tag{4.22}$$

where $\vec{\boldsymbol{r}}$ is the position vector to the field point **P** from the origin of an asteroid-fixed reference frame; $\mathcal{G}$ is the universal gravitational constant and σ is the density of the body being modeled; $\vec{\boldsymbol{r}}_e$ is the vector from any point along the edge *'e'* to $\vec{\boldsymbol{r}}$ or the field point **P** and in the same way $\vec{\boldsymbol{r}}_f$ denotes a vector from any point on the facet f to $\vec{\boldsymbol{r}}$ (Scheeres 2016); the term ω_f represents the solid angle subtended by a facet when viewed from the field point **P**, or alternately, it is the angle subtended by the facet of the polyhedron on to a unit sphere centered at the field point **P**; L_e is analogous to the potential of a 1D straight *'wire'* and is computed for all facet edges in a polyhedron (Werner et al. 1996); $\boldsymbol{E}_e$ is the edge dyad and is expressed as the sum of two outer-products, forming a 3x3 matrix; and finally $\boldsymbol{F}_f$ is the facet dyad which is simply the outer-product of the facet normal vector with itself (Werner et al. 1996).

The constant density polyhedron gravitational potential model provides a realistic shape for an irregular body by accounting for topographical irregularities, however, the polyhedron model is computationally expensive (Scheeres 2016). This thesis work does not make use of this model, but instead, employs a triaxial ellipsoid to model the gravitational potential (explained in the following section). This is because we wanted to understand the fundamental phenomenon associated with the motion and final fate of regolith in presence of gravity and Solar perturbations. This fundamental phenomenon would be difficult to decouple from other effects of a true irregular body, such as in the case of a polyhedron model and hence it was not used in this thesis. A triaxial ellipsoid itself is a very good approximation of real small body shapes (Broschart et al. 2005) and hence we don't loose out on the validity of explanations for the fundamental features of regolith motion by excluding the polyhedron model.

4.3.3 CONSTANT DENSITY ELLIPSOID

Consider a CDE with semi-major axes (α, β, γ) such that $\gamma \leq \beta \leq \alpha$. The shape of the triaxial ellipsoid is completely defined by the equation $(x/\alpha)^2 + (y/\beta)^2 + (z/\gamma)^2 \leq 1$. The density of the ellipsoid is assumed to be constant. An example for a CDE model is shown in Figure 4.8. Then the gravitational potential for a point external to such a body, i.e. CDE, is defined by the following equation (Scheeres

2016):

$$U(\vec{r}) = -\frac{3\mu}{4}\int_{\lambda(\vec{r})}^{\infty} \phi(\vec{r},u)\frac{du}{\Delta(u)} \tag{4.23}$$

$$\phi(\vec{r},u) = \frac{x^2}{\alpha^2+u} + \frac{y^2}{\beta^2+u} + \frac{z^2}{\gamma^2+u} - 1 \tag{4.24}$$

$$\Delta(u) = \sqrt{(\alpha^2+u)(\beta^2+u)(\gamma^2+u)} \tag{4.25}$$

where $\vec{r}$ is the position vector to the point, external to the CDE, and is defined in the ARF; $\lambda(\vec{r})$ is a parameter defined by the equation $\phi(\vec{r},\lambda) = 0$, which is a cubic polynomial as shown in Equation (4.26), and the value λ is the maximum real root of this polynomial (Scheeres 2016).

$$\begin{aligned} \lambda^3 + \\ \lambda^2(\alpha^2+\beta^2+\gamma^2-(x^2+y^2+z^2)) + \\ \lambda(\alpha^2\beta^2+\alpha^2\gamma^2+\beta^2\gamma^2-x^2(\beta^2+\gamma^2)-y^2(\alpha^2+\gamma^2)-z^2(\alpha^2+\beta^2)) + \\ (\alpha^2\beta^2\gamma^2-x^2\gamma^2\beta^2-y^2\alpha^2\gamma^2-z^2\alpha^2\beta^2) = 0 \end{aligned} \tag{4.26}$$

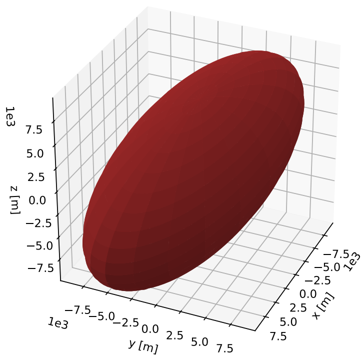

Figure 4.8: Triaxial ellipsoid model with semi-major axes $\alpha = 20$ km, $\beta = 7$ km, $\gamma = 7$ km.

For a given point (x, y, z) in space around the CDE, the only unknown in Equation (4.26) is λ which is solved for using the standard Cardano's formula (see Weisstein, "Cubic"). Now for the given ellipsoid, the equation for the family of confocal quadratic surfaces is given as follows (Panou 2014):

$$\frac{x^2}{\alpha^2+u} + \frac{y^2}{\beta^2+u} + \frac{z^2}{\gamma^2+u} = 1 \tag{4.27}$$

where u is a real-valued parameter whose value defines the type of the confocal quadratic surface. Equation (4.27) is a cubic polynomial in u and can be solved to obtain three unequal real roots - u_1, u_2, u_3, such that the following relation holds true (Panou 2014):

$$-\alpha^2 < u_3 < -\beta^2 < u_2 < -\gamma^2 < u_1 < +\infty \tag{4.28}$$

where u_1 is the maximum real root possible and at that value, Equation (4.27) defines another ellipsoid which is confocal to the original one defined by the semi-major axes $\rightarrow \alpha, \beta, \gamma$ (Panou 2014). Thus, the value of λ in Equation (4.23) conforms to a confocal ellipsoid for a given point external to the original ellipsoid (which in turn is modeling the asteroid).

The potential defined by Equation (4.23) appears to have a complicated computational process due to its integral form. However, the integral can be split into multiple parts such that each can be solved with the help of standard functions called *Carlson's Elliptic Integrals* (Carlson 1987). Software routines for these integrals exist in several computing languages which, for our case, helps in computing the CDE gravitational potential. The integral defined in Equations (4.23) to (4.25) is restated in its complete form as follows:

$$U(\vec{r}) = -\frac{3\mu}{4}\int_{\lambda(\vec{r})}^{\infty}\left(\frac{x^2}{\alpha^2+u}+\frac{y^2}{\beta^2+u}+\frac{z^2}{\gamma^2+u}-1\right)\frac{du}{\sqrt{(\alpha^2+u)(\beta^2+u)(\gamma^2+u)}} \tag{4.29}$$

Equation (4.29) can be split into 4 parts which are stated as follows:

$$U_1 = -\frac{\mu}{2}\cdot\frac{3}{2}\int_{\lambda}^{\infty}\frac{x^2}{(\alpha^2+u)^{3/2}(\beta^2+u)^{1/2}(\gamma^2+u)^{1/2}}du \tag{4.30}$$

$$U_2 = -\frac{\mu}{2}\cdot\frac{3}{2}\int_{\lambda}^{\infty}\frac{y^2}{(\alpha^2+u)^{1/2}(\beta^2+u)^{3/2}(\gamma^2+u)^{1/2}}du \tag{4.31}$$

$$U_3 = -\frac{\mu}{2}\cdot\frac{3}{2}\int_{\lambda}^{\infty}\frac{z^2}{(\alpha^2+u)^{1/2}(\beta^2+u)^{1/2}(\gamma^2+u)^{3/2}}du \tag{4.32}$$

$$U_4 = +\frac{\mu}{2}\cdot\frac{3}{2}\int_{\lambda}^{\infty}\frac{du}{(\alpha^2+u)^{1/2}(\beta^2+u)^{1/2}(\gamma^2+u)^{1/2}} \tag{4.33}$$

where $\lambda(\vec{r})$ is simply written as λ for brevity. Thus, the CDE potential is given as $U = U_1+U_2+U_3+U_4$. We make the following substitution for Equations (4.30) to (4.33):

$$u = v+\lambda \tag{4.34}$$

$$du = dv \tag{4.35}$$

$$u = \lambda;\ v = 0 \tag{4.36}$$

$$u = \infty;\ v = \infty \tag{4.37}$$

With these substitutions, Equation (4.30), for example, can now be re-written as follows:

$$U_1 = -\frac{\mu x^2}{2}\left[\frac{3}{2}\int_0^{\infty}\frac{dv}{((\alpha^2+\lambda)+v)^{3/2}((\beta^2+\lambda)+v)^{1/2}((\gamma^2+\lambda)+v)^{1/2}}\right] \tag{4.38}$$

$$= -\frac{\mu x^2}{2}R_D(\beta^2+\lambda,\gamma^2+\lambda,\alpha^2+\lambda) \tag{4.39}$$

In Equation (4.38), the expression within the square braces conforms to the standard elliptic integral function R_D as defined by Carlson 1987 and is given as follows:

$$R_D(x,y,z) = \frac{3}{2}\int_0^{\infty}\frac{dt}{(t+x)^{1/2}(t+y)^{1/2}(t+z)^{3/2}} \tag{4.40}$$

Similarly, Equations (4.31) and (4.32) can be re-written using the standard elliptic integral function R_D as follows:

$$U_2 = -\frac{\mu y^2}{2}R_D(\alpha^2+\lambda,\gamma^2+\lambda,\beta^2+\lambda) \tag{4.41}$$

$$U_3 = -\frac{\mu z^2}{2}R_D(\alpha^2+\lambda,\beta^2+\lambda,\gamma^2+\lambda) \tag{4.42}$$

For Equation (4.33), we use another standard elliptic integral function as defined by Carlson 1987:

$$R_F(x,y,z) = \frac{1}{2}\int_0^\infty \frac{dt}{(t+x)^{1/2}(t+y)^{1/2}(t+z)^{1/2}} \tag{4.43}$$

using which, Equation (4.33) is re-written as follows:

$$U_4 = \frac{3\mu}{2} R_F(\alpha^2+\lambda, \beta^2+\lambda, \gamma^2+\lambda) \tag{4.44}$$

Thus, to calculate the CDE gravitational potential U at any given point (x, y, z) external to the ellipsoid, we first calculate the corresponding value of λ from Equation (4.26) and then substitute this value into Equations (4.39), (4.41), (4.42) and (4.44), the sum of which is the final potential value.

The gravitational acceleration components are obtained by taking a partial derivatives of the potential equation given in Equation (4.29) (Scheeres 2016):

$$U_x = -\frac{3\mu x}{2}\int_{\lambda(\vec{r})}^\infty \frac{du}{(\alpha^2+u)\Delta u} \tag{4.45}$$

$$U_y = -\frac{3\mu y}{2}\int_{\lambda(\vec{r})}^\infty \frac{du}{(\beta^2+u)\Delta u} \tag{4.46}$$

$$U_z = -\frac{3\mu z}{2}\int_{\lambda(\vec{r})}^\infty \frac{du}{(\gamma^2+u)\Delta u} \tag{4.47}$$

where (U_x, U_y, U_z) are the gravitational acceleration terms and all other terms have the same definition as explained before for the CDE potential term. Just like with the gravitational potential, the acceleration terms can be reduced to standard Carlson's elliptic integrals by using the same substitution parameters as defined in Equations (4.34) to (4.37). After substitution, for example, the x-component of the acceleration term is written as follows:

$$U_x = -\frac{-3\mu x}{2}\int_0^\infty \frac{dv}{(\alpha^2+v+\lambda)\sqrt{(\alpha^2+v+\lambda)(\beta^2+v+\lambda)(\gamma^2+v+\lambda)}} \tag{4.48}$$

$$= -\mu x\left[\frac{3}{2}\int_0^\infty \frac{dv}{((\alpha^2+\lambda)+v)^{3/2}((\beta^2+\lambda)+v)^{1/2}((\gamma^2+\lambda)+v)^{1/2}}\right] \tag{4.49}$$

$$= -\mu x \cdot R_D((\beta^2+\lambda), (\gamma^2+\lambda), (\alpha^2+\lambda)) \tag{4.50}$$

Similarly, the other components of the gravitational acceleration (defined in the ARF) can be written as follows:

$$U_y = -\mu y \cdot R_D((\alpha^2+\lambda), (\gamma^2+\lambda), (\beta^2+\lambda)) \tag{4.51}$$

$$U_z = -\mu z \cdot R_D((\alpha^2+\lambda), (\beta^2+\lambda), (\gamma^2+\lambda)) \tag{4.52}$$

For any point (x, y, z) outside of the CDE, we calculate the value for λ first by solving Equation (4.26) and then substitute it into Equations (4.50) to (4.52) to get the acceleration components in the ARF.

4.4 SOLAR PERTURBATIONS

The dominant force acting on an orbiting particle in the vicinity of an asteroid is from its gravity field. However, perturbations, both gravitational and non-gravitational, can be significant especially when the particle is further away from the asteroid (Scheeres 2016). The two most significant sources of perturbations are from the Sun and we will be discussing them briefly in this section.

4.4.1 SOLAR THIRD-BODY EFFECT (STBE)

We consider a simple two-body problem, wherein the asteroid has a circular, Heliocentric orbit in the Ecliptic plane. This is a reasonable approximation, as mentioned earlier in Section 4.1, since several asteroids have been observed to have circular orbits around the Sun with near-zero inclinations. The gravitational effect of the Sun on the motion of regolith (henceforth STBE) around the asteroid is not modeled through a three-body problem because the order of magnitude of the perturbing acceleration is extremely small relative to the gravitational acceleration of the asteroid (atleast 5 orders of magnitude smaller in the vicinity of a sample asteroid at 1 AU from the Sun) and hence it is sufficient to model it as an external perturbing acceleration.

The absolute gravitational acceleration, due to the Sun, experienced by a particle (of mass negligible compared to that of the Sun) in orbital motion around the asteroid is given as (Scheeres 2016):

$$\vec{\boldsymbol{a}}_{abs,p} = -\frac{\mu_S}{|\vec{\boldsymbol{r}} - \vec{\boldsymbol{d}}|^3}(\vec{\boldsymbol{r}} - \vec{\boldsymbol{d}}) \tag{4.53}$$

where μ_S is the gravitational parameter of the Sun; $\vec{\boldsymbol{r}}$ and $\vec{\boldsymbol{d}}$ are the position vectors of the orbiting particle and the Sun, respectively, from the asteroid's centre of mass, defined in the AIF. In Equation (4.53), the Sun is viewed to be orbiting the asteroid, instead of the other way around. This is just a change in perspective and is done to keep all distance vector definitions originating from the centre of mass of the asteroid (Scheeres 2016). The orientation of the position vectors is shown in Figure 4.9.

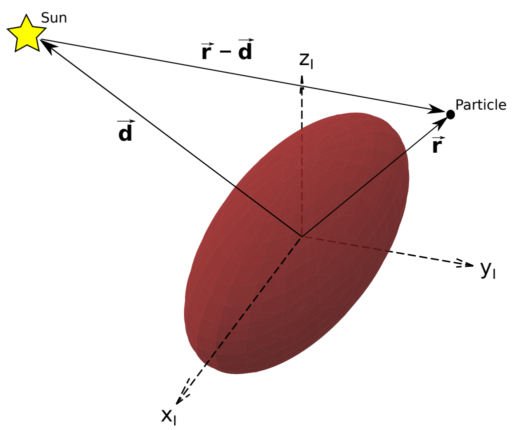

Figure 4.9: A schematic representing the orientation of position vectors of the Sun and the orbiting particle/regolith around the asteroid, in the AIF. Diagram is not to scale and the rotation state of asteroid is such that the ARF and AIF are coinciding.

Now the absolute gravitational acceleration, due to the Sun, experienced by the asteroid is given as follows (Scheeres 2016):

$$\vec{\boldsymbol{a}}_{abs,a} = +\frac{\mu_S}{|\vec{\boldsymbol{d}}|^3}(\vec{\boldsymbol{d}}) \tag{4.54}$$

where the definition of all variables is the same as that for Equation (4.53). Thus, the perturbing acceleration acting on the particle due to the STBE is the difference between the absolute accelerations experienced by the particle (Equation (4.53)) and the asteroid (Equation (4.54)) (Scheeres 2016):

$$\vec{a}_{STBE} = -\mu_S \left[\frac{(\vec{r} - \vec{d})}{|\vec{r} - \vec{d}|^3} + \frac{\vec{d}}{|\vec{d}|^3} \right] \tag{4.55}$$

The perturbing acceleration in Equation (4.55) can be re-written in the form of a potential as follows (Scheeres 2016):

$$\mathcal{R}_{STBE} = \mu_S \left[\frac{1}{|\vec{r} - \vec{d}|} - \frac{\vec{d} \cdot \vec{r}}{|\vec{d}|^3} \right] \tag{4.56}$$

$$\vec{a}_{STBE} = \frac{\delta \mathcal{R}_{STBE}}{\delta \vec{r}} \tag{4.57}$$

In Equation (4.55), we can directly substitute the position vectors as defined in ARF such that the acceleration term obtained is also in the ARF. This is possible because the position magnitude terms would remain the same in either of the reference frames. Also, the rotation matrix ϕ_I^B multiplied either outside the square bracket or inside, in Equation (4.55), with the two numerator terms would ultimately give the same result.

$$\ddot{\vec{d}} = -\frac{\mu_S}{|\vec{d}|^3}(\vec{d}) \tag{4.58}$$

The apparent position of the Sun, relative to the asteroid, can be obtained in two ways. We could either numerically integrate the second order differential equation for the standard two-body problem as stated in Equation (4.58) or solve, what is historically known as, the *Kepler's problem*. We use the latter since the apparent position of the Sun can be obtained for any time value directly by using the Kepler's problem algorithm as stated by Chobotov 2002. Although the Kepler's problem algorithm is not completely analytical and uses a numerical iteration method to solve for the true anomaly, it is relatively easier to use within the simulator than employing a numerical integrator to propagate the position from an initial condition for every time value. The algorithm for solving the Kepler's problem is not stated here for brevity; A detailed explanation for it is given by Chobotov 2002.

4.4.2 SOLAR RADIATION PRESSURE (SRP)

With the heliocentric orbit of the asteroid, in addition to the STBE, is a non-gravitational source of perturbation acting on an asteroid-orbiting particle, called SRP. Momentum transfer takes place from the Solar photons that strike and recoil from the surface of the particle, which thus perturbs the orbital motion (Scheeres 2016).

We use a model for SRP that assumes that the particle always presents a constant area to the impinging Solar photons and the area is perpendicular to the Sun-line. The total momentum transfer is modeled as Solar irradiance and reflection and the acceleration due to SRP thus acts in a direction away from and along the Sun-line (Scheeres 2016). This acceleration is given as follows:

$$\vec{a}_{SRP} = -(1+\rho)P_0 \cdot \frac{A}{M} \cdot \frac{(\vec{d} - \vec{r})}{|\vec{d} - \vec{r}|^3} \tag{4.59}$$

where ρ is the albedo of the particle; P_0 is a Solar constant whose value is 1.0×10^{17} kg m/s^2; A/M is the area-to-mass ratio of the particle and area refers to the cross-sectional area of the particle on which the Solar photons are striking; $\vec{d}$ is the distance vector from the asteroid to the Sun and $\vec{r}$ is the distance vector from the asteroid to the orbiting particle (Scheeres 2016). The SRP perturbing acceleration can be re-stated in terms of a perturbing potential as follows:

$$\mathcal{R}_{SRP} = -(1+\rho)P_0 \cdot \frac{A}{M}\left[\frac{1}{|\vec{\boldsymbol{d}} - \vec{\boldsymbol{r}}|}\right] \tag{4.60}$$

$$\vec{\boldsymbol{a}}_{SRP} = \frac{\delta \mathcal{R}_{SRP}}{\delta \vec{\boldsymbol{r}}} \tag{4.61}$$

4.5 PERTURBED TWO-BODY PROBLEM

We have discussed the gravitational potential and the perturbations model to be used for our system, and now we'll present the EOM (Equations Of Motion) that govern the motion of the lofted particle. Note that the CDE potential model is defined for a body-fixed frame inherently which means the accelerations that we get out of it are directly defined for the ARF frame. The same applies for the STBE and SRP perturbing accelerations. This is why we define the equations of motion too in the ARF frame and transform the propagated state to the AIF frame post-simulation.

We use a Lagrangian approach to derive the EOM because once the Lagrangian is formed, it becomes relatively easy to re-write the EOM for a different frame of reference or a different set of coordinates by substituting the relevant transformation equations in the Lagrangian. It is formed as $L = T + \mathcal{U}$, where T is the specific kinetic energy and $\mathcal{U}$ is the full potential of the system and they are given as follows (Scheeres 2016):

$$T = \frac{1}{2}\dot{\vec{\boldsymbol{r}}}_I \cdot \dot{\vec{\boldsymbol{r}}}_I \tag{4.62}$$

$$\mathcal{U} = U + \mathcal{R}_{STBE} + \mathcal{R}_{SRP} \tag{4.63}$$

where $\vec{\boldsymbol{r}}_I$ is the position vector of the particle from the asteroid to the orbiting particle and expressed in the AIF; U is the CDE gravity potential; $\mathcal{R}_{STBE}$ and $\mathcal{R}_{SRP}$ are the perturbing potentials for the Sun's third-body effect and radiation pressure respectively. The EOM is then obtained from the following (Scheeres 2016):

$$\frac{d}{dt}\left(\frac{\delta L}{\delta \dot{x}_i}\right) = \frac{\delta L}{\delta x_i} \tag{4.64}$$

where $(x_i, \dot{x}_i)$ are the position and velocity vector components. We will now evaluate Equation (4.64) for our particular case by first re-stating the Lagrangian with vectors expressed in the ARF. With $(\vec{\boldsymbol{q}}, \dot{\vec{\boldsymbol{q}}})$ denoting the ARF position and velocity vectors respectively, the position vector in the AIF is related to the ARF as $\vec{\boldsymbol{r}} = \phi_B^I \vec{\boldsymbol{q}}$ and the velocity is related as $\dot{\vec{\boldsymbol{r}}} = \phi_I^B \cdot (\dot{\vec{\boldsymbol{q}}} + \vec{\boldsymbol{\omega}} \times \vec{\boldsymbol{q}})$. With these definitions, the Lagrangian is re-written as follows:

$$L = (\dot{\vec{\boldsymbol{q}}} + \vec{\boldsymbol{\omega}} \times \vec{\boldsymbol{q}}) \cdot (\dot{\vec{\boldsymbol{q}}} + \vec{\boldsymbol{\omega}} \times \vec{\boldsymbol{q}}) + \mathcal{U}(\vec{\boldsymbol{q}}) \tag{4.65}$$

where the transformation matrix ϕ_B^I preserves [1] the dot product, as it is orthogonal, and hence is excluded from the equation. The derivative on the right hand side of Equation (4.64), directly in

[1] For two vectors $\vec{\boldsymbol{u}}$ and $\vec{\boldsymbol{v}}$, and an orthogonal matrix Q, $\vec{\boldsymbol{u}} \cdot \vec{\boldsymbol{v}} = (Q\vec{\boldsymbol{u}}) \cdot (Q\vec{\boldsymbol{v}})$

vector form, is evaluated as follows:

$$\frac{\delta L}{\delta \vec{\boldsymbol{q}}} = \frac{1}{2}\left[2\cdot(\dot{\vec{\boldsymbol{q}}} + \vec{\boldsymbol{w}} \times \vec{\boldsymbol{q}})\cdot(\vec{\boldsymbol{\omega}} \times \vec{\mathbf{1}} + \dot{\vec{\boldsymbol{q}}} \times \vec{\mathbf{0}})\right] + \frac{\delta \mathcal{U}}{\delta \vec{\boldsymbol{q}}} \tag{4.66}$$

$$= \dot{\vec{\boldsymbol{q}}}\cdot(\vec{\boldsymbol{\omega}} \times \vec{\mathbf{1}}) + (\vec{\boldsymbol{\omega}} \times \vec{\boldsymbol{q}})\cdot(\vec{\boldsymbol{\omega}} \times \vec{\mathbf{1}}) + \frac{\delta \mathcal{U}}{\delta \vec{\boldsymbol{q}}} \tag{4.67}$$

$$= (\dot{\vec{\boldsymbol{q}}} \times \vec{\boldsymbol{\omega}})\cdot \vec{\mathbf{1}} + \vec{\mathbf{1}}\cdot((\vec{\boldsymbol{\omega}} \times \vec{\boldsymbol{q}}) \times \vec{\boldsymbol{\omega}}) + \frac{\delta \mathcal{U}}{\delta \vec{\boldsymbol{q}}} \tag{4.68}$$

$$= -(\vec{\boldsymbol{\omega}} \times \dot{\vec{\boldsymbol{q}}}) - (\vec{\boldsymbol{\omega}} \times (\vec{\boldsymbol{\omega}} \times \vec{\boldsymbol{q}})) + \frac{\delta \mathcal{U}}{\delta \vec{\boldsymbol{q}}} \tag{4.69}$$

where $\vec{\mathbf{1}}$ and $\vec{\mathbf{0}}$ are vectors of ones and zeros respectively and all other terms have been defined previously. The left hand side of Equation (4.64) is evaluated as follows:

$$\frac{\delta L}{\delta \dot{\vec{\boldsymbol{q}}}} = \dot{\vec{\boldsymbol{q}}} + (\vec{\boldsymbol{\omega}} \times \vec{\boldsymbol{q}}) \tag{4.70}$$

$$\frac{d}{dt}\left(\frac{\delta L}{\delta \dot{\vec{\boldsymbol{q}}}}\right) = \ddot{\vec{\boldsymbol{q}}} + \vec{\boldsymbol{\omega}} \times \dot{\vec{\boldsymbol{q}}} \tag{4.71}$$

Thus, by substituting Equations (4.69) and (4.71) into Equation (4.64), we get the final equations of motion as follows:

$$\ddot{\vec{\boldsymbol{q}}} + 2\cdot \vec{\boldsymbol{\omega}} \times \dot{\vec{\boldsymbol{q}}} + (\vec{\boldsymbol{\omega}} \times (\vec{\boldsymbol{\omega}} \times \vec{\boldsymbol{q}})) = \frac{\delta \mathcal{U}}{\delta \vec{\boldsymbol{q}}} \tag{4.72}$$

$$= \frac{\delta U(\vec{\boldsymbol{q}})}{\delta \vec{\boldsymbol{q}}} + \frac{\delta \mathcal{R}_{STBE}}{\delta \vec{\boldsymbol{q}}} + \frac{\delta \mathcal{R}_{SRP}}{\delta \vec{\boldsymbol{q}}} \tag{4.73}$$

$$\ddot{\vec{\boldsymbol{q}}} + 2\cdot \vec{\boldsymbol{\omega}} \times \dot{\vec{\boldsymbol{q}}} + (\vec{\boldsymbol{\omega}} \times (\vec{\boldsymbol{\omega}} \times \vec{\boldsymbol{q}})) = \frac{\delta U(\vec{\boldsymbol{q}})}{\delta \vec{\boldsymbol{q}}} + \vec{\boldsymbol{a}}_{STBE} + \vec{\boldsymbol{a}}_{SRP} \tag{4.74}$$

In Equation (4.73), the first term denotes the acceleration due to gravity, and the second and the third term denote the perturbing accelerations. Equation (4.74) is thus the final equation of motion used in this thesis.

4.6 PARTICLE INITIAL CONDITIONS

The EOM established in the previous section are difficult to solve analytically and hence we make use of a numerical integrator to propagate the state vector of an orbiting particle in time. To do this, we need to establish robust methods for providing initial conditions. These initial conditions basically form the state vector with which the particle is lofted from the surface of an asteroid.

4.6.1 LAUNCH LOCATION

This section will present a method to efficiently calculate the launch location of a particle, in the form of a Cartesian position vector from the centre of the asteroid. The formulation is such that the resulting position vector will always point to a location on the surface of the asteroid.

Consider the equation for the ellipsoid given as follows:

$$\frac{x^2}{\alpha^2} + \frac{y^2}{\beta^2} + \frac{z^2}{\gamma^2} = 1 \tag{4.75}$$

where (x, y, z) is the coordinate of any point *on* the surface. An alternate way of writing Equation (4.75), in vector format, is given as follows:

$$\vec{\boldsymbol{r}}.E.\vec{\boldsymbol{r}} = 1 \tag{4.76}$$

$$E = \begin{bmatrix} 1/\alpha^2 & 0 & 0 \\ 0 & 1/\beta^2 & 0 \\ 0 & 0 & 1/\gamma^2 \end{bmatrix} \tag{4.77}$$

where $\vec{\boldsymbol{r}}$ is a general position vector expressed in the ARF and (α, β, γ) are the semi-major axes of the triaxial ellipsoid model of the asteroid. Continuing with Equation (4.76):

$$\vec{\boldsymbol{r}}.\vec{\boldsymbol{r}} = \frac{1}{E} \tag{4.78}$$

$$r^2 = \frac{1}{\hat{\boldsymbol{u}}.E.\hat{\boldsymbol{u}}} \tag{4.79}$$

where $\hat{\boldsymbol{u}}$ is a unit vector expressed in ARF, pointing in the direction of the launch location from the asteroid's centre, with components (u_x, u_y, u_z). The unit vector can be stated in terms of the latitude (δ) and longitude (λ) of the launch point as follows:

$$\hat{\boldsymbol{u}} = \cos\delta\cos\lambda\hat{\boldsymbol{x}} + \cos\delta\sin\lambda\hat{\boldsymbol{y}} + \sin\delta\hat{\boldsymbol{z}} \tag{4.80}$$

where $(\hat{\boldsymbol{x}}, \hat{\boldsymbol{y}}, \hat{\boldsymbol{z}})$ are the basis vectors forming the ARF. Thus, Equation (4.79) can be written as:

$$r^2 = \frac{1}{(u_x^2/\alpha^2) + (u_y^2/\beta^2) + (u_z^2/\gamma^2)} \tag{4.81}$$

The final position vector to the launch location, from the origin of ARF or the asteroid's centre, is given as follows:

$$\vec{\boldsymbol{r}}_s = r\hat{\boldsymbol{u}} \tag{4.82}$$

where r is obtained from Equation (4.81). Thus, just by specifying the latitude and longitude of any desired launch point, the position vector to it is obtained. This, thus, acts as the initial position state of the particle.

4.6.2 LAUNCH VELOCITY

Once we know the position of the particle, we need to provide an initial velocity to launch it into an orbit around the asteroid. But this has to do much more than just providing a velocity magnitude. The velocity magnitude is accompanied by a launch direction which is defined by two angles, namely, *Launch Azimuth* (η) and *Launch Declination* (χ).

These angles can be understood as follows. Suppose you are standing on the surface of an asteroid and you throw a ball. Now the ball will be associated with a velocity vector and if we take the projection of this vector onto the local surface, then the angle between this projection and the local direction to the North pole of the asteroid is defined as the launch azimuth. The angle that the velocity vector itself makes with the local normal is then defined as the launch declination. By keeping a constant angle of declination and varying the launch azimuth from 0° to 360°, we can create a cone of particles, thus replicating how impact ejecta would launch out. An example of this is given in Figure 4.10.

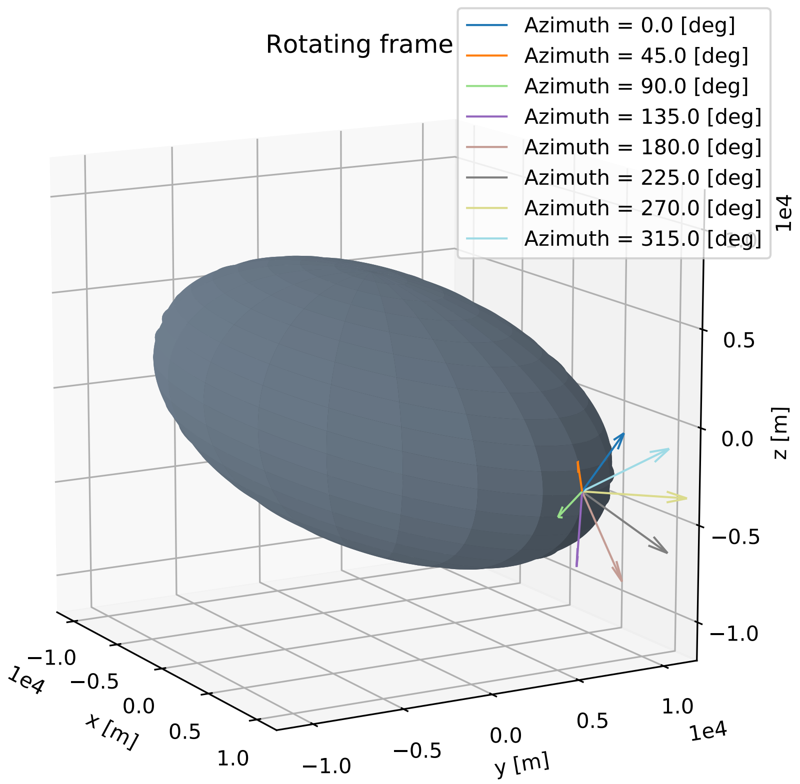

(a)

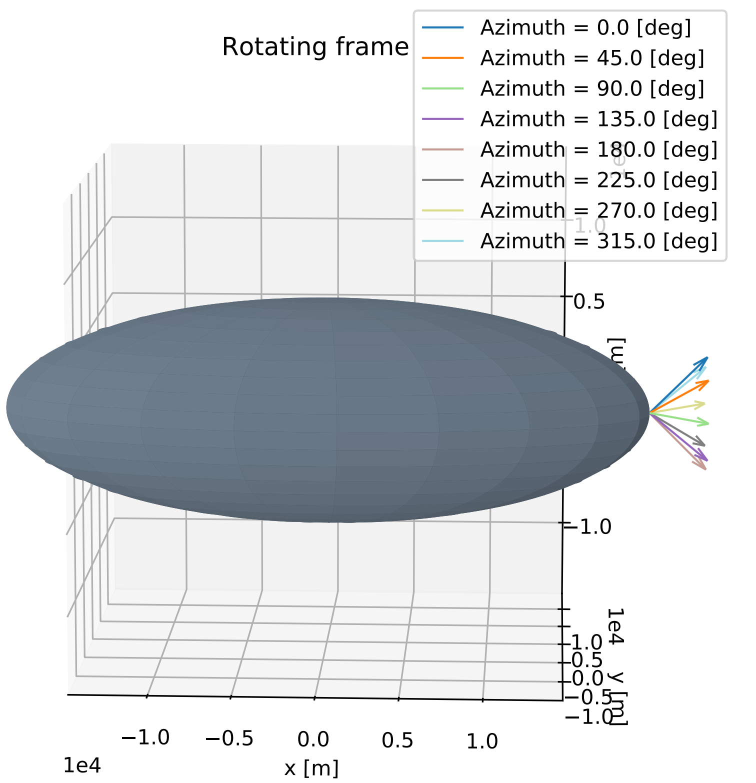

(b)

Figure 4.10: Various velocity vectors depicted at the longest edge of the ellipsoid shaped asteroid i.e. for a launch location longitude and latitude of 0°. Figure 4.10a depicts the front view of multiple velocity vectors spaced at 45° azimuth from each other and at a constant declination of 45°. All vectors are expressed in the rotating frame or the ARF. Figure 4.10b depicts the lateral view of the same velocity vectors.

We will now discuss how the velocity vectors are formed in practice. Consider the equation for a triaxial ellipsoid given in Equation (4.75). Now for any given point (x, y, z) on the surface of the ellipsoid, the normal vector ($\vec{\boldsymbol{n}}$) (and subsequently the unit normal vector ($\hat{\boldsymbol{n}}$)) to it is found by taking the gradient of Equation (4.75):

$$\vec{\boldsymbol{n}} = \frac{2x}{\alpha^2}\hat{\boldsymbol{i}} + \frac{2y}{\beta^2}\hat{\boldsymbol{j}} + \frac{2z}{\gamma^2}\hat{\boldsymbol{k}} \tag{4.83}$$

$$\hat{\boldsymbol{n}} = \frac{\vec{\boldsymbol{n}}}{|\vec{\boldsymbol{n}}|} \tag{4.84}$$

where both $\vec{\boldsymbol{n}}$ and $\hat{\boldsymbol{n}}$ are expressed in the ARF, whose basis vectors are denoted here as $(\hat{\boldsymbol{i}}, \hat{\boldsymbol{j}}, \hat{\boldsymbol{k}})$. Note that since the body in question is not a sphere, the normal vector at the launch location and the radial unit vector $\hat{\boldsymbol{R}}$ (from the centre of the ellipsoid to the launch location) may not always coincide. Now that we know the unit normal vector to the launch location, we need to find the local North direction. This is done by performing the following calculations successively:

$$\hat{\boldsymbol{R}} = \frac{\vec{\boldsymbol{r}}_s}{|\vec{\boldsymbol{r}}_s|} \tag{4.85}$$

$$\hat{\boldsymbol{T}} = \frac{\hat{\boldsymbol{R}} \times \hat{\boldsymbol{k}}}{|\hat{\boldsymbol{R}} \times \hat{\boldsymbol{k}}|} \tag{4.86}$$

$$\hat{\boldsymbol{x}} = \frac{\hat{\boldsymbol{T}} \times \hat{\boldsymbol{n}}}{|\hat{\boldsymbol{T}} \times \hat{\boldsymbol{n}}|} \tag{4.87}$$

$$\tag{4.88}$$

where $\vec{\boldsymbol{r}}_s$ is the position vector to the launch location from the centre of the asteroid; $\hat{\boldsymbol{T}}$ is the tangential unit vector (tangential to the local surface at the local point); $\hat{\boldsymbol{x}}$ is the unit vector that is pointing towards the local North. This formulation works for any point on the surface of the asteroid to give the local North's direction except for the two poles and as such an alternative definition for them has to be used which will be defined later. Note that all the unit vectors discussed so far are expressed in the ARF.

$\hat{\boldsymbol{x}}$ is also viewed as the x-axis basis vector for a frame of reference fixed and centered at the launch location. This frame of reference is termed as the SF (Surface Frame). Note that the SF is not used to define the orbital motion of the regolith and hence it is not one of the standard reference frames. This is why it wasn't mentioned in Section 4.2 and is only defined here since it's use is only for obtaining the velocity vector. The z-axis of SF is defined in the direction of the unit normal vector at the launch location and the y-axis is obtained by following the right-hand rule to form the orthogonal frame. The SF is shown in Figure 4.11.

Note that the basis vectors of the SF are expressed in the ARF and thus their components are defined as follows:

$$\hat{\boldsymbol{x}} = x_1\hat{\boldsymbol{i}} + x_2\hat{\boldsymbol{j}} + x_3\hat{\boldsymbol{k}} \tag{4.89}$$

$$\hat{\boldsymbol{y}} = y_1\hat{\boldsymbol{i}} + y_2\hat{\boldsymbol{j}} + y_3\hat{\boldsymbol{k}} \tag{4.90}$$

$$\hat{\boldsymbol{z}} = z_1\hat{\boldsymbol{i}} + z_2\hat{\boldsymbol{j}} + z_3\hat{\boldsymbol{k}} \tag{4.91}$$

Then the velocity vector components in ARF are obtained as follows:

$$v_x = V.\left[x_1 \cos\eta \sin\chi + y_1 \sin\eta \sin\chi + z_1 \cos\chi\right] \tag{4.92}$$

$$v_y = V.\left[x_2 \cos\eta \sin\chi + y_2 \sin\eta \sin\chi + z_2 \cos\chi\right] \tag{4.93}$$

$$v_z = V.\left[x_3 \cos\eta \sin\chi + y_3 \sin\eta \sin\chi + z_3 \cos\chi\right] \tag{4.94}$$

where V is the magnitude of the velocity chosen manually at the start of the simulation. Thus in this manner, and for the same velocity magnitude, we can simulate particles being launched in different directions from the same launch location, which in turn helps us understand the role of launch direction in the final fate of ejecta.

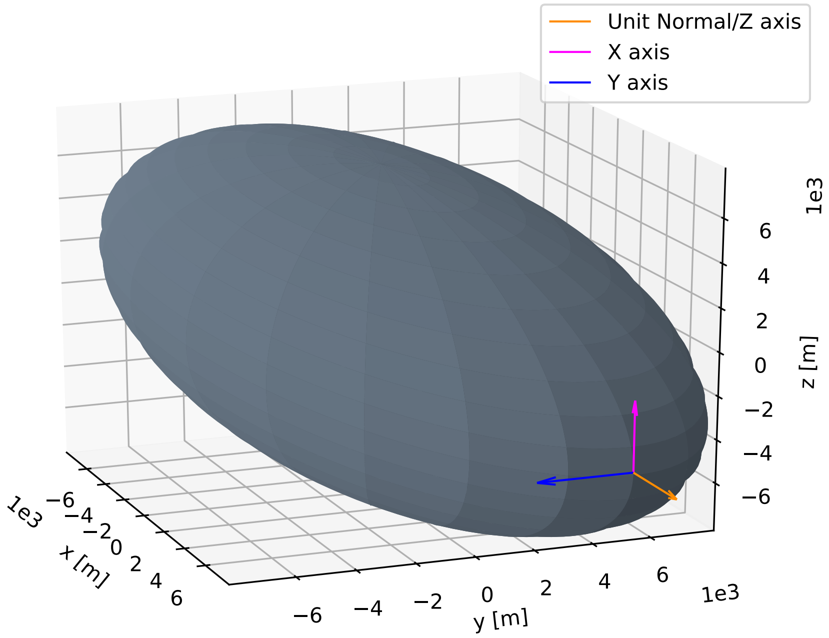

Figure 4.11: An example of the SF at the launch location of latitude and longitude 0° i.e. the longest edge of the asteroid. The x-axis points to the local North; z-axis is in the direction of the unit normal vector at the launch location; and finally the y-axis completes right-hand rule orthogonal frame.

As said earlier, the x-basis vector for the SF can not be defined by the method described previously for launch locations on the two poles of the asteroid. Hence we use two alternate definitions for the x-basis vector in those scenarios however all other computations remain the same as described before. If the launch location is the North pole, then the x-basis vector of the SF is defined as $\hat{\boldsymbol{x}} = [1, 0, 0]$ and for South pole it is defined as $\hat{\boldsymbol{x}} = [-1, 0, 0]$.

4.7 NON-CONSERVATIVE GUARANTEE ESCAPE SPEED

Up until now we discussed the dynamics involved with the particle motion around an asteroid and we also devised methods to launch regolith from the surface into an orbit. It was mentioned earlier that the thesis has employed a full numerical simulation approach to the problem at hand, but while doing that we did attempt at finding a new analytical method to determine a non-conservative guarantee escape speed.

The conservative guarantee escape speed method is obtained by making use of the maximum gravitational potential, between the actual potential of the irregular body and an equivalent point mass potential, at the location of the launch of the particle. If the launch speed is above the conservative guarantee escape speed, then the particle will escape immediately after launch. The conservative guaranteed escape speed method works best for uniform gravity field models, as we'll see later in Section 7.1.1, but fails when one accounts for non-uniform gravity field models such as the CDE model.

We will first understand how the conventional guarantee escape speed is obtained since it will help us in understanding the method for the non-conventional guarantee escape speed later on. The inertial velocity of a particle which is resting on an asteroid's surface is given as $\vec{\boldsymbol{v}}_I = \vec{\boldsymbol{\omega}} \times \vec{\boldsymbol{r}}$, where $\vec{\boldsymbol{r}}$ is the location to the particle from the centre of the asteroid. The resulting vector is pointing outwards from the asteroid if the launch location is on the leading edge of the asteroid and inwards if the launch location is on the trailing edge of the asteroid (Scheeres 2016). The idea is easily depicted in Figure 4.12.

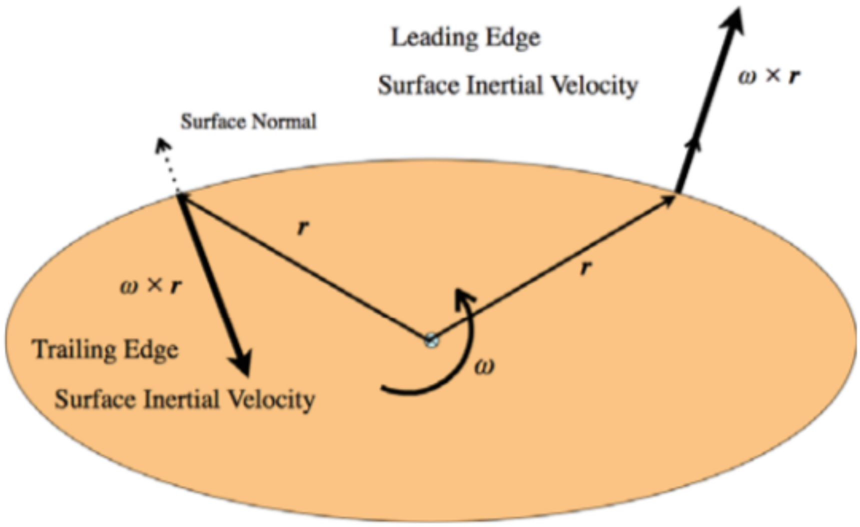

Figure 4.12: Schematic for inertial velocity at the surface for different launch locations (Scheeres 2016).

The idea now is to provide an additional launch speed, for instance in the normal direction, that would result in an escape scenario for the particle. The inertial velocity can then be expressed as follows (Scheeres 2016):

$$\vec{\boldsymbol{v}}_I = v_e \hat{\boldsymbol{n}} + \vec{\boldsymbol{\omega}} \times \vec{\boldsymbol{r}} \tag{4.95}$$

where $v_e \hat{\boldsymbol{n}}$ is the velocity, expressed in ARF, with which a particle is launched in the normal direction such that the particle is on an escape trajectory. All other terms have been defined previously. The conservative approach is to equate $\vec{\boldsymbol{v}}_I$ to $\sqrt{2U_{max}}$ where $U_{max} = max[U(\vec{\boldsymbol{r}}), \mu/\vec{\boldsymbol{r}}]$ (Scheeres 2016). Equation (4.95) can then be re-written as follows:

$$\sqrt{2U_{max}} = v_e \hat{\boldsymbol{n}} + \vec{\boldsymbol{\omega}} \times \vec{\boldsymbol{r}} \tag{4.96}$$

$$2U_{max} = v_e^2 + (\vec{\boldsymbol{\omega}} \times \vec{\boldsymbol{r}})^2 + 2v_e(\hat{\boldsymbol{n}} \cdot (\vec{\boldsymbol{\omega}} \times \vec{\boldsymbol{r}})) \tag{4.97}$$

Equation (4.97) is a quadratic equation in v_e and can be solved as follows:

$$v_e = \frac{-2(\hat{\boldsymbol{n}} \cdot (\vec{\boldsymbol{\omega}} \times \vec{\boldsymbol{r}})) \pm \sqrt{4(\hat{\boldsymbol{n}} \cdot (\vec{\boldsymbol{\omega}} \times \vec{\boldsymbol{r}}))^2 + 4(2U_{max}) - 4(\vec{\boldsymbol{\omega}} \times \vec{\boldsymbol{r}})^2}}{2} \tag{4.98}$$

$$v_e = -(\hat{\boldsymbol{n}} \cdot (\vec{\boldsymbol{\omega}} \times \vec{\boldsymbol{r}})) \pm \sqrt{(\hat{\boldsymbol{n}} \cdot (\vec{\boldsymbol{\omega}} \times \vec{\boldsymbol{r}}))^2 + 2U_{max} - (\vec{\boldsymbol{\omega}} \times \vec{\boldsymbol{r}})^2} \tag{4.99}$$

Since the speed can't be negative, the formula is re-written as:

$$v_e = -(\hat{\boldsymbol{n}} \cdot (\vec{\boldsymbol{\omega}} \times \vec{\boldsymbol{r}})) + \sqrt{(\hat{\boldsymbol{n}} \cdot (\vec{\boldsymbol{\omega}} \times \vec{\boldsymbol{r}}))^2 + 2U_{max} - (\vec{\boldsymbol{\omega}} \times \vec{\boldsymbol{r}})^2} \tag{4.100}$$

Equation (4.100) thus gives the conservative escape speed, expressed in the ARF, for a particle launched in the normal direction. The equation is equally applicable for a particle launched in any general direction as well by substituting $\hat{\boldsymbol{n}}$ with the unit vector for the direction in which the launch takes place. Thus if a particle is launched with a velocity above or equal to the one mentioned in Equation (4.100), then it would result in a guaranteed escape situation.

Now for a non-conservative approach, we will not use $\vec{\boldsymbol{v}}_I = \sqrt{2U_{max}}$ to get a guaranteed escape launch speed. We will derive an alternate relation for $\vec{\boldsymbol{v}}_I$ first and then later on substitute it back into Equation (4.100) in place of $2U_{max}$ to get the non-conservative guaranteed escape launch speed.

Consider the EOM mentioned in Equation (4.74), with the exception that we only consider the gravitational potential and remove all external perturbations on the left hand side of the equation. These equations do not have an explicit dependence on time which means that the Jacobian for the system exists and is conserved (Scheeres 2016). The Jacobian, expressed in the ARF, is given as follows (Scheeres 2016):

$$J = \frac{1}{2}v_B^2 - \frac{1}{2}\omega^2(x^2+y^2) - U(\vec{\boldsymbol{r}}) \tag{4.101}$$

where v_B is the velocity of the particle in the ARF; ω is the magnitude of the angular velocity of the rotating asteroid and is along the z-axis of the ARF; (x, y) are the x-y coordinate of the orbiting particle; $U(\vec{\boldsymbol{r}})$ is the small-body gravitational potential, which in our case is the CDE potential model. From transport theorem, we use the relation between an inertial velocity and the rotating frame velocity:

$$\vec{\boldsymbol{v}}_B = \vec{\boldsymbol{v}}_I - (\vec{\boldsymbol{\omega}} \times \vec{\boldsymbol{r}}) \tag{4.102}$$
$$v_B^2 = v_I^2 + (\vec{\boldsymbol{\omega}} \times \vec{\boldsymbol{r}})^2 - 2\vec{\boldsymbol{v}}_I \cdot (\vec{\boldsymbol{\omega}} \times \vec{\boldsymbol{r}}) \tag{4.103}$$
$$v_B^2 = v_I^2 + (\vec{\boldsymbol{\omega}} \times \vec{\boldsymbol{r}})^2 - 2\vec{\boldsymbol{\omega}} \cdot (\vec{\boldsymbol{r}} \times \vec{\boldsymbol{v}}_I) \tag{4.104}$$
$$v_B^2 = v_I^2 + (\vec{\boldsymbol{\omega}} \times \vec{\boldsymbol{r}})^2 - 2\vec{\boldsymbol{\omega}} \cdot \vec{\boldsymbol{H}} \tag{4.105}$$

where $\vec{\boldsymbol{H}}$ is the angular momentum of the orbiting particle. We substitute Equation (4.105) back into Equation (4.101) to get the following relation:

$$J = \frac{1}{2}v_I^2 - \vec{\boldsymbol{\omega}} \cdot \vec{\boldsymbol{H}} - U(\vec{\boldsymbol{r}}) \tag{4.106}$$

Considering that after launch the particle is on a parabolic trajectory such that it barely escapes then in such a case the energy of the particle would be 0 which reduces the Jacobian to $J_\infty = -\vec{\boldsymbol{\omega}} \cdot \vec{\boldsymbol{H}}_\infty$. Now at the instance of the launch, the Jacobian is expressed as follows:

$$J_0 = \frac{1}{2}v_{I_0}^2 - \vec{\boldsymbol{\omega}} \cdot \vec{\boldsymbol{H}}_0 - U(\vec{\boldsymbol{r}}_0) \tag{4.107}$$

Since the Jacobian is conserved, $J_0 = J_\infty$, which means we can write the following relation:

$$\frac{1}{2}v_{I_0}^2 - \vec{\boldsymbol{\omega}} \cdot \vec{\boldsymbol{H}}_0 - U(\vec{\boldsymbol{r}}_0) = -\vec{\boldsymbol{\omega}} \cdot \vec{\boldsymbol{H}}_\infty \tag{4.108}$$

For parabolic trajectories, the angular momentum magnitude is expressed in terms of the semi-latus rectum and the gravitational parameter of the central body as $H = \sqrt{\mu 2q}$ where q is the periapsis distance (Schaub et al. 2003). Also the angle between the angular momentum vector and the asteroid's rotation vector is the orbit inclination (i) and with these new definitions, Equation (4.108) is re-written as follows:

$$\frac{1}{2}v_{I_0}^2 - \vec{\boldsymbol{\omega}} \cdot \vec{\boldsymbol{H}}_0 - U(\vec{\boldsymbol{r}}_0) = -\omega\cos(i)\sqrt{2\mu q_\infty} \tag{4.109}$$

We will consider only equatorial orbits for now and hence Equation (4.109) can be stated as simply:

$$\frac{1}{2}v_{I_0}^2 - \vec{\boldsymbol{\omega}}\cdot\vec{\boldsymbol{H}}_0 - U(\vec{\boldsymbol{r}}_0) = -\omega\sqrt{2\mu q_\infty} \tag{4.110}$$

$$\frac{1}{2}v_{I_0}^2 - \vec{\boldsymbol{\omega}}\cdot(\vec{\boldsymbol{r}}_0 \times \vec{\boldsymbol{v}}_{I_0}) - U(\vec{\boldsymbol{r}}_0) = -\omega\sqrt{2\mu q_\infty} \tag{4.111}$$

Note we can write $H_0 = \vec{\boldsymbol{r}}_0 \times \vec{\boldsymbol{v}}_{I_0}$, where $\vec{\boldsymbol{r_0}}$ is expressed in ARF, since at time $t = 0$ both ARF and AIF are aligned which means that $\vec{\boldsymbol{r}}_{I_0} = \vec{\boldsymbol{r}}_{B_0}$. The intent now is to solve for v_{I_0} from Equation (4.111), which is the inertial velocity at launch that eventually leads to an escape scenario.

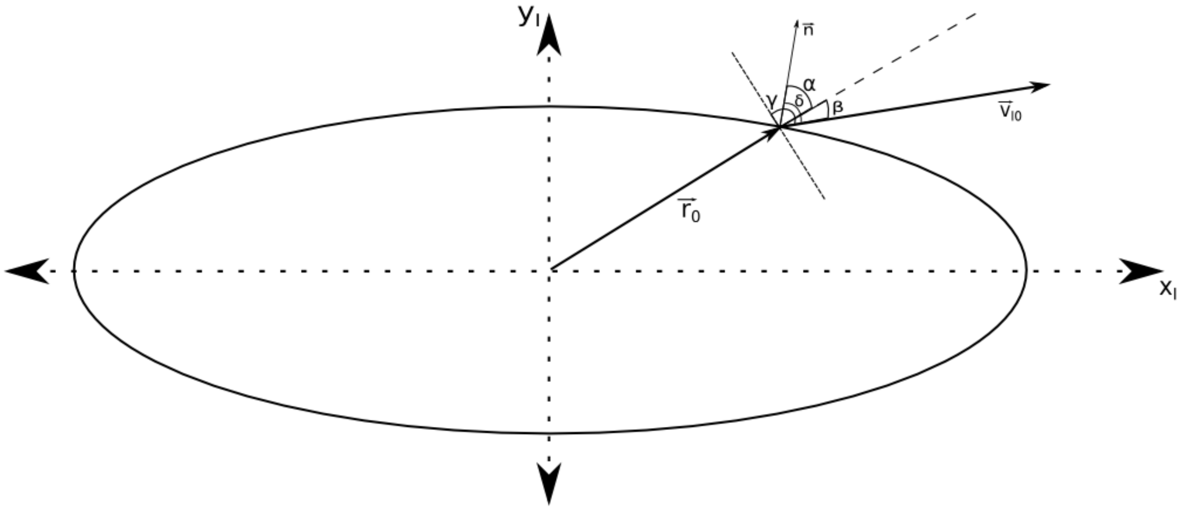

Figure 4.13: General angle definitions for velocity vector with position and normal vector at the launch location.

We need to evaluate the second term on the left hand side of Equation (4.111) using the angle definitions given in Figure 4.13. In that, γ is the angle between the velocity vector and the plane perpendicular to the position vector; δ is the launch declination angle as explained in Section 4.6.2; α is the angle between the normal vector and the position vector direction and finally, β is the angle between the velocity vector and the position vector direction. Using these definitions, the cross product in Equation (4.111) is evaluated as follows:

$$\vec{\boldsymbol{\omega}}\cdot(\vec{\boldsymbol{r}}_0 \times \vec{\boldsymbol{v}}_{I_0}) = \vec{\boldsymbol{\omega}}\cdot(r_0 v_{I_0}\sin(\beta)\hat{\boldsymbol{h}}) \tag{4.112}$$

$$= (r_0 v_{I_0}\sin(\delta-\alpha))\vec{\boldsymbol{\omega}}\cdot\hat{\boldsymbol{h}} \tag{4.113}$$

where $\hat{\boldsymbol{h}}$ specifies the direction of the cross product, i.e. the angular momentum vector $\vec{\boldsymbol{H}}_0$. The angle definitions given in Figure 4.13 remains valid even for a launch location at the trailing edge of the asteroid and hence the angular definitions remain generalized. In addition to having an equatorial orbit, we can further simplify Equation (4.113) by keeping the launch site at the longest edge of the ellipsoid which means that we can make $\alpha = 0$. Thus Equation (4.111) can be re-written as:

$$\frac{1}{2}v_{I_0}^2 - (r_0 v_{I_0}\sin(\delta))\vec{\boldsymbol{\omega}}\cdot\hat{\boldsymbol{h}} - U(\vec{\boldsymbol{r}}_0) = -\omega\sqrt{2\mu q_\infty} \tag{4.114}$$

Equation (4.114) is a quadratic equation in v_{I_0} which is solved to provide the following solution:

$$v_{I_0} = (r_0\sin\delta)\vec{\boldsymbol{\omega}}\cdot\hat{\boldsymbol{h}} \pm \sqrt{((r_0\sin\delta)\vec{\boldsymbol{\omega}}\cdot\hat{\boldsymbol{h}})^2 + 2U - 2\omega\sqrt{2\mu q_\infty}} \tag{4.115}$$

Thus instead of using $v_{I_0} = \sqrt{2U_{max}}$ in Equation (4.97), we use the formula in Equation (4.115) which leads to modifying Equation (4.100) as follows:

$$v_e = -(\hat{\boldsymbol{d}} \cdot (\vec{\boldsymbol{\omega}} \times \vec{\boldsymbol{r}})) + \sqrt{(\hat{\boldsymbol{d}} \cdot (\vec{\boldsymbol{\omega}} \times \vec{\boldsymbol{r}}))^2 + v_{I_0}^2 - (\vec{\boldsymbol{\omega}} \times \vec{\boldsymbol{r}})^2} \tag{4.116}$$

where instead of using $\hat{\boldsymbol{n}}$ we use the unit vector $\hat{\boldsymbol{d}}$, representing a general direction of launch and not just the normal direction. Note that Equations (4.114) and (4.115) are valid only for the launch location at the longest edge of the ellipsoid. We simplified the equations by making $\alpha = 0$ so that testing this approach for a non-conservative guaranteed escape speed can be made easy, however the approach can be generalized by using a non-zero value for α in Equation (4.113) as well.

4.8 CONCLUSION

5

NAOS: NEAR-ASTEROID ORBIT SIMULATOR

6

VERIFICATION & VALIDATION

In this chapter, we will present the results on verification and validation of the simulator discussed in Chapter 5. We verify the gravity model, the launch conditions for the regolith, the numerical integrator along with the equations of motion for the regolith, and finally the Solar perturbation models. We validate our simulator to ensure that our inferences for any scientific result out of it remains true and valid as well.

6.1 CONSTANT DENSITY ELLIPSOID GRAVITY MODEL

The CDE gravity model was tested for a singular target point by comparing the gravitational potential and acceleration values at that point as computed by NAOS (Near-Asteroid Orbit Simulator), with external data obtained from another researcher at CSML [1]. The parameters used for the test are given in Table 6.1.

Table 6.1: Parametric values used for testing the CDE gravitational potential model.

Parameter	Value	Units
Gravitational Parameter	446382.0	m^3/s^2
Alpha (longest axis of CDE)	20000	m
Beta (Intermediate axis of CDE)	7000	m
Gamma (Shortest axis of CDE)	7000	m
Target point x-coordinate	10000	m
Target point y-coordinate	13000	m
Target point z-coordinate	8000	m

The test values for the gravitational potential and the acceleration values at the specified target point are given in Table 6.2.

[1] Centre for Spaceflight Mechanics Laboratory; The thesis work was partly done at CSML, which is a research lab headed by Dr. Daniel Scheeres and is part of the University of Colorado, Boulder, USA.

Table 6.2: Test values for verification of the CDE gravity model.

Parameter	Value		Units
Gravitational Potential	23.710052554396402		m^2/s^2
Gravitational Acceleration	x	-0.00044762916738340803	m/s^2
	y	-0.0009623388813999501	m/s^2
	z	-0.000592208542399969	m/s^2

The values obtained from the simulator NAOS were compared with the ones in Table 6.2 upto the 12th decimal point and they matched, validating the gravity model implemented in NAOS.

6.2 REGOLITH LAUNCH CONDITIONS

In this section, we'll presents results on verifying whether the initial state vector for the regolith or the launch condition match to what is desired by the user. Here, an internal validation is done to ensure that the launch conditions registered in the output database match the raw value input to NAOS. We present graphical and numerical results in this regard.

6.2.1 LAUNCH LOCATION

The position vector to the launch location, from the centre of the ARF, is formed by giving only the launch location latitude and longitude as input. Thus, we have to verify whether the position vector conforms to a given angular input. We take the initial state vector, from the output databases of the dynamics simulator, of regolith launched from a few launch locations on the asteroid and convert the Cartesian coordinates back to latitude and longitude to see if the position vector was formed correctly. For the same Cartesian coordinates, we use the triaxial ellipsoid equation, and see if they solve the equation, to verify that the launch point lies on the surface of the asteroid.

We took 5 test locations from where regolith was launched and separately calculated the corresponding longitude and latitude for the launch location to check if the position vector was correctly formed. The position coordinates and the back-calculated latitude and longitude angles are shown in Table 6.3.

Table 6.3: Position vector to different launch locations and the corresponding Latitude and Longitude angles.

X [m]	Y [m]	Z [m]	Longitude [deg]	Latitude [deg]
20000.0	0.0	0.0	0.0	0.0
0.0	7000.0	0.0	90.0	0.0
0.0	0.0	7000.0	0.0	90.0
3316.14545023	1914.57746836	6632.29090046	30.0	60.0
-3961.38284482	-3961.38284482	5602.2413449	-135.0 (225.0)	45.0

The longitude and latitude values given in Table 6.3 were calculated from the Cartesian coordinates and match those given as inputs to the dynamics simulator. The position vectors from Table 6.3 with the CDE model are also depicted in Figure 6.1.

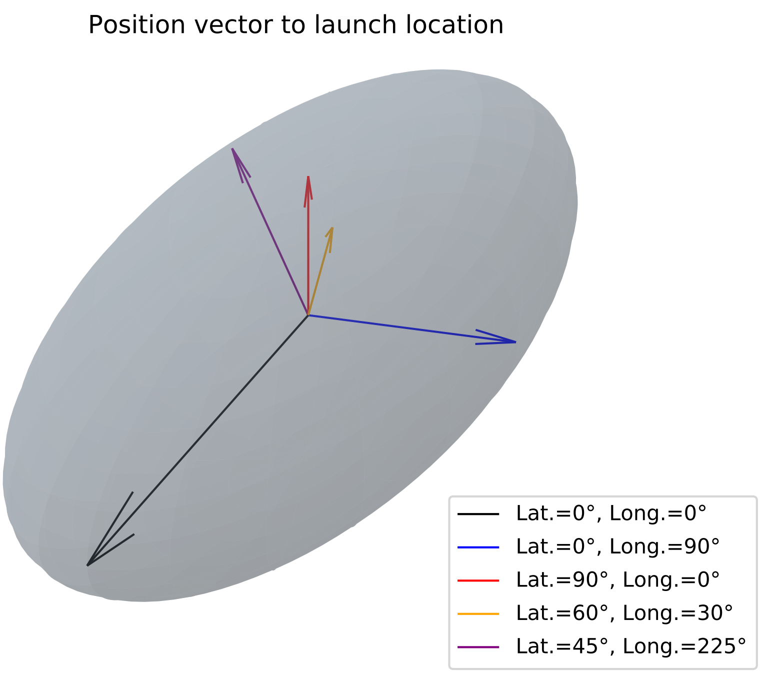

(a)

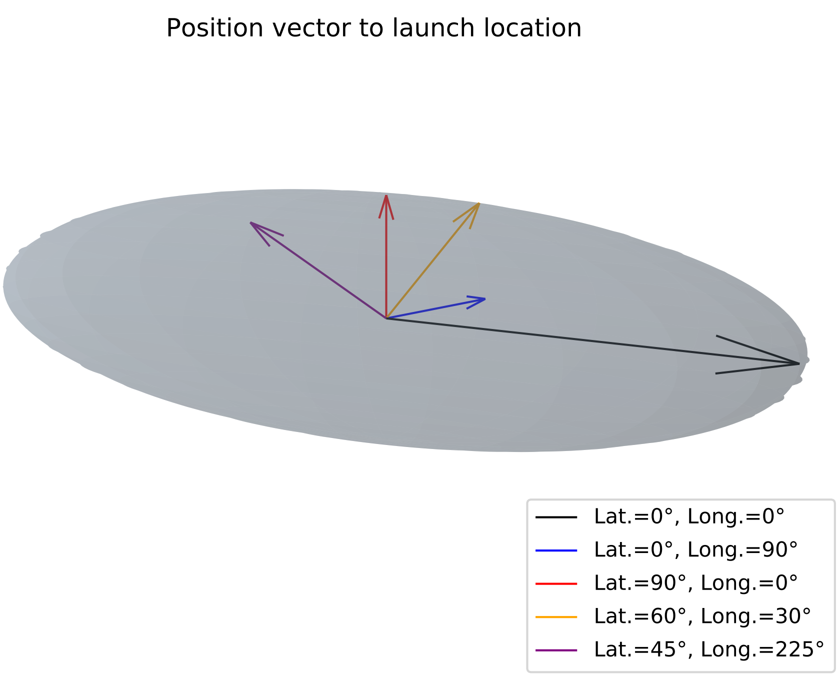

(b)

Figure 6.1: Position vectors from Table 6.3 shown with the CDE asteroid model.

We also checked whether the launch location in fact did lie exactly on the surface of the CDE asteroid and not inside or above the surface. This is really important because a wrong initial condition could produce erroneous results. Once we substitute the Cartesian coordinates into the triaxial ellipsoid equation (see Equation (4.75)) and if the output equals zero (when we take the term 1.0 on the right hand side in Equation (4.75)), then the launch point lies on the asteroid. We did an external validation for this but an internal validation always takes place within the dynamics simulator at all times whenever a new simulation is run.

Table 6.4: Output of the triaxial ellipsoid equation for a few test launch location position vectors. An output of 0.0 means that the position vector is a perfect root of the equation and hence the launch location indeed lies on the surface of the asteroid.

X [m]	Y [m]	Z [m]	Output of triaxial ellipsoid equation
20000.0	0.0	0.0	0.0
0.0	7000.0	0.0	0.0
0.0	0.0	7000.0	0.0
3316.14545023	1914.57746836	6632.29090046	2.22044604925e-16
-3961.38284482	-3961.38284482	5602.2413449	0.0

6.2.2 LAUNCH VELOCITY

The launch velocity vector is formed by providing two angles and a magnitude. As explained in Section 4.6.2, the two angles are the declination angle from the normal vector at the launch location and the azimuth angle from the local North direction. The local North direction and the normal vector, in essence, act as the basis vectors for a local surface frame of reference which in turn help in the mathematical formulation of the velocity vector of Cartesian components. Since we are dealing with an ellipsoid and not a sphere, defining local North is not a straight-forward process as explained earlier in Section 4.6.2.

Thus, we first begin with verifying our methodology of forming the local surface frame, and ensure that the local Normal vector and the local North pointing vector are correctly formed and their lies no discrepancy. Then we verify whether the velocity vector, in terms of its Cartesian components, indeed makes the same angle with the surface frame as specified at the input of the simulation. The process for the second verification item is different from how the velocity vector was formed in the first place and hence the verification itself won't be a tampered or faulty process.

Let's first begin with a test launch location at the longest edge of the CDE. A graphical depiction of the frame is shown in Figure 4.11. This is the simplest location to perform any simulation or test because the surface normal vector here will be along the same direction as the position vector to the launch point from the centre of the ellipsoid. This also makes the test in itself a trivial task. Note that the surface normal is also the z-axis for the surface frame at the launch point. So for the current test location, if the cross product of the normal and the position vector is a zero vector, then the normal vector is verified. Table 6.5 shows the result for this. Following this, if the angle between the normal vector and the x-axis basis vector for the surface frame is 90°, then the latter is pointing to the local North direction. This is because for the current test location, any vector perpendicular to the surface normal (or effectively to the launch location position vector) will be along the 0° meridian line crossing the test location. A simple dot product (again shown in Table 6.5) between the x-axis basis vector of the surface frame and the normal vector will tell us if they are perpendicular to each other or not.

Table 6.5: Surface frame verification at the longest edge of the ellipsoid

Unit Vector	Components			Operations
	x	y	z	
Position ($\hat{\boldsymbol{r}}$)	1.0	0.0	0.0	$\hat{\boldsymbol{r}} \times \hat{\boldsymbol{n}}$ = [0.0, 0.0, 0.0]
Normal ($\hat{\boldsymbol{n}}$)	1.0	0.0	0.0	
X-axis Surface frame / local North direction ($\hat{\boldsymbol{x}}$)	0.0	0.0	1.0	$\hat{\boldsymbol{x}} \cdot \hat{\boldsymbol{n}} = 0.0$

Now, we perform a more generalized and non-trivial test for the surface frame but this time we choose a more general launch location. A test site was chosen at 30° longitude and 60° latitude. It can be viewed in Figure 6.2. Note that at this location, the surface normal vector and the launch position vector will not be aligned. We begin with first verifying that the x-axis basis vector for the surface frame at the current launch site is pointing to North. Another way of stating this is that this vector is tangential to the meridian line, which is running all the way up to the poles. If the x-axis basis vector is indeed tangential to the local meridian, then its x-y plane projection will be collinear to that of the position vector to the launch site.

Table 6.6: Surface frame verification for test launch location at 30° Longitude and 60° Latitude, i.e., on the leading edge of the asteroid.

Unit Vector	Components			Operations
	x	y	z	
Position ($\hat{\boldsymbol{r}}$)	0.4330127	0.25	0.8660254	$\hat{\boldsymbol{x}}_x / \hat{\boldsymbol{r}}_x == \hat{\boldsymbol{x}}_y / \hat{\boldsymbol{r}}_y$
X-axis Surface frame / local North direction ($\hat{\boldsymbol{x}}$)	-0.8496329	-0.49053578	0.1936455	= -1.9621431353
Normal ($\hat{\boldsymbol{n}}$)	0.05874547	0.27687111	0.95910967	$\hat{\boldsymbol{n}} \cdot \hat{\boldsymbol{x}} = 0.0$

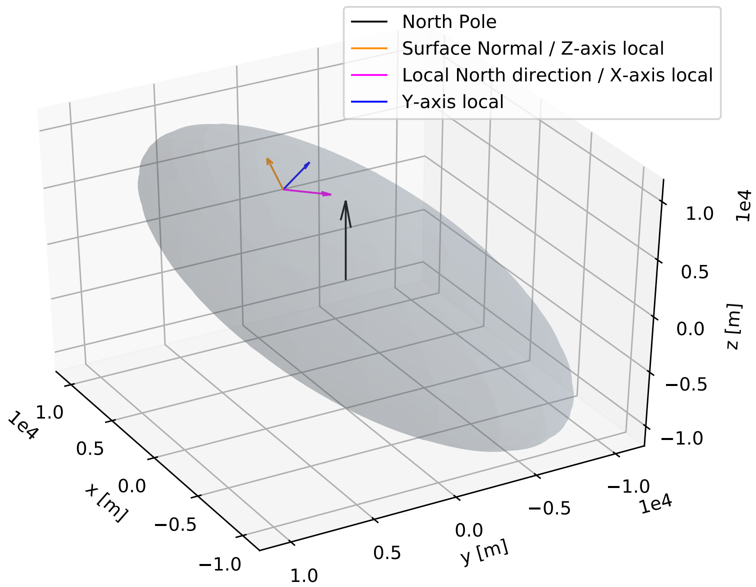

Figure 6.2: Surface frame depicted for test launch located at 30° Longitude and 60° Latitude. Note that the longitude is measured in anti-clockwise direction from the +X axis in the figure.

We can prove the two projections to be collinear if the x and the y components of the vectors form equal ratios. This is shown in Table 6.6. We see that the ratios are equal and hence the x-axis basis vector is pointing to the North direction. Following this, we can also say that the normal vector at this location is formulated correctly since it is perpendicular to the x-axis basis vector (which in turn is tangential to the meridian line). A vector perpendicular to the meridian line will in-fact be the surface normal vector. Note that, we haven't explicitly verified the y-axis basis vector of the surface frame because it is formed by cross multiplying the normal and the x-axis basis vector. So it inherently remains verified if the latter two are formulated correctly.

Now that we have verified that the surface frame is established correctly, we need to verify that the velocity vector makes the correct declination and azimuth angle with the surface frame. The test launch location is still the same as before and the procedure for verification (explained shortly) is different from how the velocity vector was originally formed. We use the vector dot product definition to compute the angle between the velocity vector and the surface normal vector. This gives us the launch declination angle. We then compute the projection of the velocity vector onto the x-y plane of the surface frame [2] and then compute the angle between the projection and the x-axis basis vector of the surface frame. The latter is done, again, by using the dot product method. This then gives us the launch azimuth angle. If the computed angles match the ones provided as input for the simulation, then the velocity vector formulation is verified.

Two particle launches were simulated for the aforementioned verification process. The particles were launched with a velocity of 6.0 [m/s] from a point located on the surface of the CDE asteroid at 30° Longitude and 60° Latitude. The first test involved launching particles at declination and azimuth angles of 30° and 45° respectively. The second test involved declination and azimuth angles of 60° and 135° respectively. The results for these test simulations is shown in Tables 6.7 and 6.8. Figure 6.3 shows the orientation of the velocity vector, for the first test, with respect to the launch site surface frame and the ARF.

Table 6.7: Launch velocity surface frame angles verification data. Input launch declination = 30° and azimuth = 45°.

Vector	**Vector Components**			**Launch Declination [deg]**	**Launch Azimuth [Deg]**
	x	y	z		
Velocity ($\vec{v}$) [m/s]	-0.385325	-1.354695	5.832351	30.0	
Unit Normal	0.058745	0.276871	0.959109		
$\vec{v}$ projection [m/s]	-0.690575	-2.793360	0.848671		45.0
Unit x-axis surface frame	-0.8496329	-0.49053578	0.1936455		

Table 6.8: Launch velocity surface frame angles verification data. Input launch declination = 60° and azimuth = 135°.

Vector	**Vector Components**			**Launch Declination [deg]**	**Launch Azimuth [Deg]**
	x	y	z		
Velocity ($\vec{v}$) [m/s]	5.223625	-0.4029416	2.924273	60.0	
Unit Normal	0.058745	0.276871	0.959109		
$\vec{v}$ projection [m/s]	5.047389	-1.2335549	0.046944		135.0
Unit x-axis surface frame	-0.8496329	-0.4905357	0.1936455		

[2] Given a velocity vector $\vec{v}$ and the surface normal vector $\vec{n}$, the x-y plane projection of $\vec{v}$ is given as: $\vec{v}_{xy} = \vec{v} - \frac{\vec{v}\cdot\vec{n}}{n^2}\vec{n}$

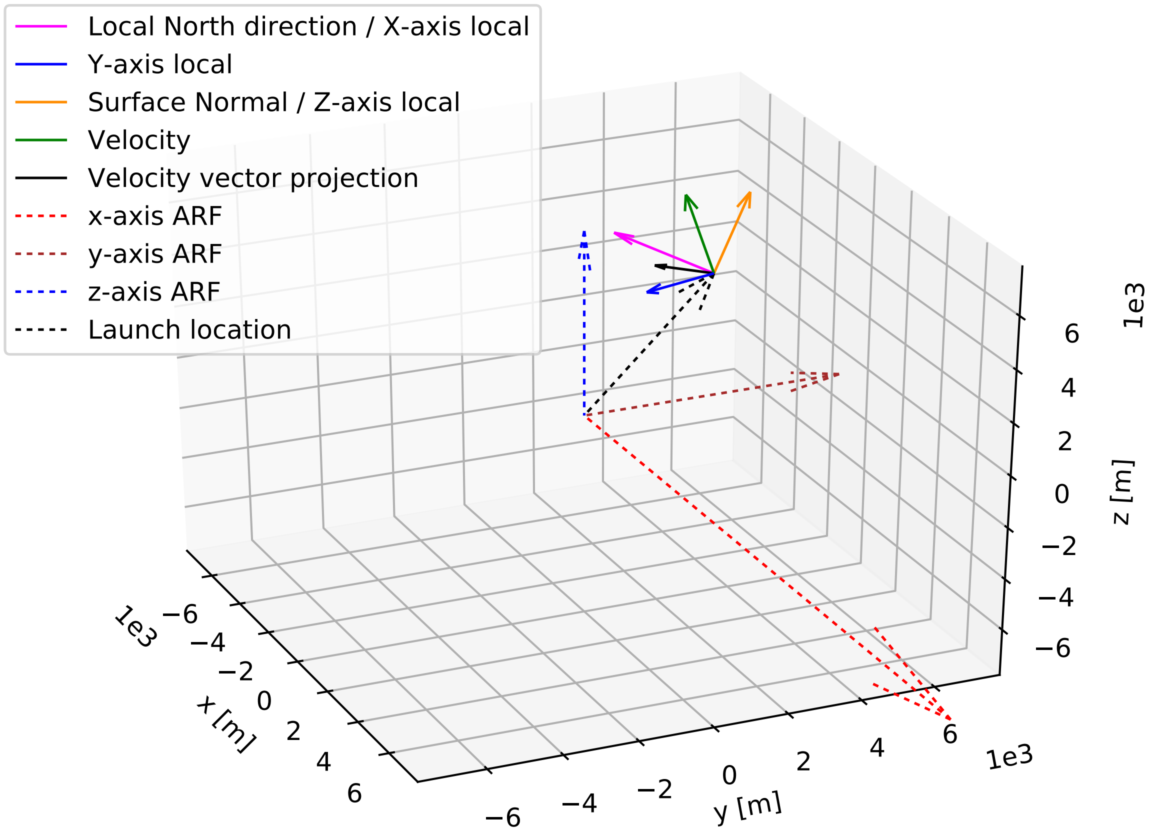

Figure 6.3: Schematic representing the surface frame for launch site at 30° Longitude and 60° Latitude along with the velocity vector and the ARF. The diagram gives an intuition on the orientation of the velocity vector. The launch declination and azimuth angles are 30° and 45° respectively.

6.3 REGOLITH ORBITAL MOTION

In this section, we will present results on test simulations that verify and validate the numerical integration of the equations of motion for the regolith in NAOS, and in extension, the numerical integrator, the gravity potential model and the relatively smaller functional aspects of the simulator. The tests were done by using the CDE gravity potential model, which means that gravity perturbations were accounted for, but excluded the Solar perturbations. This is so that we can test the validity of the simulator by observing the conservation properties of the Jacobi Integral and the Keplerian Energy of an orbiting particle. Both of these would not be conserved if perturbations were included in the test.

6.3.1 SPHERICAL ASTEROID

We first test the simulator for a particle launched from the surface of a spherical asteroid of radius 20 km. The launch site was located at 0° Longitude and Latitude. A single particle was launched with a velocity of 10.0 m/s with an azimuth angle of 135° and declination angle of 45°. Note that the CDE potential model was still used for this simulation with all three semi-major axes made equal to the sphere radii. If the gravity potential model is formulated properly, then with all three semi-major axes being equal, the potential model will act like a point-mass model. This would make the gravity field uniform and hence conserve the Keplerian Energy. The Jacobi integral and the Keplerian energy for this test is shown in Figure 6.4. From the conservation of these values, we can infer that atleast for a spherical asteroid, the simulator works correctly.

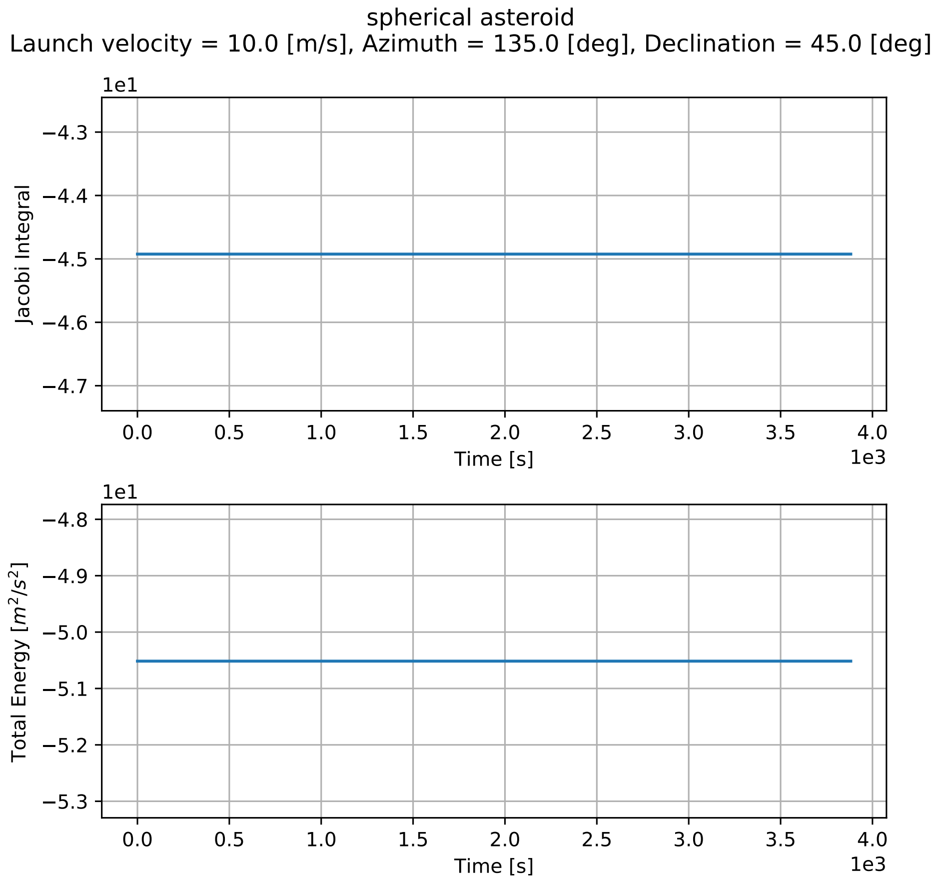

Figure 6.4: Jacobi Integral and Keplerian Energy for the regolith launched from the surface of a spherical asteroid at Latitude and Longitude 0° remains conserved.

6.3.2 CDE ASTEROID

We'll perform a similar test as before but this time for a CDE shaped asteroid of semi-major axes α = 20 km, β = 7 km, γ = 7 km. A single regolith was launched from the surface at site Longitude 30° and Latitude 60°. The particle was launched with a velocity of 10 m/s, azimuth angle of 135° and declination angle of 30°. Now since the gravity potential model is a non-uniform one, unlike that in the case of the spherical asteroid, the Jacobi integral would remain conserved however the Keplerian energy of the particle should not remain conserved. We see this outcome in Figure 6.5. This result further validates the simulator since the Jacobi remains conserved, implying that the equations of motion, the gravity potential model, the numerical integrator and several other background functions of the simulator work correctly.

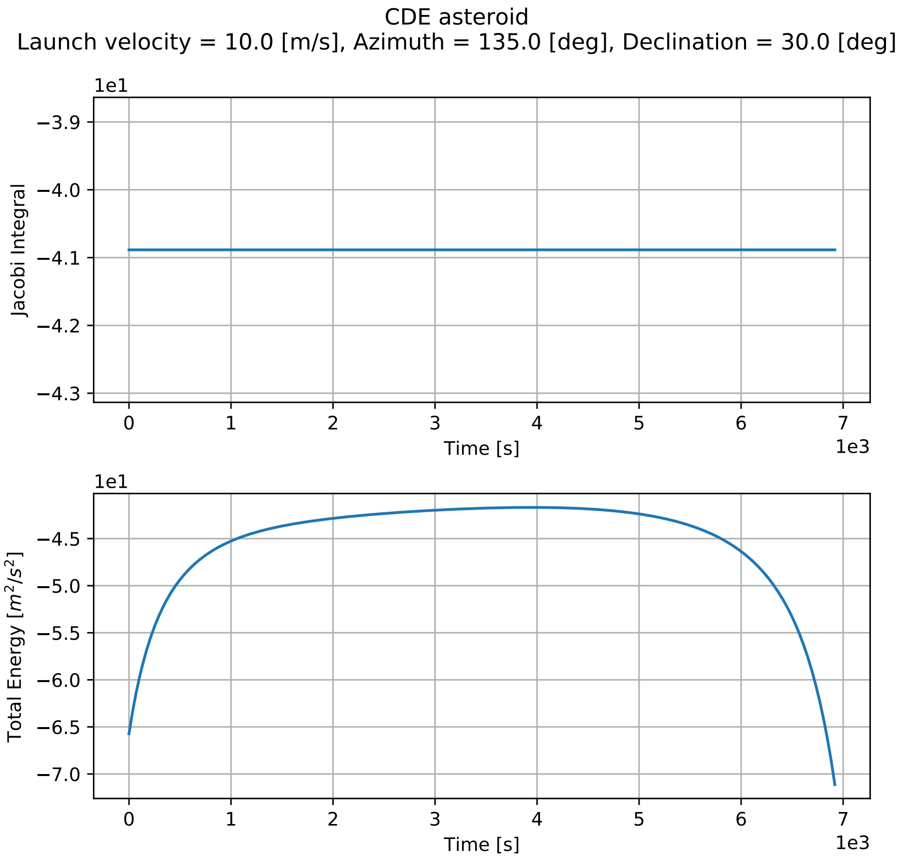

Figure 6.5: Jacobi Integral and Keplerian Energy for the regolith launched from the surface of a CDE shaped asteroid at Latitude 60° and Longitude 30°.

Post this, two other tests were performed from the leading edge of the asteroid, one of which resulted in re-impact and the other which resulted in an escape situation. The Jacobi integral for the two simulation was computed which again turned out to be constant throughout the duration of the respective trajectories. The results and initial conditions for the re-impact case are shown in Figure 6.6 and for the escape case are shown in Figure 6.7. The launch declination in both cases is 45°. The results further validate the functionality of the simulator.

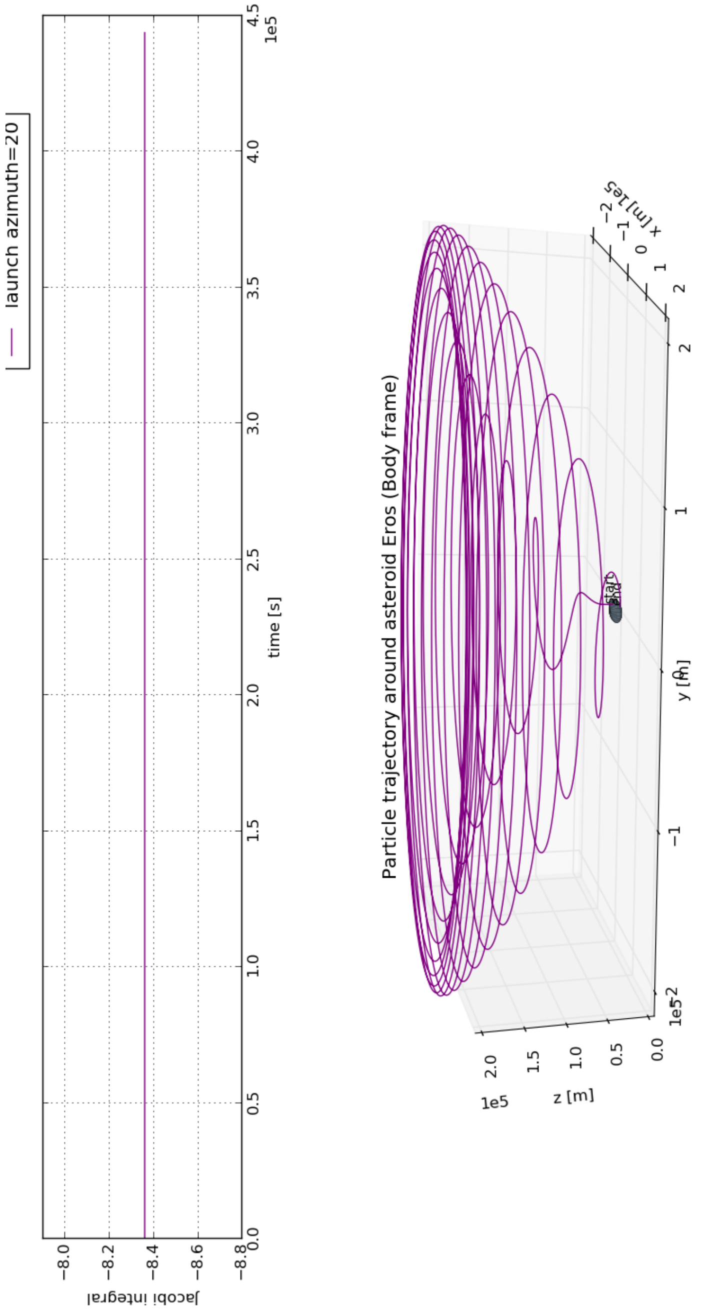

Initial X coordinate	4804.78756138	[m]
Initial Y coordinate	4804.78756138	[m]
Initial Z coordinate	4804.78756138	[m]
Initial X velocity	-1.37701356924	[m/s]
Initial Y velocity	0.294055951059	[m/s]
Initial Z velocity	12.827152878	[m/s]
Simulation time	443683.910349	[s]

Figure 6.6: Jacobi Integral for the regolith launched from the leading edge of a CDE shaped asteroid which eventually re-impacts the surface of the asteroid.

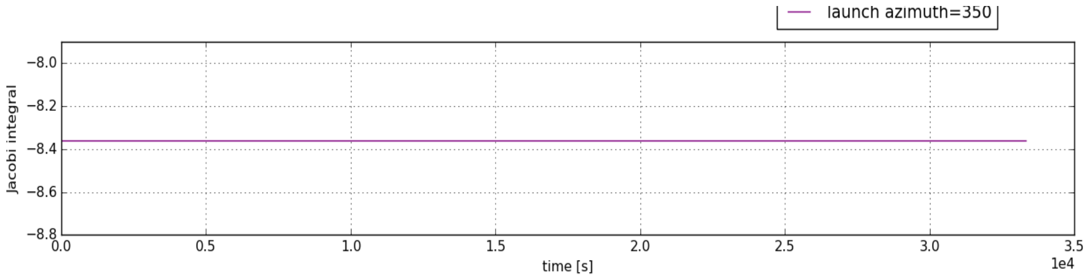

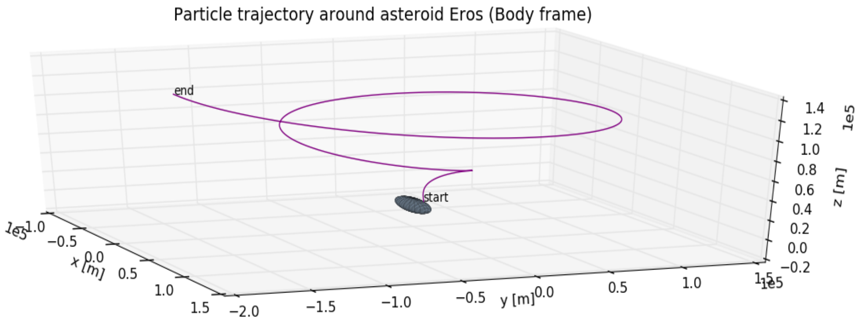

Initial X coordinate	4804.78756138	[m]
Initial Y coordinate	4804.78756138	[m]
Initial Z coordinate	4804.78756138	[m]
Initial X velocity	-5.50162085006	[m/s]
Initial Y velocity	2.15435970563	[m/s]
Initial Z velocity	11.4721135153	[m/s]
Simulation time	33330.0	[s]

Figure 6.7: Jacobi Integral for the regolith launched from the leading edge of a CDE shaped asteroid which eventually escapes the gravitational attraction of the asteroid.

6.3.3 INTEGRATOR PERFORMANCE

The integrator used in our simulator NAOS was from an external library called *boost*. We use this library because coding higher order numerical integrators is an extremely daunting task which would have swayed away time and focus from the thesis at hand. On top of that, the boost library provides verified integrator subroutines (among other things) and hence this reduces our task to just verify that it has been used properly in our simulator. From the results in the previous two subsections, we can say that the integrator has been properly accommodated in NAOS otherwise the behavior of the Jacobi integral and the Keplerian energy would have been different. Here, we will briefly discuss the performance of the integrator under different configurations of itself, for the same particle launch conditions as mentioned in Section 6.3.2. But first we'll give a brief description of the integrators adaptive behavior before we can look at some numbers on the performance.

The integrator used is a Runge-Kutta-Fehlberg78, which is an 8th order integrator with the 7th order used for error control. The integrator uses an adaptive step size, which means that the step size for integration, from one epoch to another, changes continuously depending on the magnitude of integration error at each step. What this means is that the number of steps taken to integrate from an initial epoch to the final one changes, for every instance of integration in a sequence. So to propagate the state vector from, say, time t_0 to t_1, the integrator first performs a single step of integration based on an initial guess for the step-size. This is done first using an order 8 process then again using a 7th order process. The difference in the outcome between the two is then treated as the numerical error for that step. This process of error estimation of-course repeats for every other step of integration performed, to go from time t_0 to t_1. The estimated error is compared with the following equation:

$$abs_{tol} + rel_{tol} \times (X + (dt * dXdt)) \tag{6.1}$$

where abs_{tol} and rel_{tol} are the absolute and relative error tolerances of the integrator, and their values can be set by the user; X is the state vector, dt is the time step for integration, and $dXdt$ is the first order differential equation for the state vector (so basically the equations of motion in our case). Now if the estimated error is smaller than Equation (6.1), the integration step is accepted and the integrator moves on to the next step. If, however, the estimated error is larger, then the step size is reduced and the integration is performed again. There are other processes that run internally within the subroutine, that ensure that the step-size does not become too small or too large, the details of which can be found at (*Boost, "Integrator"*).

Table 6.9 gives values for certain metrics that showcase the variation in performance of the Runge-Kutta-Fehlberg78 integrator. Note that we propagated the trajectory of the regolith for the same initial conditions as mentioned in Section 6.3.2. The metric CPU time refers to the total time taken by the computer processor to integrate the entire problem from start to end. The total CPU time shouldn't be taken at face value but rather at the order of magnitude because background processes in the computer could delay the time taken to perform a given simulation. The entire simulation, from the start till the end, is broken down into a series of smaller integration instances. For each instance then, the number of steps to perform the integration changes since the step-size keeps on changing. Thus, the column *max. step* refers to the maximum number of steps undertaken for any integration instance in the entirety of the simulation. Similarly, the column *min. step* gives the values for the least number of steps. Each row in Table 6.9 corresponds to one entire simulation performed with the given absolute and relative tolerances.

Table 6.9: Variation in integrator performance for different error tolerance values.

Absolute Tolerance	**Relative Tolerance**	**CPU time [s]**	**Max. Steps**	**Min. Steps**
10^{-2}	10^{-2}	0.54	6	3
10^{-6}	10^{-6}	0.47	6	3
10^{-15}	10^{-15}	0.41	6	3
10^{-20}	10^{-20}	2.43	2468	5

It is important to note that the integrity of the simulation from the dynamics point of view was not hampered for any of the combinations of absolute and relative tolerances given in Table 6.9. They all gave the same result as that in Figure 6.5. A logical inference to be drawn from this is that even when the tolerance is relatively large, the simulation results turn out to be the same because the estimated error in integration itself is very small in the first place. We see a visible difference in the performance only when the tolerances are made extremely small, such as 10^{-20}, which ultimately causes the integrator to perform computations at much smaller step-sizes because now the estimated error gets larger in comparison to Equation (6.1). Not shown in Table 6.9, but the tolerances were further reduced to 10^{-30} at which point the simulation got extremely slow and never ceased within a reasonable amount of time. Thus extremely small tolerances, i.e. beyond 10^{-15}, should not used for the purposes of this thesis since we are simulating several thousand particles at the same time. We ultimately decided to use an absolute and relative tolerance of 10^{-15} since it gave the same performance as any other higher tolerance value.

6.4 SOLAR PERTURBATIONS

In this section we will provide results on tests performed to validate the perturbing force models. The test data was taken from, the already verified, unit test files of TUDAT (Technische Universiteit Delft Astrodynamics Toolbox) [3]. We benchmark the force models used in NAOS by performing tests with data from TUDAT and data obtained from some simplified hand-based calculations as well. The subroutines for the force models in NAOS were modular enough and no changes were made to the function codes to accommodate the validation process.

6.4.1 SOLAR THIRD-BODY EFFECT

We'll begin by presenting validation data for the STBE perturbing acceleration. The position vector of the target location where the perturbing acceleration had to be calculated, and the position vector to a random perturbing body, are both mentioned with respect to some common arbitrary frame of reference. The definition of the latter does not matter or affect the computation within the STBE force model. The gravitational parameter of the perturbing body is 4900.0×10^9 m^3/s^2. The computed acceleration values matched those provided in the TUDAT unit test files, shown in Table 6.10, thus validating the STBE force model for a more generalized 3D data.

Table 6.10: Validation data for testing the STBE force model, taken from unit test files in TUDAT. The gravitational parameter of the perturbing body is 4900.0×10^9 m^3/s^2.

Vector	**Component**		
	x	y	z
Target position [m]	-40000000.0	9000000.0	-9500000.0
Perturber position [m]	25000000.0	-380000000.0	-55000000.0
Perturbing acceleration [m/s^2]	2.93946e-06	2.22539e-06	1.16801e-06

The second test was a more simplified one and uses hand-based calculations to verify the software routine. This was done to test if the routine performs correctly even for an edge case. The test considers a planar situation wherein the regolith is on the positive x-axis with respect to the asteroid (consider looking at Figure 4.9 to visualize the set up) and the Sun is in the equatorial plane of the asteroid on the negative x-axis. The position vectors for the two bodies and the corresponding acceleration values, both hand-calculated and software computed, are shown in Table 6.11.

Table 6.11: Validating the STBE force model using hand-calculated acceleration values for a specific edge case.

Vector		**Component**		
		x	y	z
Target position [m]		25000.0	0.0	0.0
Perturber position [m]		-1.0 AU	0.0	0.0
Perturbing acceleration [m/s^2]	Hand-calculated	1.98201e-09	0.0	0.0
	Software computed	1.98201e-09	-3.64089e-25	0.0

There is an extremely small round off error in the y-component of the software computed perturbation acceleration but apart from that the software values match the hand-calculated ones in

[3]TUDAT is an open source astrodynamics toolbox, developed and maintained by the department of astrodynamics and space missions at the Delft University of Technology and the toolbox can be found at `https://github.com/tudat/`.

terms of both magnitude and direction.

6.4.2 SOLAR RADIATION PRESSURE

We'll now present validation data for the SRP force model. The first test assumes a spacecraft near Venus. The parametric data for the test was again taken from the TUDAT unit test files and is shown in Table 6.12. The acceleration due to SRP computed from the software routine matched in direction and magnitude with the test data. The position vector goes from the target to the Sun and is defined with respect to an arbitrary frame. The definition of the frame does not matter for the software routine to calculate the perturbing accelerations, apart from the fact that the values will be defined with respect to the arbitrary frame.

Table 6.12: Validation of SRP model using test data from TUDAT. The test assumes a satellite somewhere near Venus and considers a planar case.

Parameter	Value
Target to Sun position vector [m] (x, y, z)	(77432181578.46405, 77432181578.46405, 0.0)
Target emissivity	0.5
Solar incident area [m^2]	0.005
Target mass [kg]	0.0022
Solar constant	1.0205062450596109e+17
Perturbing acceleration [m/s^2] (x, y, z)	(-2.05148e-05, -2.05148e-05, 0.0)

The second test, again taken from TUDAT, assumes a random location for the target in 3D, thus providing a more generalized test scenario. The incident area and target mass are also extremely exaggerated. The parametric data used for the test and the output acceleration values are shown in Table 6.13.

Table 6.13: Validation of SRP model using test data from TUDAT. The test assumes an exaggerated target body at a random location and considers a general 3D scenario.

Parameter	Value
Target to Sun position vector [m] (x, y, z)	(94359740.25, 90831886.1, 14668782.92)
Target emissivity	0.4058
Solar incident area [m^2]	514701.9505
Target mass [kg]	1.0
Solar constant	1.0205062450596109e+17
Perturbing acceleration [m/s^2] (x, y, z)	(-3.04373e+06, -2.92993e+06, -473166)

The perturbing accelerations computed from the software routine for SRP in NAOS matches the test data from TUDAT, thus validating the software model. Just like for STBE, we present a case of validation against hand-calculated data for a set of very simple parametric values. The results and test data are given in Table 6.14. There is an extremely small round-off error in the x-component of the computed acceleration, but the magnitude and direction matches that of the hand-computed values. Thus with this final test, we can say that the software is verified.

Table 6.14: Validation of SRP model in NAOS for an edge case against hand-calculated data.

<table>
<tr><th colspan="2">Parameter</th><th>Value</th></tr>
<tr><td colspan="2">Target to Sun position vector [m] (x, y, z)</td><td>(0.0, 0.1 AU, 0.0)</td></tr>
<tr><td colspan="2">Target emissivity</td><td>1.0</td></tr>
<tr><td colspan="2">Solar incident area [m^2]</td><td>1.0</td></tr>
<tr><td colspan="2">Target mass [kg]</td><td>1.0</td></tr>
<tr><td colspan="2">Solar constant</td><td>1.0e+17</td></tr>
<tr><td rowspan="2">Perturbing acceleration [m/s^2] (x, y, z)</td><td>Hand-calculated</td><td>(0.0, -0.000893674, 0.0)</td></tr>
<tr><td>Software computed</td><td>(-5.47218e-19,-0.000893674, 0.0)</td></tr>
</table>

6.5 REGOLITH FINAL FATE

Part III

Numerical Simulation Results

7
RESULTS

7.1 REGOLITH LAUNCHED FROM THE LONGEST EDGE OF THE ASTEROID

The results that we'll discuss in this section pertain to the case of regolith launched from the longest edge of the asteroid, modeled as an ellipsoid.

7.1.1 NON-CONSERVATIVE GUARANTEED ESCAPE SPEED

In this section, we will discuss the results from the non-conservative guaranteed escape speed analytical method developed in Section 4.7. As mentioned there, the launch location for testing out the algorithm was chosen to be the longest edge of the ellipsoid shaped asteroid since it helped in simplifying the computation. In addition to this, the particles were launched in the equatorial plane such that the orbital inclination remained zero [1], which further simplified the computation.

We compare the results from our derivation of the non-conservative guaranteed escape speed with that of the conservative approach as defined by Scheeres 2016. To use the algorithm, the following launch conditions were used (these launch conditions are also depicted in Figure 7.1):

1. The launch location is at the longest edge of the ellipsoid.
2. The launch azimuth is equal to 270°.
3. The launch declinations are varied from 10° to 80°.
4. The launch velocity was kept fixed and chosen at random to be 6.0 m/s

Note that these launch conditions result in equatorial orbits, just like how we want to test the non-conservative escape speed algorithm. The value for the parameter q_∞ in Equation (4.115), which is the periapsis distance for a parabolic escape trajectory, was set manually for each simulated trajectory and remained constant during the entire duration of each simulation. Several values of q_∞ were used for testing and they were all taken as fractions of the largest dimension of the ellipsoid. This was done because we do not yet have a dedicated process to determine the value of q_∞ and hence several random fractions were used to guage the output.

[1] The orbital inclination remains zero valued after the launch in a non-uniform gravity field because the central body is homogeneous as well as symmetrical about the equator which means that there is equal attraction in the positive and negative z-axis directions which cancel each other out.

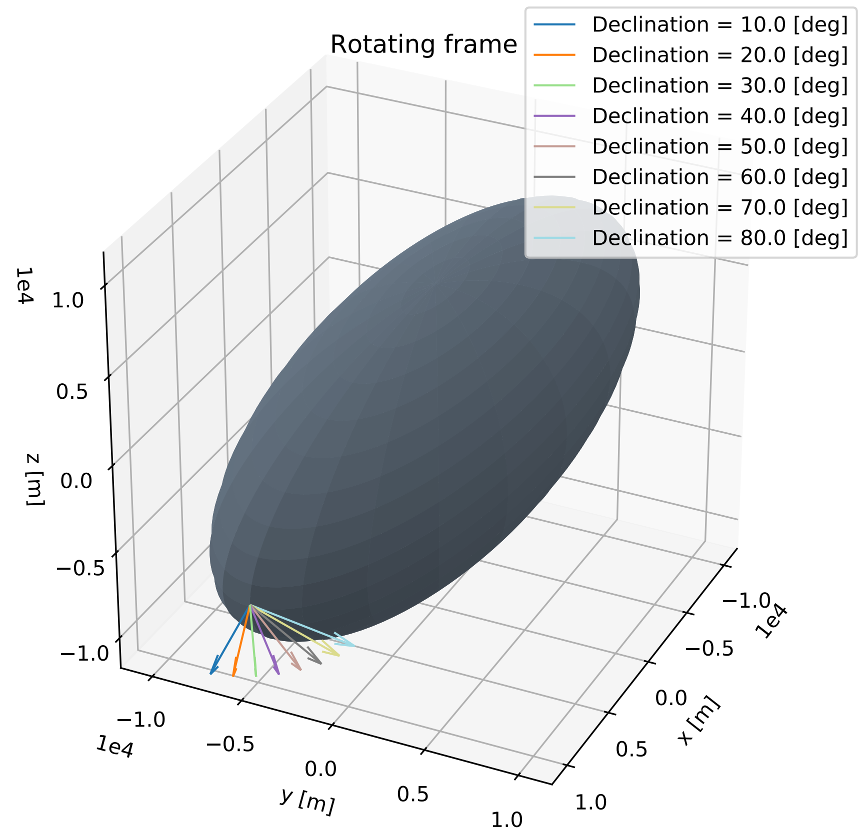

(a)

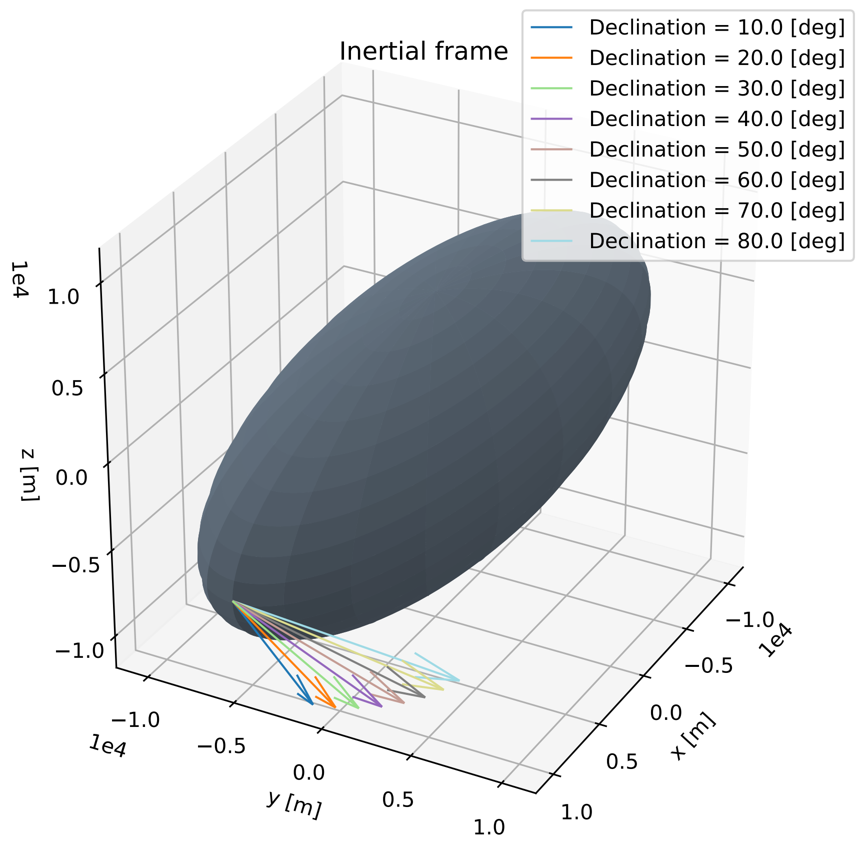

(b)

Figure 7.1: Launch vectors used for testing the non-conservative escape speed algorithm. Figure 7.1a shows the vectors expressed in ARF and Figure 7.1b shows the vectors expressed in AIF.

We will first look at the case of a homogeneous spherical asteroid whose radius is equal to the largest semi-major axis of the CDE i.e. 20 km. The simulation involved launching particles at a constant declination of 45° and for launch azimuth varying in the range [0, 360)°. The launch velocities ranged from 1 - 20 m/s and the simulations did not include perturbations, gravity or otherwise. We used the CDE potential model but all three semi-major axes were made equal to 20 km. In such a case, the CDE gravity potential model acts like a point mass potential model. This situation works for us since the latter is the actual gravity potential model for a point external to a homogeneous spherical body (MacMillan 1958).

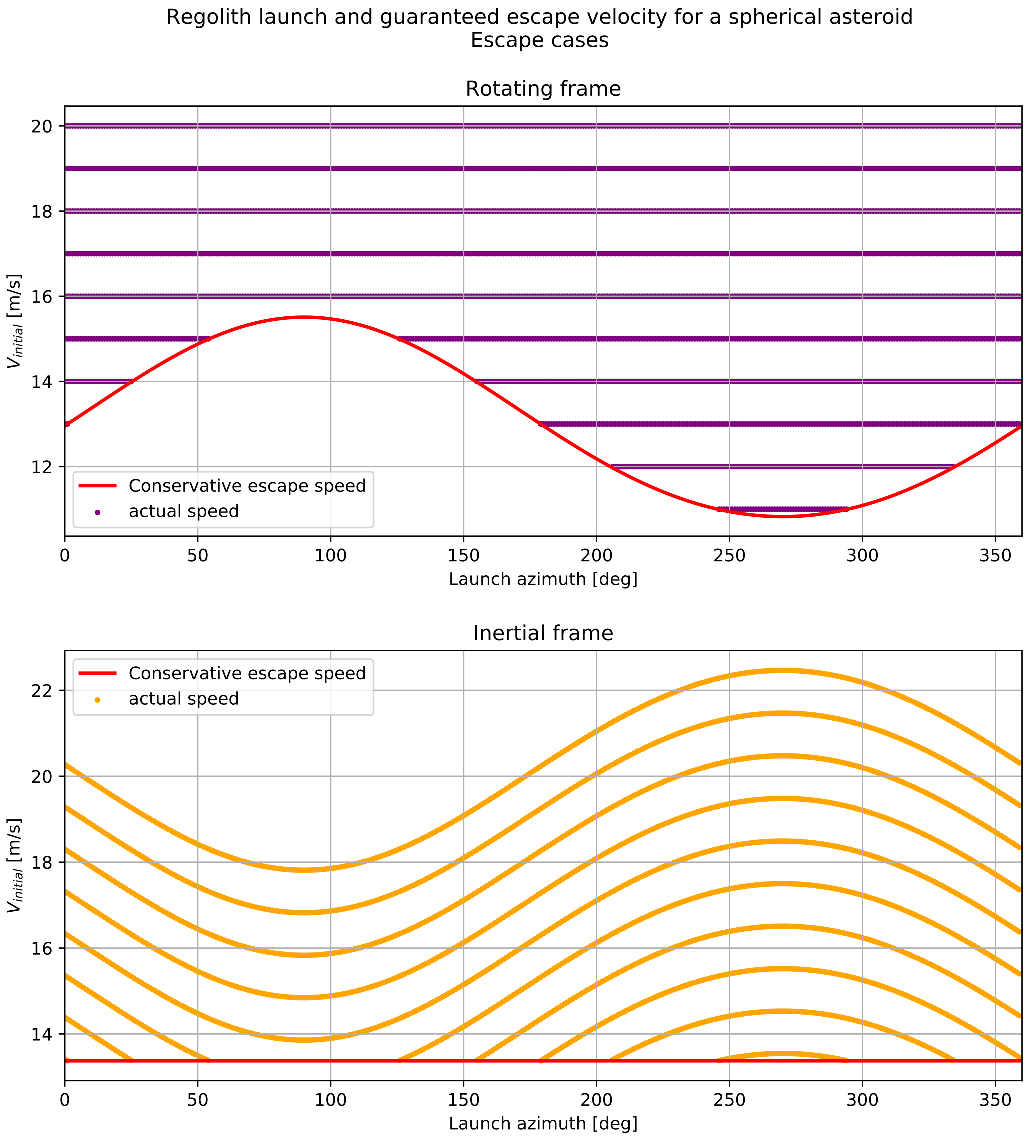

Figure 7.2: Escape velocities for varying launch azimuths and a constant launch declination of 45°. The conservative guaranteed escape speed curve clearly separates all escape scenarios, as shown in both AIF and ARF.

The algorithm for the conservative guaranteed escape speed works properly for the case of a homogeneous spherical asteroid, as shown in Figure 7.2, whose gravity potential is equivalent to that of a point mass. An escape occurs only if the particle was launched with a velocity which is equal to or above the conservative guaranteed escape speed curve and not otherwise. Figure 7.3 shows how the curve even separates out all the re-impact cases. All launch velocities that are below the escape speed curve result only in re-impact and nothing else. Note that for this particular simulation we did not obtain any capture cases, but only escape and re-impact.

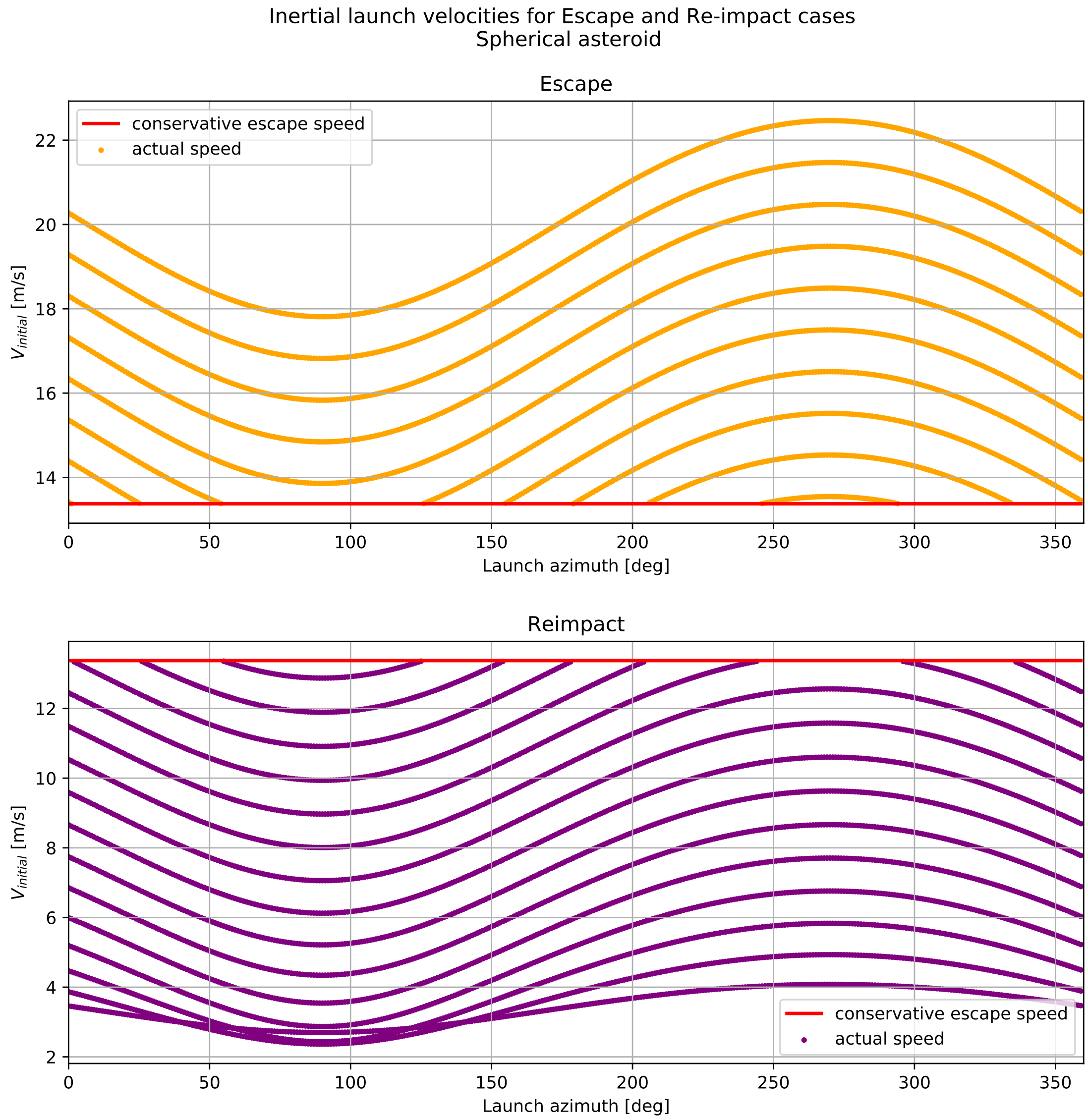

Figure 7.3: Escape and re-impact scenario velocities for varying launch azimuths and a constant launch declination of 45°. The conservative guaranteed escape speed curve clearly separates all re-impact cases from the escape ones.

Now we shall look at the results for a CDE model, for which a particle was launched with the initial conditions enlisted earlier. Figure 7.4 shows the inadequacy of the conservative guaranteed escape speed algorithm to predetermine escape scenarios based just on the initial conditions, as it fails to account for escape situations that occur at lower declination angles. However, for all launch velocities above the conservative escape speed curve, we only witness escape scenarios which is how it should be and any result contrary to this means the simulator is at fault. The non-conservative escape speed algorithm, does not function as expected. The algorithm was designed, hoping that it would also account for escape cases that the conservative approach was unable to. Figure 7.4 shows the non-conservative escape speed curves for three different q_∞ values and although we get an idea on the performance from individual q_∞ values, the algorithm in general fails to identify escape scenarios since there are cases (at higher declination angles) where the launch velocity lies below the q_∞ curves but belongs to the escape regime.

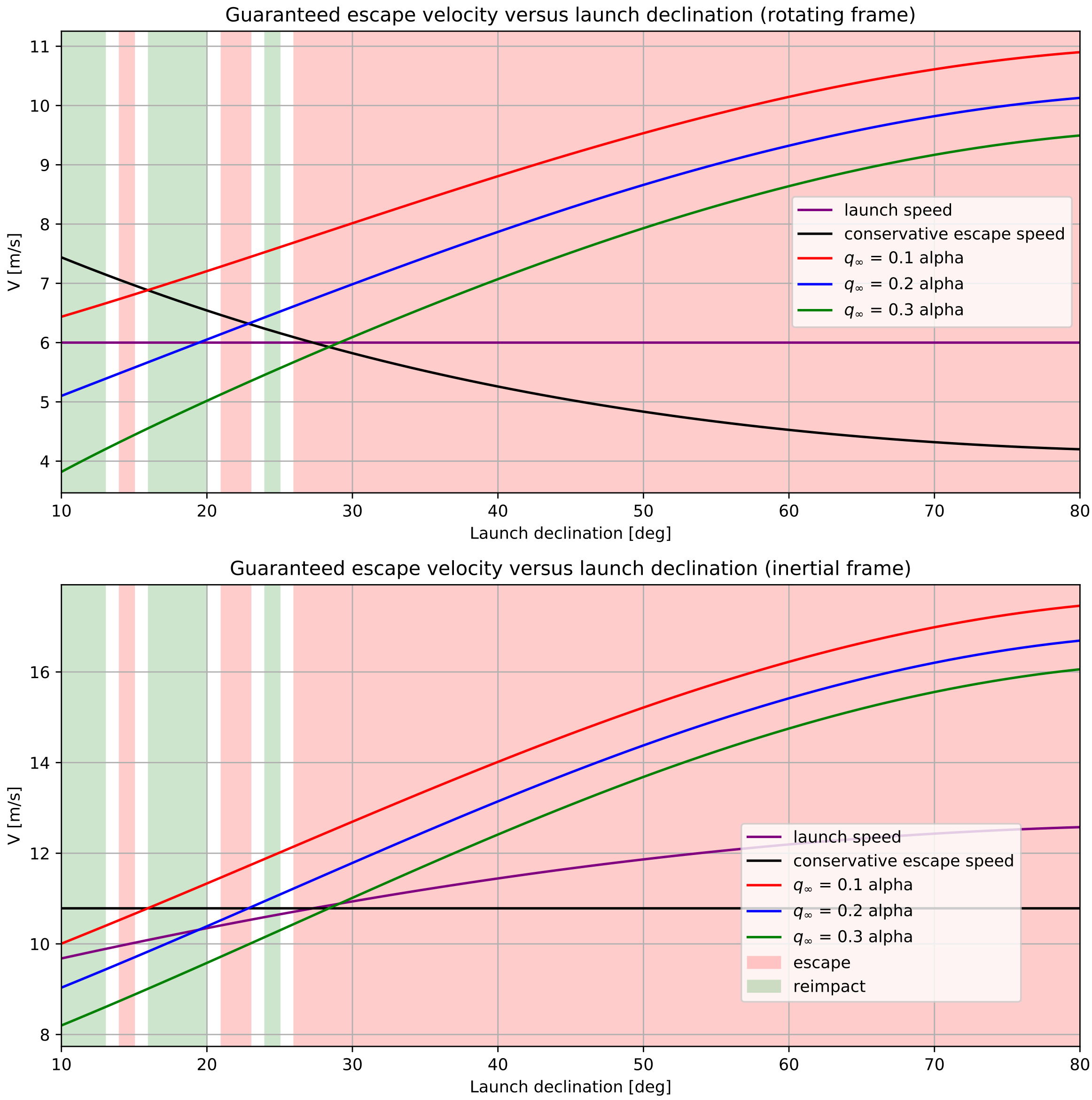

Figure 7.4: Escape and re-impact scenarios depicted for regolith launched with a single velocity and launch azimuth but multiple launch declination values. Non-conservative escape speed curve is shown for a CDE asteroid for three q_∞ values that are fractions of the largest semi-major axes, α, of the ellipsoid. The conservative guaranteed escape speed curve is also shown for comparison.

It is important to note that in Figure 7.4, the non-conservative escape speed curves used only the "+" sign part of the formula in Equation (4.115) and not the "-" sign part since the latter always gave negative velocities for multiple sample values of q_∞. We performed the simulation for the non-conservative approach for the same launch azimuth and range of declination angles as before but velocities ranging from 1 to 16 m/s and $q_\infty = 0.3$ to see if the curve provides better escape estimates at other launch velocities. The result of this is shown in Figure 7.5. We see yet again the failure of the so called non-conservative escape speed algorithm. We witness that even when the launch velocity is above the non-conservative escape speed curve, we have re-impact scenarios. This clearly means that the algorithm is not even able to demarcate re-impact situations. Atleast with the conservative escape speed curve, we know that if the launch velocity is above the curve then the regolith can only escape and not have any other final fate.

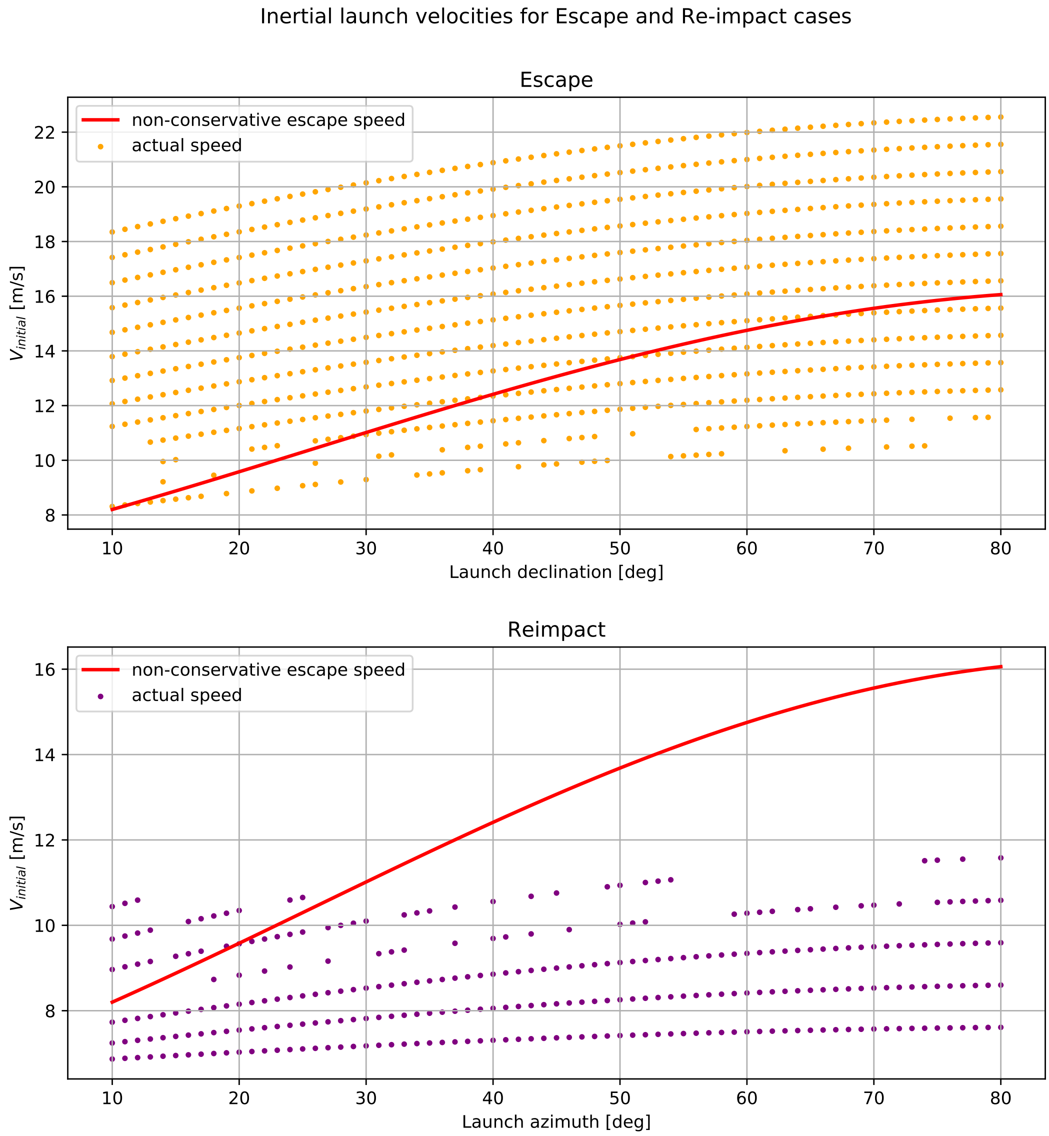

Figure 7.5: Escape and re-impact scenarios depicted for regolith launched from the longest edge of CDE with multiple velocities with launch azimuth = 270° and launch declination in the range of 10 to 80°. The non-conservative escape speed curve is shown for $q_{\infty} = 0.3$.

On the other end of the spectrum, we can see that there are launch velocities below the non-conservative escape speed curve where escape scenarios occur. This is another indication of the failure of the algorithm we designed.

The other problem with the algorithm is that if we reduce the value of q_{∞} beyond certain extent, then we obtain a gibberish curve for the non-conservative escape speed in the ARF. An example of this is depicted in Figure 7.6 where $q_{\infty} = 0.7$. The curve as expressed in the ARF has no meaning since negative speeds are not valid.

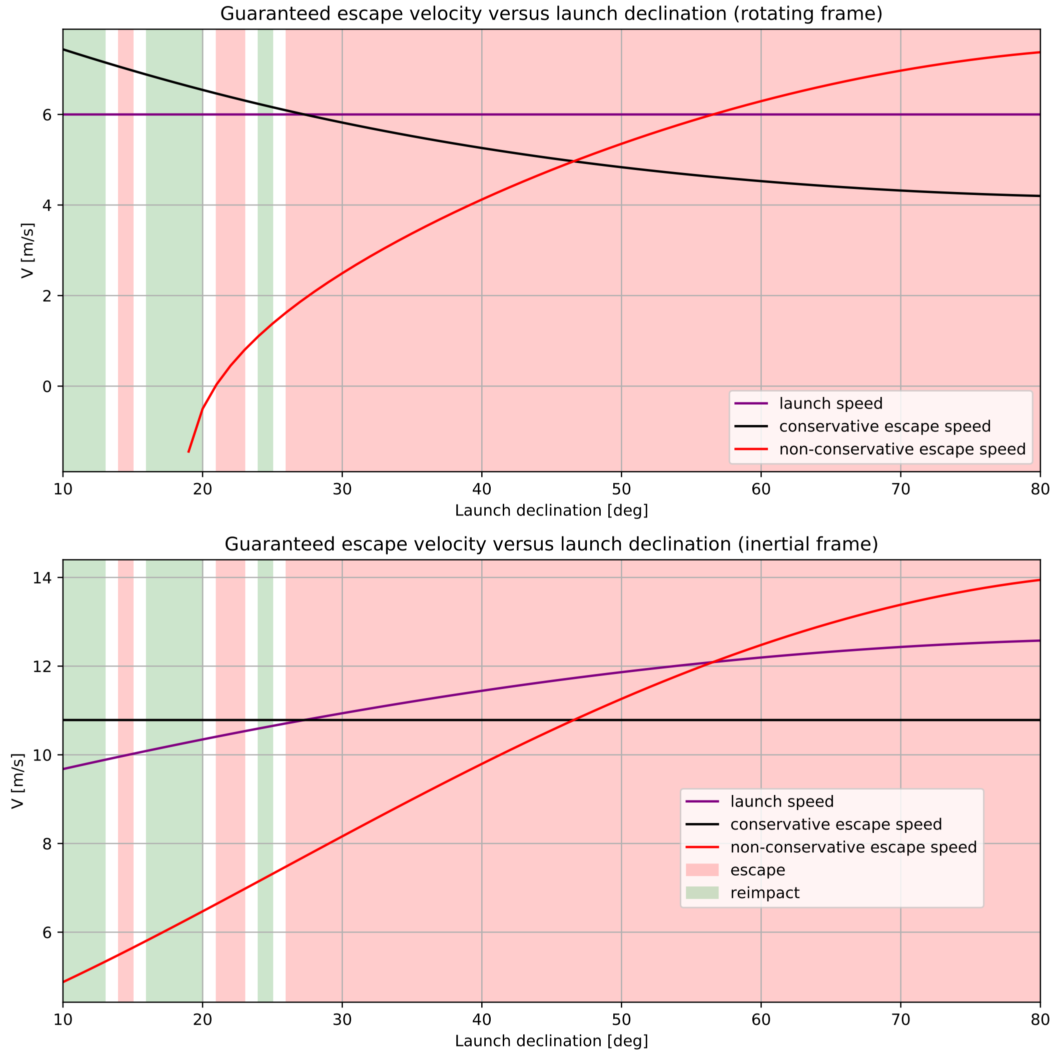

Figure 7.6: A non-applicable non-conservative escape speed curve for $q_\infty = 0.7$. The curve in the rotating frame or the ARF shows negative speed values which is not valid.

The non-conservative guaranteed escape speed method did not work as expected in identifying the escape cases that were undetected by the conservative method. In addition to this, we saw that the method produces a valid escape velocity curve only for a small range of q_∞ values. Although the non-conservative method failed, the approach to derive it was correct and now we know that even if it sounds reasonable in theory, it fails completely in practice.

The conservative escape speed approach didn't account for a few escape scenarios when regolith was launched from the surface of a CDE shaped asteroid and the reason for that is the combined effect of the shape/gravity field variations and a rapid rotation rate of the asteroid. For example, from the trajectory for the regolith launched at declination angle of 15° in Figure 7.4, it was observed that the particle completes one revolution around the asteroid before embarking on a final hyperbolic trajectory. This is shown in Figure 7.7.

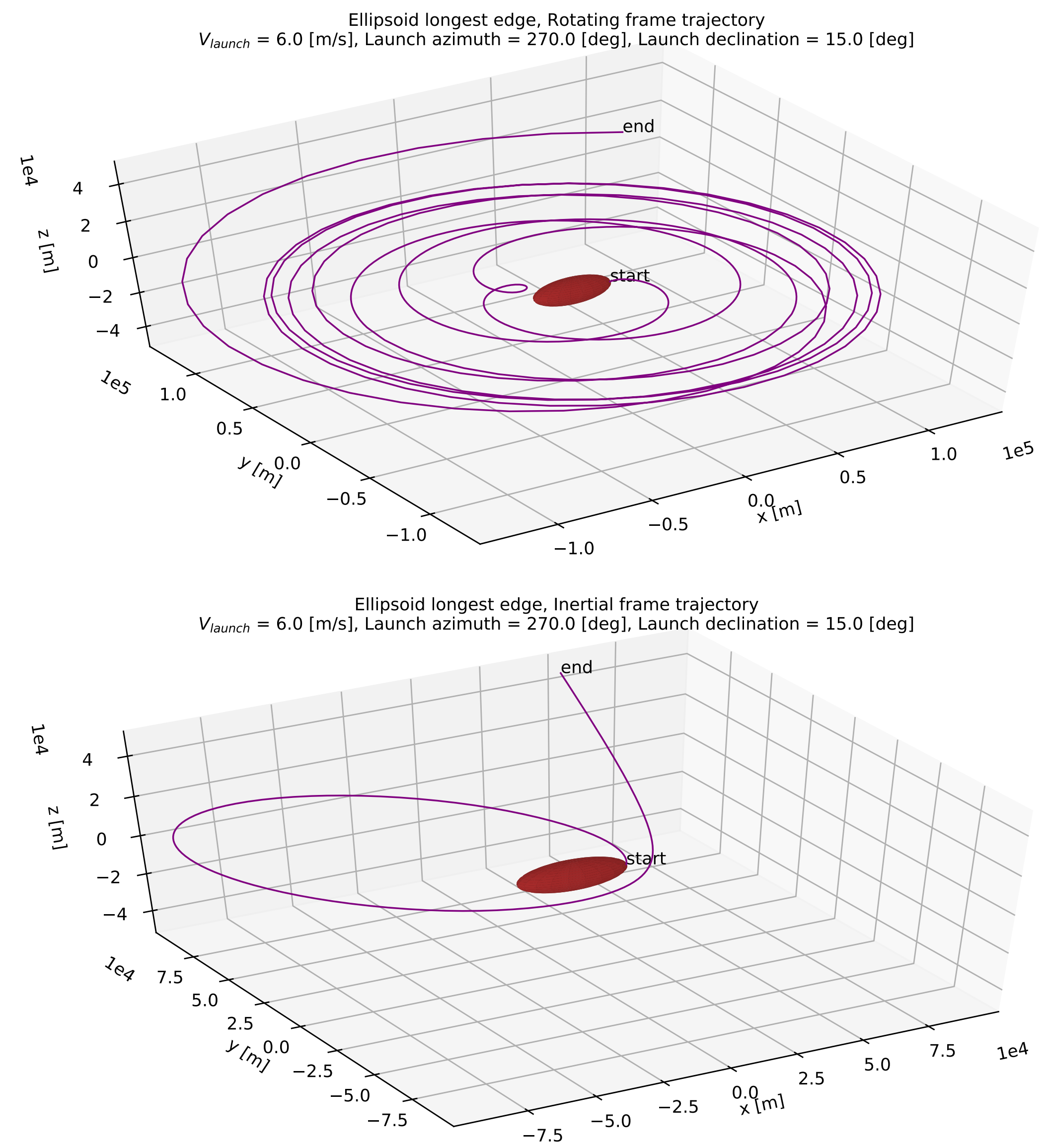

Figure 7.7: 3D trajectory in the ARF and the AIF for launch declination angle 15° from Figure 7.4.

The animation for the trajectory in Figure 7.7 can be found at the web-link given in Figure 7.8. The animation clearly shows the rapid rotation rate of the asteroid which accelerates the particle as it approaches behind it and completes the one and only revolution around the asteroid; having its velocity increased enough to eventually attain a positive energy and escape the asteroid. Thus with the help of gravity perturbations and a fast rotating asteroid, the particle changes from an elliptical orbit to a hyperbolic trajectory leading to its escape. This behavior can not be easily captured just from the initial conditions, as we observed, by the conservative guaranteed escape speed algorithm.

An important thing to note here is that the initial condition of the regolith was such that its osculating eccentricity was above 1.0 (but a negative total energy), meaning that at the moment of the launch the regolith was on a hyperbolic trajectory but instantly evolves its orbit into an elliptical one. The reason for this is again the perturbations from a non-uniform gravity field and a rapidly rotating asteroid which keeps osculating the orbit. On the other hand, when we consider a spherical asteroid, the launched particle continues to propagate on the initial trajectory itself because in the absence of perturbations the initial orbital elements do not osculate. Thus for a spherical asteroid, a particle can only escape if the initial orbital elements are such that it is on a parabolic or a hyperbolic trajectory and not otherwise due to a lack of external influences to osculate the orbit. This is why the conservative guaranteed escape speed algorithm works for the spherical asteroid in predetermination of escape situations.

Figure 7.8: Scan the QR code to view the 2D trajectory animation in the AIF for launch declination angle 15° from Figure 7.4. The video can also be accessed from the following web-link: `https://youtu.be/5l_CAYnjotk`.

The final aspect that will be discussed in regard to the conservative guaranteed escape speed algorithm is its capacity to distinguish between particles that escape immediately and the ones that take one or more revolutions before escaping, when launched from an irregular body (Scheeres et al. 2002). However, we found out that this is only true if the particle is launched from the surface in the normal direction. In that, if the launch speed is lower than the conservative guaranteed escape speed and the particle escapes, then it underwent multiple revolutions. This was observed for multiple particles launched from the longest edge of the CDE for launch velocities ranging from 1 to 16 m/s. However, this phenomenon is not observed when the launch direction is not in the normal direction. For example, from Figure 7.4, the launch declination angle of 26° results in a direct escape scenario, even though the launch velocity is below the conservative guaranteed escape speed algorithm. The 3D trajectory for this case is shown in Figure 7.9.

Thus, it is imperative to understand that with just a non-uniform gravity field and a relatively fast rotating asteroid, the dynamics for orbiting regolith become intangible enough such that predetermination of orbital behavior and final fate of the regolith can not be explained by simple analytical methods. We attempted to explain the complex behavior by deriving a different guaranteed escape speed algorithm, however, the method failed completely. We realize now that a numerical simulation method is a relatively better approach to understand the orbital dynamics of regolith lofted from an asteroid.

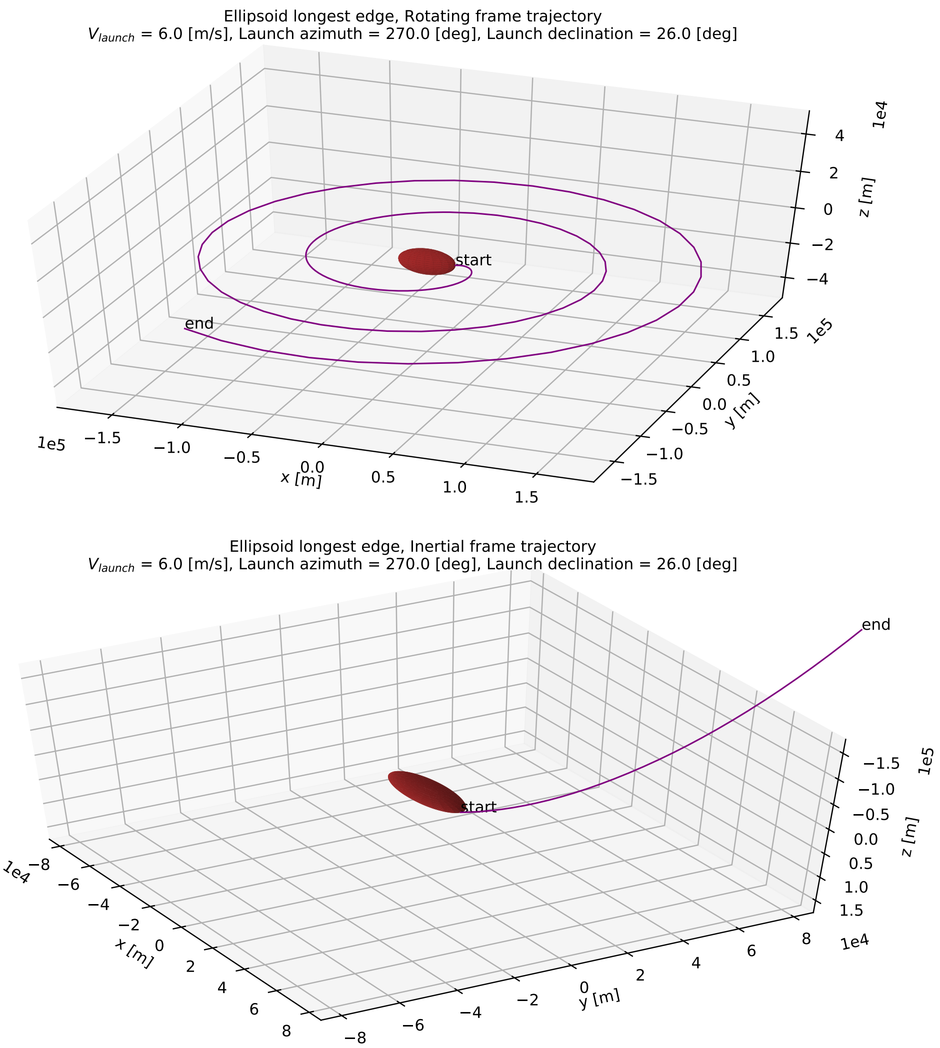

Figure 7.9: 3D trajectory expressed in the ARF and the AIF for a launch declination angle of 26° from the normal direction. The particle launch conditions are the same as that used for Figure 7.4.

7.1.2 DYNAMICS WITHOUT SOLAR PERTURBATIONS

7.1.3 DYNAMICS WITH SOLAR PERTURBATIONS

In this case, the simulation accounted for perturbations from the irregular gravity field of the asteroid, the SRP, and the STBE. Within this category, there are 4 distinct sets of simulations, each for a particle with different Area-to-Mass ratio. These are mentioned in Table 7.1. The material with a density of 3.2 [g/cm^3] is low-density Olivine (Magnesium Iron Silicates) and the one with 7.5 [g/cm^3] is Iron-Nickel alloy (Garcia-Yarnoz et al. 2014). We have chosen these two types of materials based on the surface composition analysis of asteroid Eros, an S-Type asteroid, from the NEAR-Shoemaker data. S-Type asteroids, from reflectance spectral analysis, are commonly known to have minerals like Olivine, Pyroxene, and Fe-Ni (Iron-Nickel) metal (Nittler et al. 2001). Thermo-spectral analysis of regolith on Eros reveals that it is rich in Olivine and is found to be more abundant than Pyroxene (McCoy et al. 2001). The mineral Olivine has also been discovered on Itokawa, another S-Type asteroid, through transmission electron microscope analysis of samples returned by the Hayabusa spacecraft (Keller et al. 2014). Eros also contains Fe-Ni but it is significantly separated from the Silicates (Olivine and Pyroxene) within the regolith (Nittler et al. 2001). Evans et al. 2001 analyzed elemental composition of NEAR-Shoemaker's landing site on Eros, based on which, it presents several arguments for relatively lower abundance of Fe (Iron) on the surface of Eros. One of the arguments hypothesizes that different grain sizes and density of Fe-Ni from Olivine could have resulted in the metal to get separated from the Silicates, either spatially or for it to sink down in the lower depths of the regolith. In light of this, we are considering regolith comprising of only Olivine and Fe-Ni, to distinguish between their orbital behavior and final fate upon being lofted from the surface of Eros. Veverka et al. 2001a analyzed high resolution surface images of Eros captured by NEAR-Shoemaker on a low-altitude flyover. It argued the build-up of a heterogeneous and complex regolith that comprised of material ranging from fine particles all the way up to metre-sized ejecta blocks. Veverka et al. 2001a argues that while there is an abundance of large ejecta blocks across the surface, the much finer regolith occupies mostly the low-lying topographies, i.e., inside large craters on the surface of Eros. The latter was termed as ponded deposits. Robinson et al. 2001 argues, from high resolution images (1.2 [cm] per pixel) of ponded deposits at Eros, that the grain size of regolith would be around 1.0 [cm] or below. Thus based on this extreme spectra of regolith composition at Eros, we shall also consider regoliths with varying densities and grain radii (each grain is assumed to be spherical). These are listed in Table 7.1. The particles are listed in decreasing order of area-to-mass ratio. We considered coarse regolith of 10 [cm] radius as well, the motivation for which comes from the size of the ejecta blocks generated from the impact of NEAR-Shoemaker on Eros's surface. Robinson et al. 2001 notes that their are several 10 [cm] ejecta blocks around the NEAR-Shoemaker impact site. Thus, ejecta size of 10 [cm] in radii is justified for this study in the context of an asteroid exploration or exploitation mission.

Table 7.1: Particle Area-to-Mass ratios

Code	Particle radius [cm]	Density [g/cm^3]	Area-to-Mass ratio [m^2/kg]
LoGSP-1	1.0	3.2	0.0234
LoGSP-2	1.0	7.5	0.01
LoGSP-3	5.0	3.2	0.0047
LoGSP-4	5.0	7.5	0.002
LoGSP-5	10.0	3.2	0.0023
LoGSP-6	10.0	7.5	0.001

The initial conditions for lofting each type of regolith are varied in the same manner and are mentioned as follows. The asteroid revolves around the Sun in an equatorial circular orbit at a distance of 1.0 AU (Astronomical Unit). Four different initial Solar phase angles were considered for the simulation – 45.0, 135.0, 225.0 315.0 [deg], to account for the four different quadrants where the Sun could be with respect to the asteroid. For each case in Table 7.1, a total of 72 particles were launched from the surface of the asteroid, each in a different direction (defined using the launch declination and azimuth angles). The launch declination angle, measured from the zenith, was kept constant at 45.0 [deg] for all the particles. The launch azimuth, measured CCW (Counter-Clockwise) from the direction pointing to north, was varied at a resolution of 5.0 [deg] starting from 0.0 [deg] all the way up to 355.0 [deg]. Each particle was launched, in their specified direction, with different velocities ranging from 1.0 [m/s] to 16.0 [m/s] (measured with respect to the asteroid-centric rotating frame) at a resolution of 1.0 [m/s]. So basically, every combination of an initial Solar phase angle, initial launch azimuth, and initial launch velocity corresponds to a unique trajectory for a single particle of a given Area-to-Mass ratio; Thus amounting to a total of 4608 unique trajectories for each regolith type.

The simulations were subjected to run for a maximum of 270.0 [days] and were terminated earlier if a particular trajectory resulted in escape or surface re-impact. This number was obtained by looking at the close-proximity operational time periods of exploration missions to small bodies of our solar system. We wanted a maximum simulation time in the context of a man-made mission and hence this approach was taken. We accounted for four missions, two from the past and two planned for the future, which have direct contact with a small body as part of their mission and continued the mission around the small body afterwards (hence, not just disposal and/or fly-by). These are the Philae (Rosetta), Hayabusa, Hayabusa-2, and the OSIRIS-REx mission. The close-proximity design operation time period for Philae lander was 3 months (Biele et al. 2008), 3 months for Hayabusa (Kawaguchi et al. 2003), 18 months for the Hayabusa-2 mission (Tsuda et al. 2013), and finally 12 months for the OSIRIS-REx mission (Lauretta et al. 2012). The average of all of this comes out to be 9.0 months, which is what we have considered to be the maximum simulation time. In this regard, we are also categorizing orbital behavior that does not result in escape or re-impact in those 270 days, as capture orbits.

We now present a detailed analysis for one of the regolith types, particle LoGSP-1, because Olivine is the most abundant of the regolith types found on Eros and among the different grain sizes for Olivine, LoGSP-1 offers the maximum area-to-mass ratio. A larger value for area-to-mass ratio means a relatively larger effect of SRP on the regolith which makes it more interesting since for a detailed analysis we want to see how SRP (as well as STBE in general) affects the orbital motion of regolith.

CASE LOGSP-1

Figure 7.10 gives a distribution of particles (henceforth the term particle and regolith shall be used interchangeably without any implication in change of its meaning) for each of the three different final fates for the regolith i.e. capture, re-impact, and escape, for different initial launch velocities and initial Solar phase angles. Irrespective of the initial Solar phase, initial launch velocities from 1.0 to 3.0 [m/s] results in particles launched in all directions to eventually re-impact the asteroid's surface. Similarly, for initial launch velocities ranging from 14.0 to 16.0 [m/s], we see that the particles always manage to escape the gravitational attraction of the asteroid. However, there is one exception to the former statement, a single particle launched with a velocity of 14.0 [m/s] at a launch azimuth of 90.0 [deg] and at an initial Solar phase angle of 315.0 [deg], re-impacts the asteroid's surface. It is interesting to note that the launch azimuth of the particle is such that it is launched in a direction that is directly opposite to the direction of rotation of the asteroid. Launch velocities from 4.0 to 13.0 [m/s] show a mixed behavior and the final fate distribution trend does not vary drastically for different initial Solar phase angles.

The number of capture cases is far less than those for escape and re-impact. For initial Solar phase of 225.0 [deg], there are no cases of regolith being captured in orbit around the asteroid. All capture cases, arranged in order of increasing launch azimuth angle, are listed in Table 7.2. It is interesting to note that all capture cases result from when the particle is launched in a direction which is against the direction of rotation of the asteroid, bar one exception which is case index-11 in Table 7.2. The capture cases which represent symmetry in terms of the launch azimuth angle are highlighted with the same color in Table 7.2. This symmetric behavior results from the combination of two factors. First, the Sun's motion relative to the asteroid is not in an inclined plane, and secondly, the particles are launched from the equatorial tip of the ellipsoid shaped asteroid, which is a point of symmetry on the ellipsoid. The capture cases will be discussed in detail a bit further ahead.

Table 7.2: Initial conditions that resulted in temporary orbital capture of regolith around the asteroid. Particle code LoGSP-1.

Index	Launch azimuth [deg]	Launch velocity [m/s]	Initial Solar phase angle [deg]
1	5.0	5.0	315.0
2	10.0	9.0	135.0
3	15.0	8.0	45.0
4	45.0	12.0	45.0
5	45.0	10.0	315.0
6	135.0	12.0	45.0
7	135.0	10.0	315.0
8	165.0	8.0	45.0
9	170.0	9.0	135.0
10	175.0	5.0	315.0
11	185.0	5.0	135.0

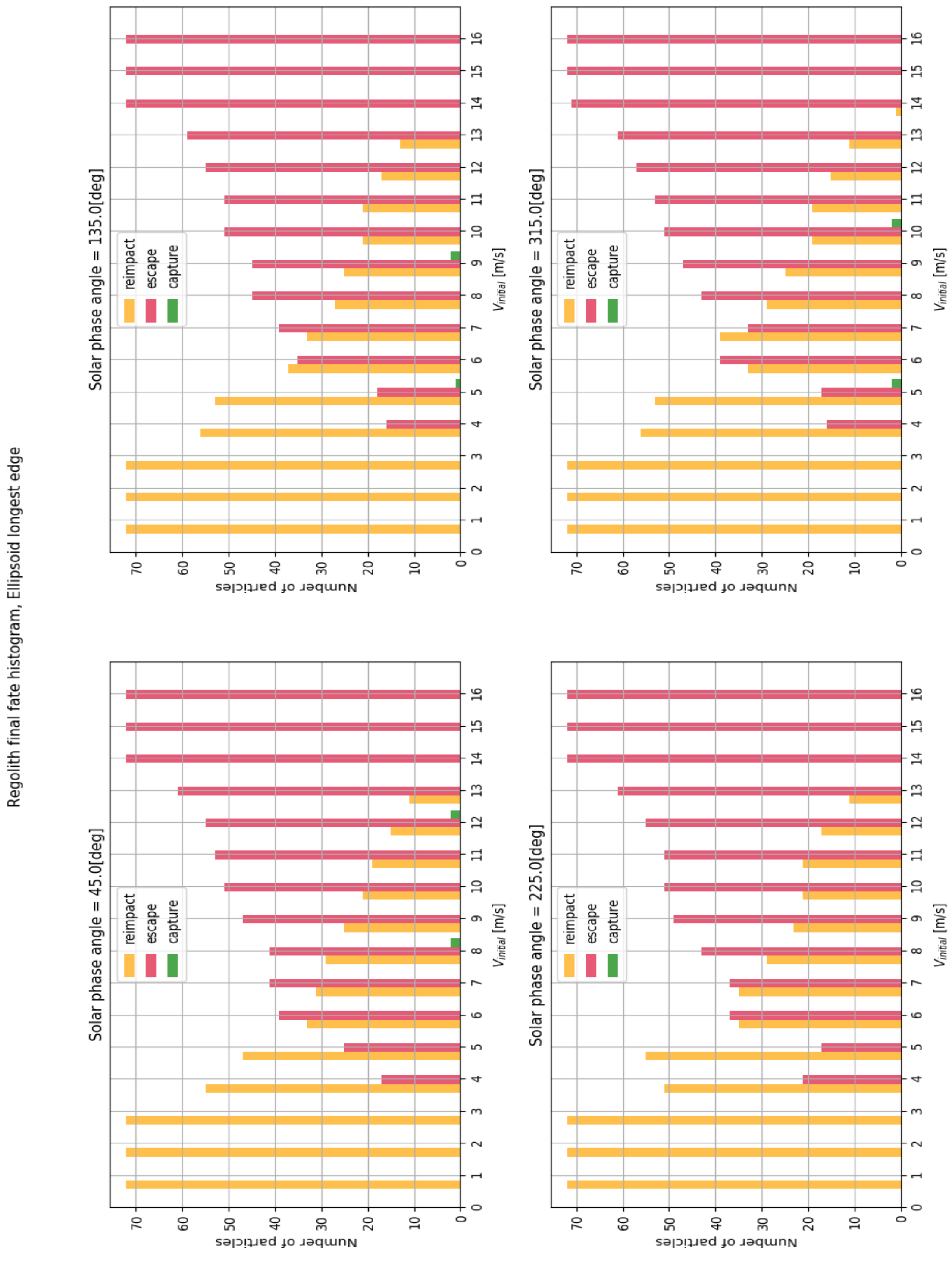

Figure 7.10: Histogram showing the number of particles that re-impact, escape, or get captured around the asteroid, for different initial launch velocities. Particle code LoGSP-1.

Figure 7.11 depicts the surface distribution of regolith that re-impacts the surface when launched from the same location with different velocities and different initial Solar phase angles. The launch location is in the centre of the map, Latitude 0.0 [deg] and Longitude 0.0 [deg]. The particle distribution is the same for regions close to the launch point and for lower launch velocities up until 8.0 [m/s]. A similarity in distribution pattern is also observed around Longitude -150.0 [deg] for launch velocity of 9.0 [m/s] and around Longitude 150.0 [deg] for launch velocity of 10.0 [m/s] for the four Solar phase angles. The distribution pattern, for all launch velocities and initial Solar phases, is also symmetric about the equator. Again, the reason for this is the same as mentioned earlier for the symmetry in capture cases in Table 7.2. Keeping the launch direction and velocity constant, we see that the distribution of regolith that re-impacts the surface does not change drastically with varying initial Solar phase angles, except for a relatively few cases. This is much easily observed in a plot of Range from the launch direction to the re-impact point versus launch azimuth for different velocities as shown in Figure 7.12.

We haven't shown the range to re-impact point plots in Figure 7.12 for all launch velocities because the intention here is to show the qualitative behavior, which can be achieved by considering only a subset of the launch velocities that result in a re-impact scenario. The very first thing we observe is that as the launch velocity increases, the range of launch azimuth over which the regolith re-impacts the surface reduces because a higher velocity allows the regolith to enter a higher orbit (as it attains a relatively higher energy) and reduces the probability of a re-impact. Even as the velocity increases, we see that the azimuths that result in a re-impact are the ones in which the regolith is launched in a direction that is opposite to the asteroid's rotation direction. This makes sense since the regolith's energy would be reduced the most in this scenario compared to all other launch directions, thereby increasing the chances of a re-impact.

Now the primary purpose of the plots in Figure 7.12 (combined with Figure 7.11) is to depict the qualitative effect of Solar perturbations, for varying initial Solar phase angles, on the re-impact behavior of regolith compared to the case when no Solar perturbations are considered. For launch velocities of 4.0, 7.0 and 10.0 [m/s], we see that the Solar perturbations do not affect the re-impact location for cases when the particle is launched in directions opposite to that of the asteroid's rotation. However, we do see few exceptions to the former statement, most noticeably in the case of 7.0 [m/s]. But for the majority of cases where the re-impact location remains unchanged, we see from Figure 7.13, that these particles spend less than 3.0 [Hrs] in orbit which is not enough time for the Solar perturbations to act and have any significant impact on the dynamics of the particles. So in essence this is what's happening here - Particles when launched in a direction that is opposite to that of the asteroid's rotation, even at relatively high velocities such as 10.0 [m/s], loose enough energy to stay in a relatively lower orbit (see Figure A.1) where the gravitational force of the asteroid is significantly stronger than any of the Solar perturbations and as the particle spends a very short time in orbit before re-impact, the Solar perturbations do not get enough time to affect the particle's orbit and hence the particle re-impacts the same location as it would have when no Solar perturbations were considered in the simulation. For the lower launch velocities of 4.0 and 7.0 [m/s], the differences in re-impact locations are more pronounced when the regolith is launched in the same direction as that of the asteroid's rotation. Particles gain relatively higher energy in this case, enter a higher orbit and spend enough time in there for the Solar perturbations to affect it's motion. For the case of the launch velocity of 13.0 [m/s] in Figure 7.12, the velocity is high enough such that the particle does not loose enough energy when launched opposite to the asteroid's rotational direction and is able to enter a relatively higher orbit (see Figure A.1) and stay there for a relatively longer time, as seen in Figure 7.13, which results in the Solar perturbations affecting the orbital motion and eventually the re-impact location of the regolith.

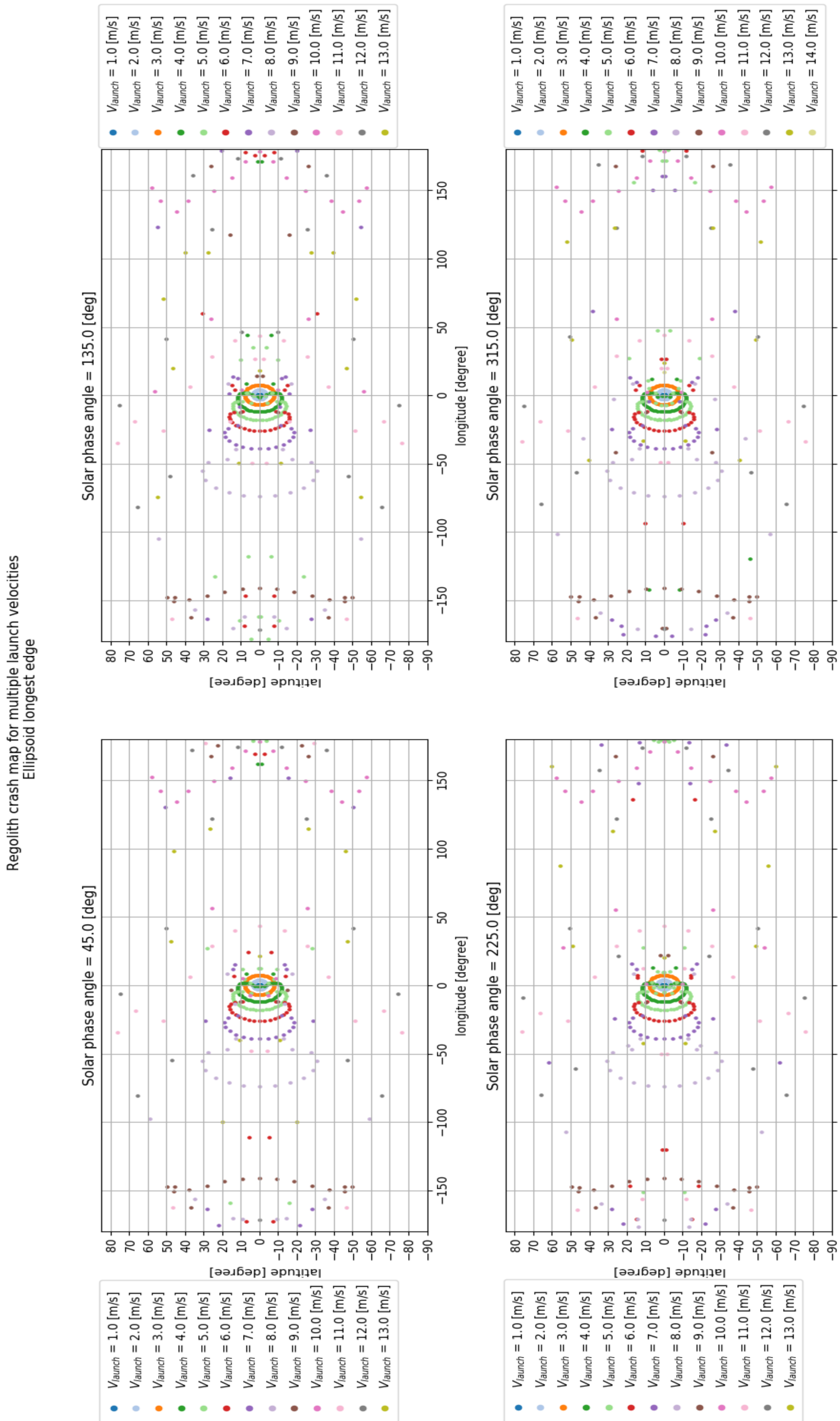

Figure 7.11: Surface distribution of re-impacted regolith for different launch velocities. The launch location is latitude: 0.0 [deg], longitude: 0.0 [deg]. Particle code LoGSP-1.

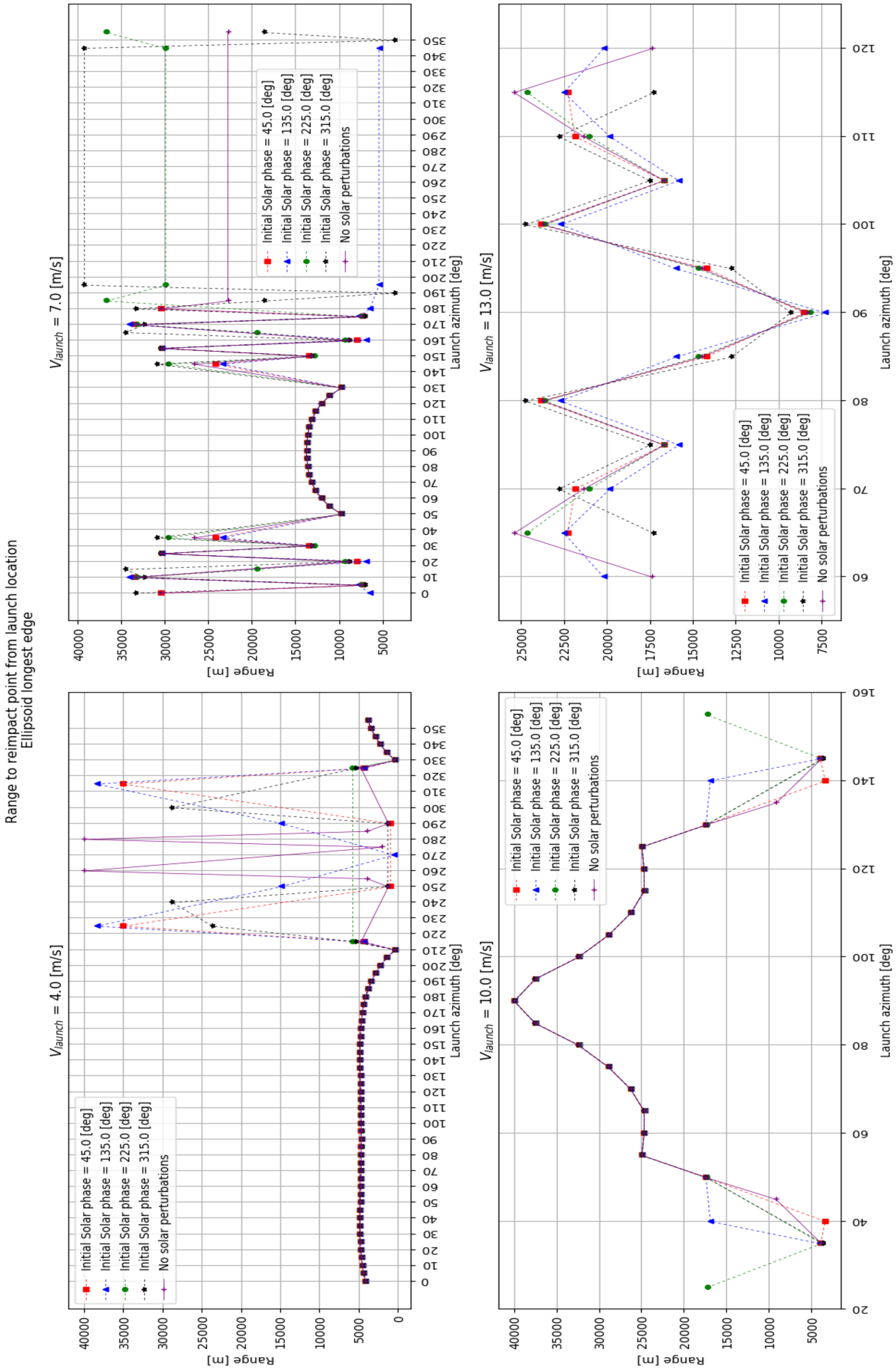

Figure 7.12: Range to re-impact location from the launch point for different velocities. Particle code LoGSP-1.

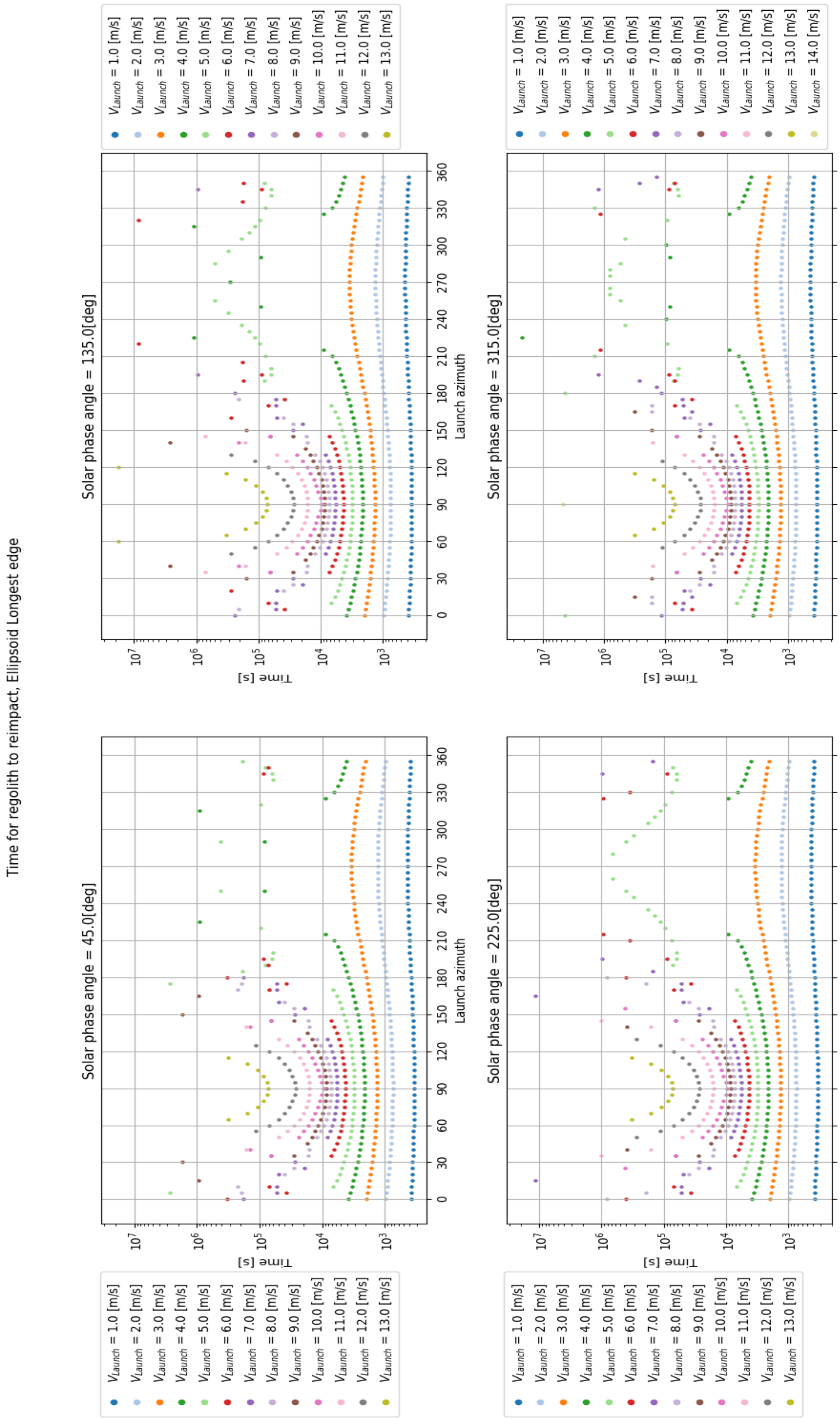

Figure 7.13: Time taken by regolith at different velocities and launch directions to re-impact with the surface of the asteroid. Particle code LoGSP-1.

We shall now look at the cases where the lofted regolith gets (temporarily) captured in orbit by the asteroid. The initial conditions for all capture cases, for the current particle size and density, were mentioned earlier in Table 7.2. Figure 7.15 depicts the progression in orbital range of the temporarily captured regolith. The straight lines in the plot are used to mark the different altitude regimes. These are the LAO (Low Altitude Orbit), MAO (Medium Altitude Orbit), HAO (High Altitude Orbit), UHAO (Ultra-High Altitude Orbit), and EHAO (Extremely-High Altitude Orbit). These altitude regime definitions are not from well defined standards, but instead were arbitrarily chosen as integer multiples of the longest semi-major axis, α, of the tri-axial ellipsoid shaped asteroid. The definition for these altitude regimes is given in Table 7.3.

Table 7.3: Altitude regimes and their definitions

Altitude regime	**Definition**
LAO	Asteroid surface to $2 \times \alpha$
MAO	$2 \times \alpha$ to $3 \times \alpha$
HAO	$3 \times \alpha$ to $5 \times \alpha$
UHAO	$5 \times \alpha$ to $7 \times \alpha$
EHAO	Above $7 \times \alpha$

The purpose of plotting data as shown in Figure 7.15 was to look for any patterns or periodicity, if they existed, and to see if particles in temporary capture scenario remain closer to the asteroid or further away from it. The symmetry as explained for initial conditions mentioned in Table 7.2 can also be seen in Figure 7.15, for example, regolith launched with velocity of 8.0 [m/s] and launch azimuth of 15.0 [deg] (shown by the purple curve in the top plot in Figure 7.15) shows the same behavior as that of regolith launched with the same velocity and 165.0 [deg] launch azimuth (shown by the green curve in the bottom plot in Figure 7.15). Another thing we see from the plot is that, apart from case number 11 in Table 7.2, the captured regolith stay in the higher altitude regions for most part and only briefly do they fall within the MAO and LAO region. We shall now look at atleast three cases from Figure 7.15 in a bit more detail to understand the effect of Solar perturbations by comparing these cases with their counterparts from the simulation where Solar perturbations were omitted.

Of all the cases shown in Figure 7.15 or Table 7.2, the one with a launch velocity of 10.0 [m/s] and launch azimuth of 45.0 [deg] results in a re-impact scenario when Solar perturbations are omitted but the same initial conditions lead to a temporary capture orbit when perturbations were added for an initial Solar phase angle of 315.0 [deg]. Every other initial condition for the capture cases had otherwise resulted in an escape situation when simulations were conducted without the Solar perturbations. The 3D trajectory plot in two different views for the former case are shown in Figure 7.16 (see Figure A.2 also for the 3D trajectory representation in body fixed frame). The 2D trajectory for the same is shown in Figure 7.17 in inertial frame and in Figure A.3 in the asteroid centric rotating frame or the body frame. The web-link or URL for the trajectory animation of the particle (in inertial frame and in XY plane only) can be found in Figure 7.14.

Figure 7.14: 2D trajectory animation (XY Plane) of capture regolith for case number 5 in Table 7.2. Particle code LoGSP-1. Scan the QR code to view the animation or use the following web-link: `https://youtu.be/oZDhDo5CIsk`

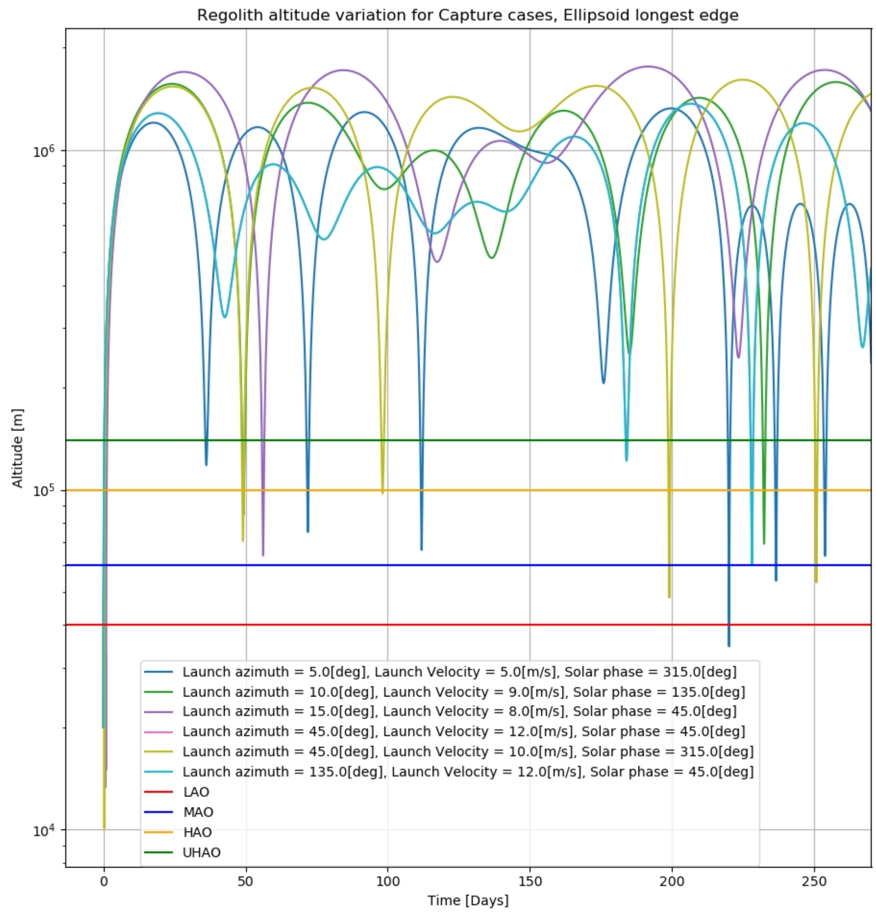

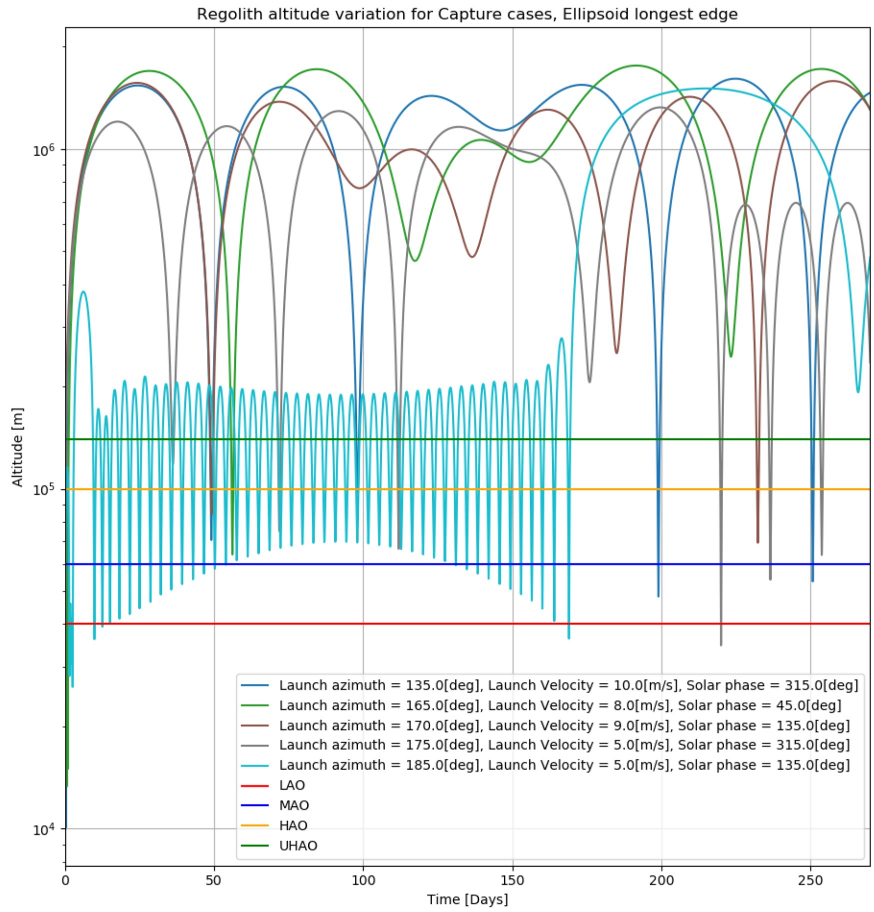

Figure 7.15: Orbital range progression with time for temporary capture scenarios. Particle code LoGSP-1.

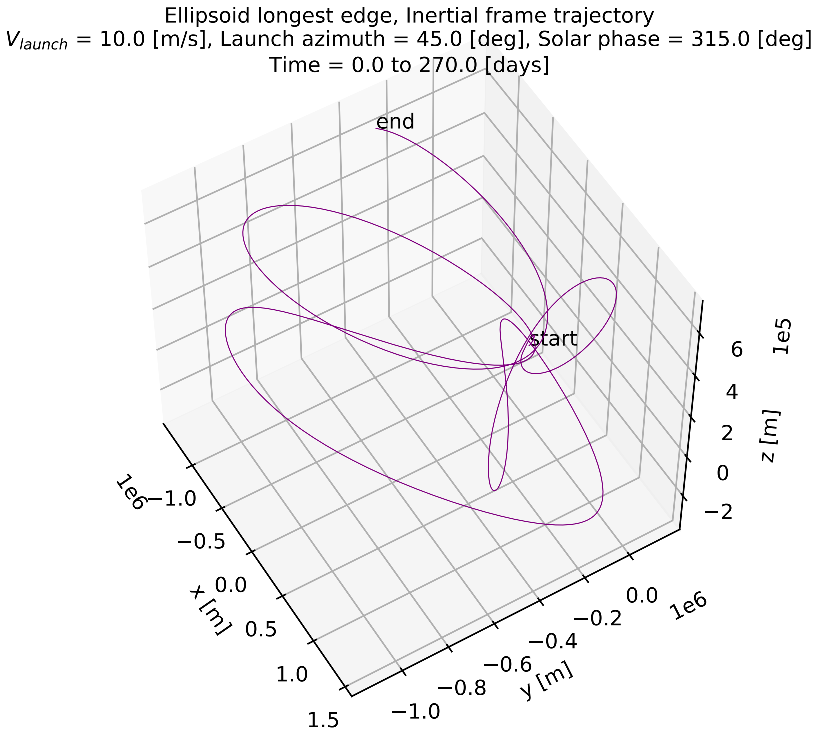

(a)

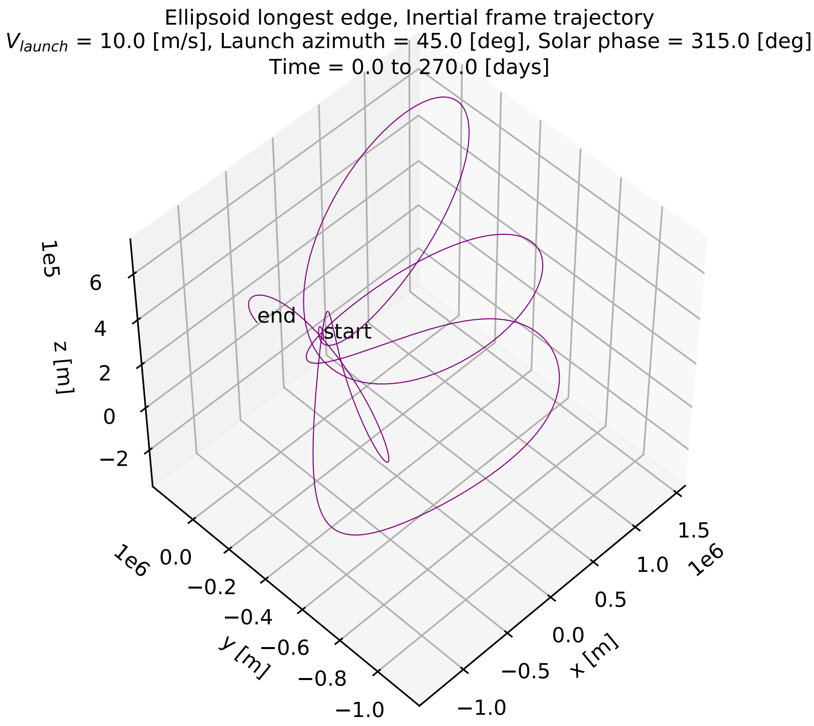

(b)

Figure 7.16: 3D inertial frame trajectory of capture regolith for case number 5 in Table 7.2 in two different viewing angles. Particle code LoGSP-1.

Note that in the trajectory animation in Figure 7.14 (and any other animation included henceforth) the particle is made to skip several data points in between along the trajectory when it is far away from the asteroid, just to reduce the length of the animation. So because of this, the particle appears to be moving faster when it is away from the asteroid but this is not true. For the exact velocity of the particle, the reader should look at the velocity magnitude indicator within the animation itself.

The animation shows that the particle reverses its direction of motion twice in its entire course. To visualize how this is happening in 3D, look at Figure 7.16. The reason for this can be understood by looking at the direction of the perturbing acceleration, the gravitational acceleration vectors, and the combined effect of all accelerations acting on the particle. The direction of SRP and STBE are shown in Figure 7.18 and that of the net effect of the two is shown in Figure 7.19a. In the trajectory simulator, the gravity model (triaxial ellipsoid model) computes the acceleration in the rotating frame. We calculated the direction of the gravitational acceleration in inertial frame in post-simulation analysis assuming a point-mass model by considering the fact that when the regolith is far-away from the asteroid, its gravity field would appear as that of a point-mass gravity source. The gravitational acceleration vectors are shown in Figure 7.19b. The net acceleration acting on the particle is then shown in Figure 7.20. All acceleration vectors are shown along those parts of the trajectory where the magnitude of SRP acceleration is of the same order of magnitude as that of the gravitational acceleration. However, the magnitude of the STBE acceleration is always 1.0 order of magnitude smaller than the gravitational acceleration for those very same points along the trajectory, but is still significant. We do not show the vectors for the entire trajectory for two reasons; first, when close to the asteroid the direction of these vectors would reduce the clarity of the plot and, second, we want to discuss the effect of the perturbations when the particle is far away from the asteroid because then they are as significant as the gravitational force.

In Figure 7.17, the trajectory loops numbered 1 and 2 (XY plane), is where the particle's direction of motion gets reversed. If we look at Figure 7.18a, we see that the direction of the SRP vector is consistent with how the particle changes its direction of motion. This, however, does not mean that the SRP is the sole actor responsible for how the particle's motion eventually turns out to be (and we will see this in detail shortly). The direction of STBE, as shown in Figure 7.18b, however, does not directly tell us on how the particle's motion would change as it progresses through its trajectory. STBE is always an order of magnitude smaller than SRP for the points shown in the two plots and its direction is not consistent with how the particle changes its direction of motion but its contribution to the capture scenario is significant (we will see the effect of removing STBE shortly). The direction of the net perturbing acceleration, shown in Figure 7.19a, shows us exactly how and where the motion of the particle is directed. Especially when we look at trajectory loops 1 and 2 in Figure 7.17, we can see that the net perturbing vector is acting in the direction that is consistent with how the particle changes its orbital motion. Now looking at these plots that we just discussed, a question that arises is that - why did the particle remain in a temporary capture orbit, and for example not escape especially when the net perturbing acceleration was acting opposite to the direction of asteroid such as in trajectory loop number 3 in Figure 7.17? The answer to this is found by looking at the direction of gravitational attraction in Figure 7.19b and the total acceleration (i.e. the net effect of gravity and perturbations) acting on the particle in Figure 7.20. Although the gravitational acceleration has the same order of magnitude as that of the Solar perturbations when the particle is far away from the asteroid, we see that the net effect of the two is towards the asteroid and hence prevents the particle from escaping.

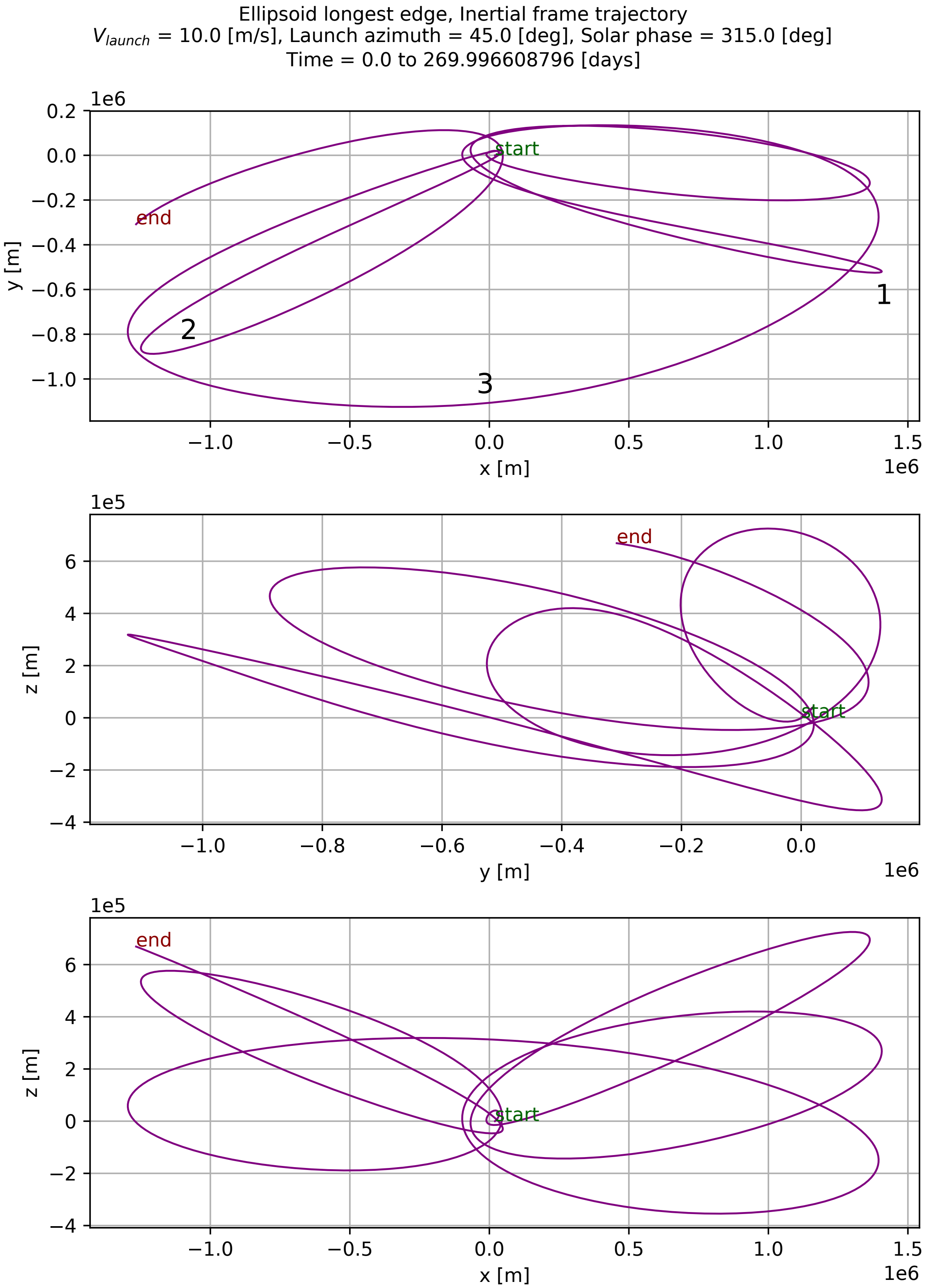

Figure 7.17: 2D inertial frame trajectory of capture regolith for case number 5 in Table 7.2. Particle code LoGSP-1.

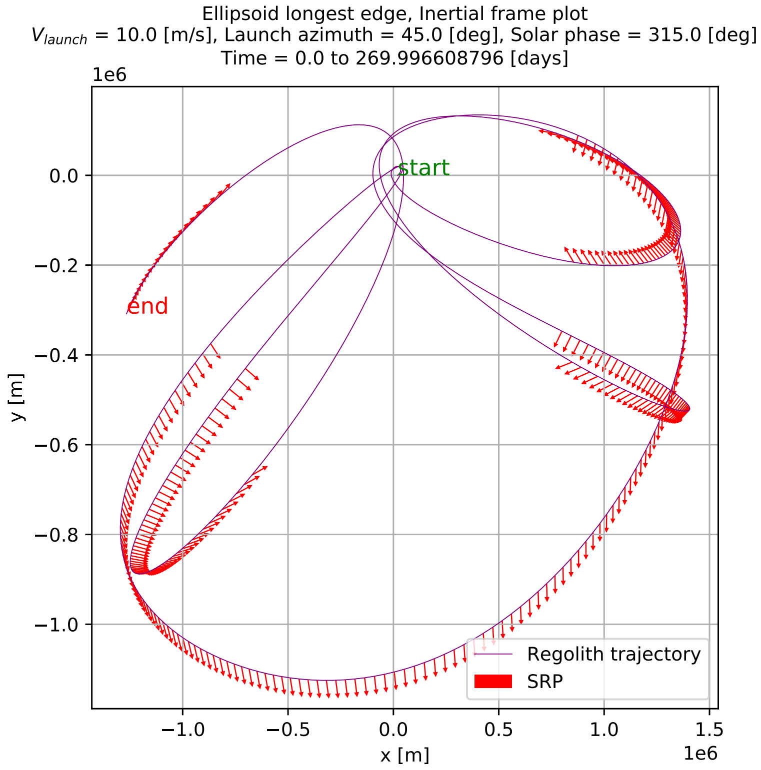

(a)

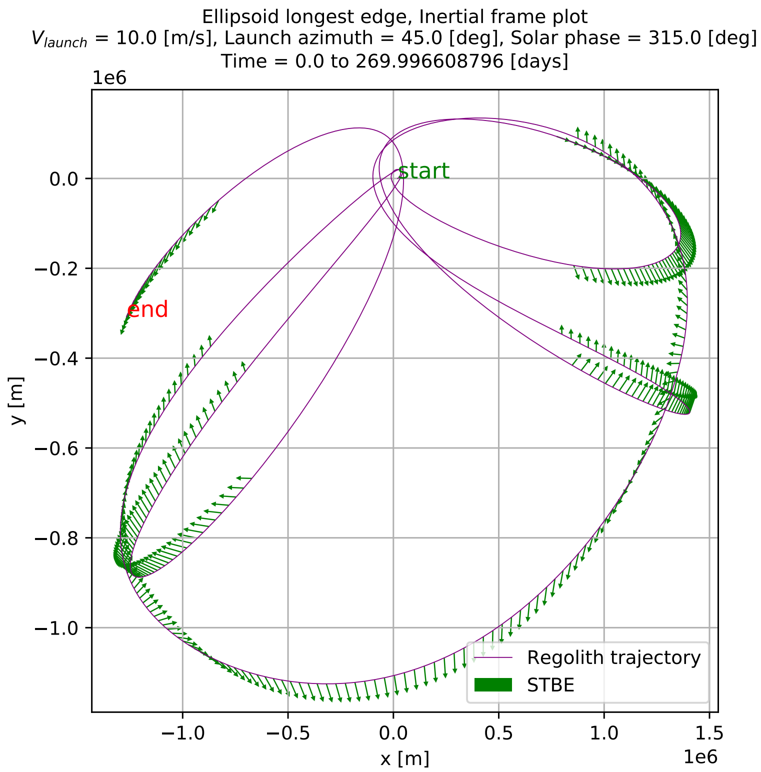

(b)

Figure 7.18: 2D trajectory of capture regolith for case number 5 in Table 7.2 with direction of SRP and STBE perturbation vectors. Note that the vectors are shown only for those parts of the trajectory where the SRP magnitude is of the same order as that of the asteroid's gravitational acceleration. For those very same points along the trajectory, the magnitude of the STBE is always 1.0 order of magnitude smaller than the gravitational acceleration. Particle code LoGSP-1.

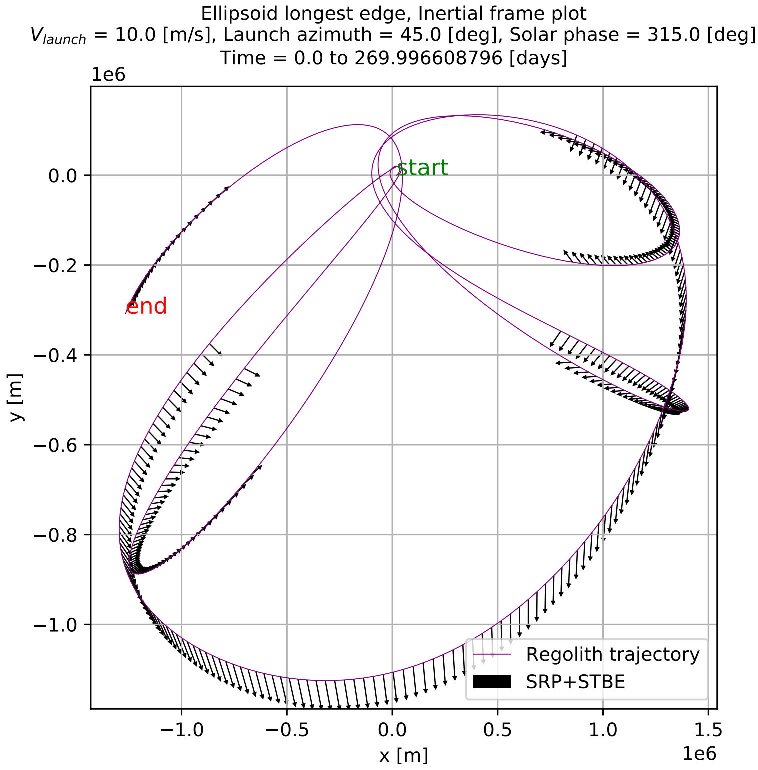

(a)

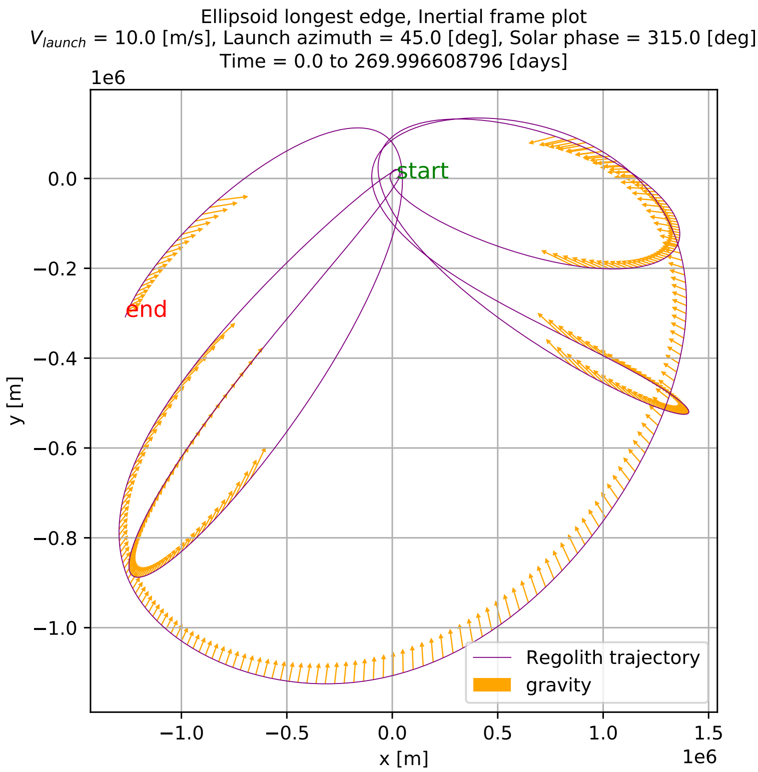

(b)

Figure 7.19: 2D trajectory of capture regolith for case number 5 in Table 7.2 with direction of the sum total of SRP and STBE perturbation vectors, and the direction of the gravitational acceleration vector for the same data points. Note that the vectors are shown only for those parts of the trajectory where the SRP magnitude is of the same order as that of the asteroid's gravitational acceleration. For those very same points along the trajectory, the magnitude of the STBE is always 1.0 order of magnitude smaller than the gravitational acceleration. Particle code LoGSP-1.

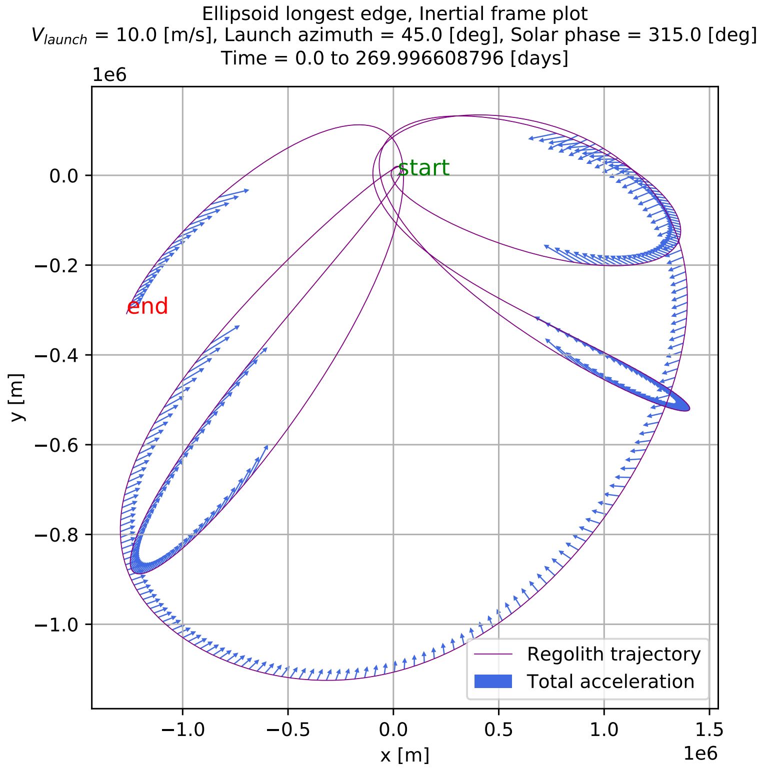

Figure 7.20: 2D trajectory of capture regolith for case number 5 in Table 7.2 with direction of the net acceleration vector. Note that the vectors are shown only for those parts of the trajectory where the SRP magnitude is of the same order as that of the asteroid's gravitational acceleration. For those very same points along the trajectory, the magnitude of the STBE is always 1.0 order of magnitude smaller than the gravitational acceleration. Particle code LoGSP-1.

Both SRP and STBE together are necessary in getting the capture trajectory shown in Figure 7.17. If either one of them is removed from the simulation, for the same launch conditions and initial Solar phase angle, then the results are completely different and we do not get a capture orbit. Note that the definition of capture orbit in this context implies that the particle stays in an orbit around the asteroid for the complete duration of 270.0 [days], i.e., the maximum time for which the simulation is run.

When only STBE is removed, then we get a trajectory where the particle eventually escapes the asteroid. This is shown in Figure 7.21. The trajectory is completely different from the one in Figure 7.17, even though the only difference between the two simulations is the omittion of STBE perturbation. Figure 7.22a shows the direction of perturbing acceleration due to SRP and the gravitational acceleration for those points along the trajectory where both have the same order of magnitude. The direction for the net acceleration acting on the particle is shown in Figure 7.22b. The trajectory of the particle starts out the same way in both Figure 7.21 and Figure 7.17 however due to the lack of STBE perturbation, the trajectories soon start to differ from each other. Upon comparing Figure 7.20 and Figure 7.22b we can infer that the trajectories differ because the with the lack of STBE the direction of the net acceleration vector differs for the two trajectories which eventually directs how the particle motion would progress. The particle trajectory in Figure 7.21 eventually leads to an escape scenario. Now if we look at Figure 7.22a, towards the end of the trajectory, the direction of the gravitational vector gradually changes and starts to point along the instantaneous tangent to the trajectory, all the while with the SRP vector point away from the asteroid. The net effect of this situation can be seen in Figure 7.22b; we see that the net acceleration vector starts pointing away from the asteroid towards the end segment of the trajectory and thus this is when the particle escapes.

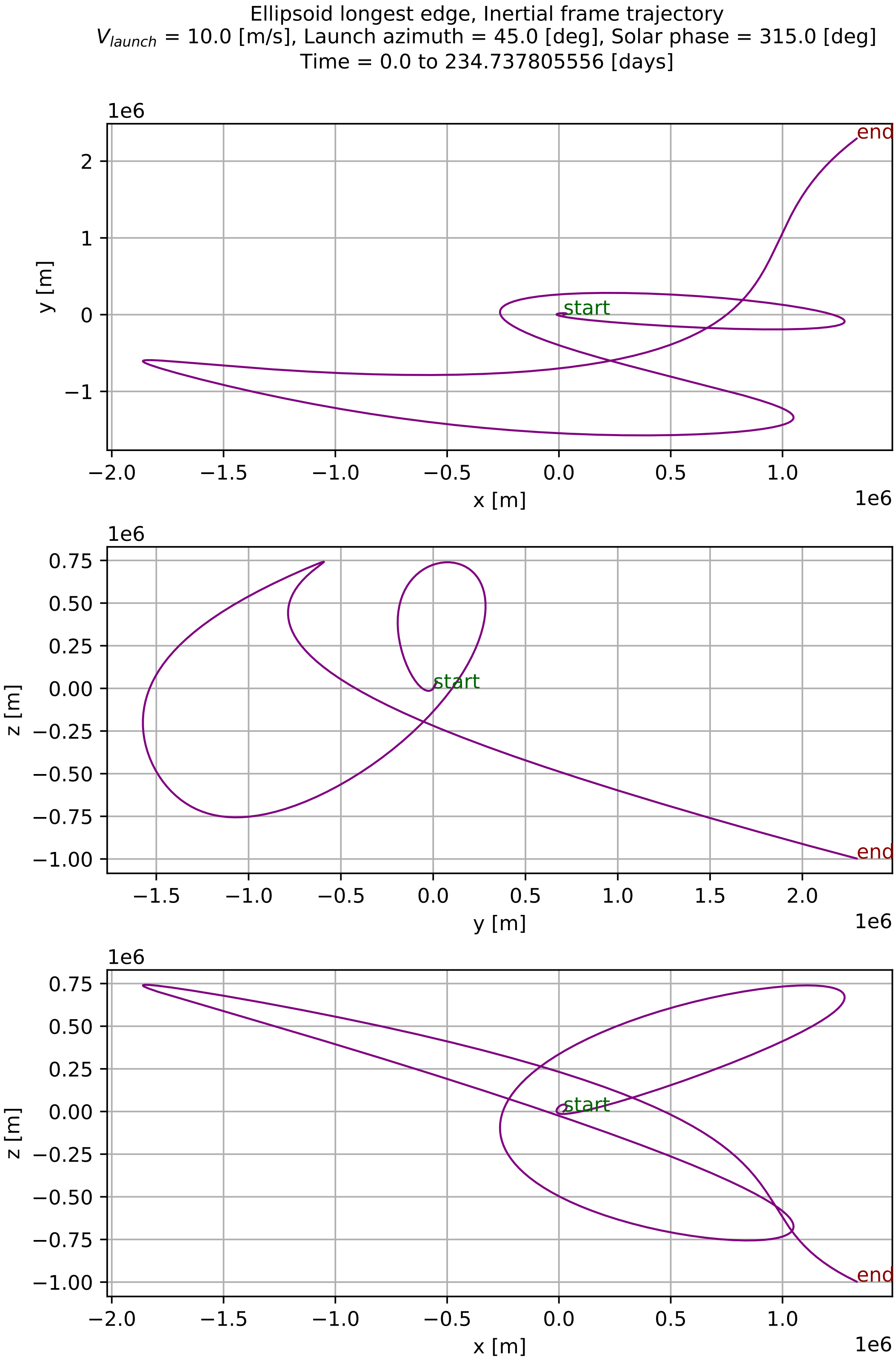

Figure 7.21: 2D trajectory of particle for same initial conditions as that of capture case 5 in Table 7.2 except that only SRP was included in this simulation. Particle code LoGSP-1.

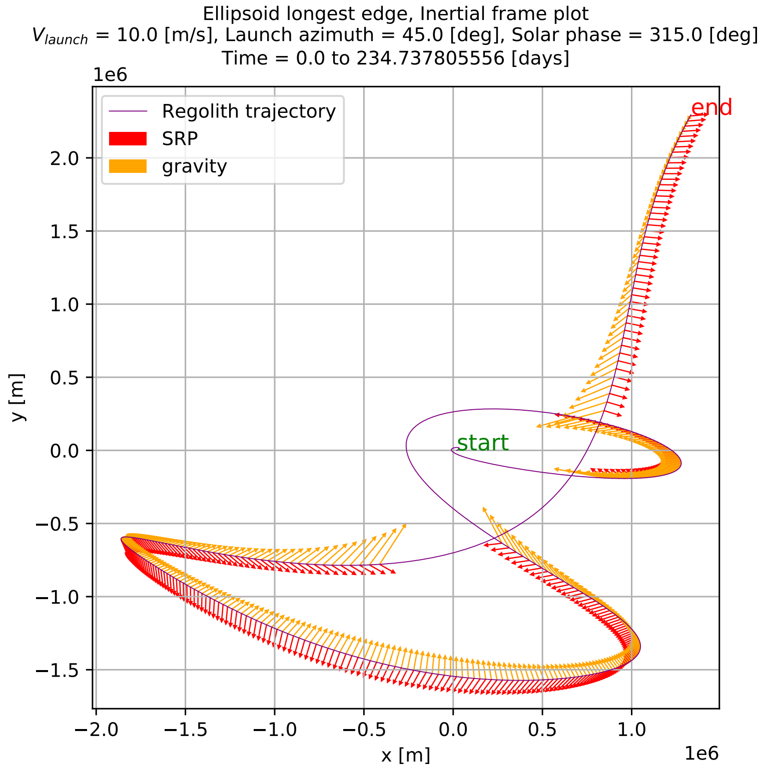

(a)

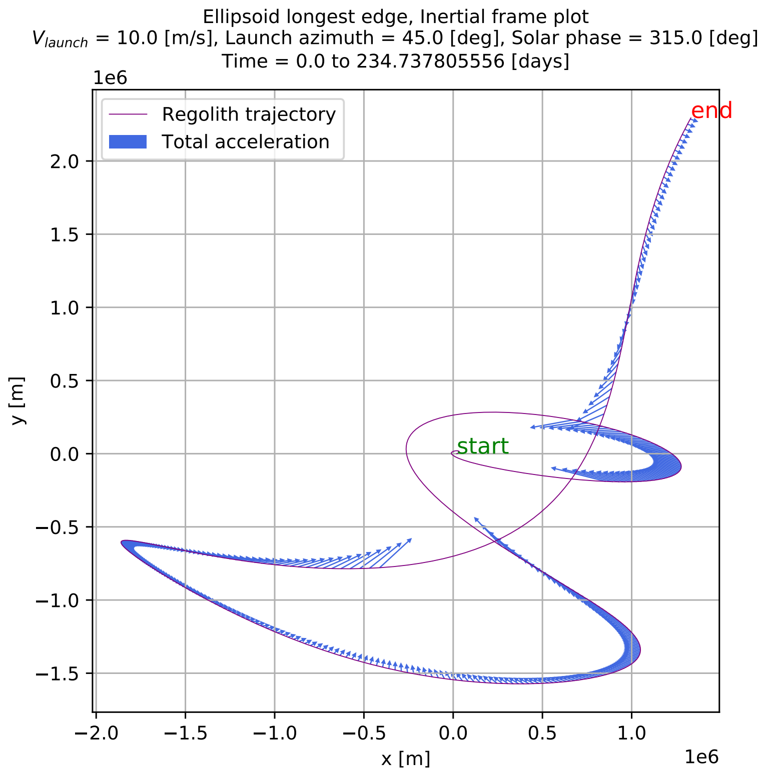

(b)

Figure 7.22: Inertial frame XY plane trajectory for same launch conditions as that of capture case 5 in Table 7.2: (a) showing direction of SRP acceleration and gravitational acceleration & (b) showing direction of the net acceleration acting on the particle. Vectors are shown only for those parts of trajectory where acceleration due to SRP and gravity have the same order of magnitude. Note that STBE perturbation was not part of the simulation here. Particle code LoGSP-1.

When we keep STBE but remove SRP from our simulations, then the trajectory again leads to an escape situation, only this time its much faster. The 2D inertial frame trajectory is shown in Figure 7.24. The trajectory shows similarity only for a brief moment immediately after launch (notice the small loop after 'start') with the capture case in Figure 7.17 but soon after the particle is on a trajectory that never comes back around the asteroid. The reason for this is clear and simple if one looks at the direction of acceleration due to gravity and STBE in Figure 7.25a and their net effect in Figure 7.25b. Initially, from the point when we show these vectors, we know that the magnitude of STBE acceleration is 1.0 order of magnitude smaller than the gravitational acceleration (see Figure 7.26) and even then the direction of the net acceleration vector is such that the trajectory can not loop around the asteroid. The STBE magnitude increases soon enough to the same order as that of gravitational acceleration and the net acceleration vector direction never points towards the asteroid which eventually causes the particle to escape. However, the point where the magnitude curves of STBE and gravitational acceleration cross is not the point where the escape occurs as is evident from the plot for total energy and eccentricity in Figure 7.23.

From this analysis, we can say that effect of removing SRP from simulations had a much drastic effect than removing just the STBE. Both cases lead to an escape situation and the combined effect of both the perturbations leads to a capture orbit, for the same launch conditions and initial Solar phase angle. The behavior of the trajectory, in all cases, can be easily understood by looking at the direction of the net acceleration vector, especially when the particle is far away from the asteroid because it tells us exactly, how by adding perturbations, the motion of the particle is affected and not just in terms of its final fate but even in terms of changing its orbital direction.

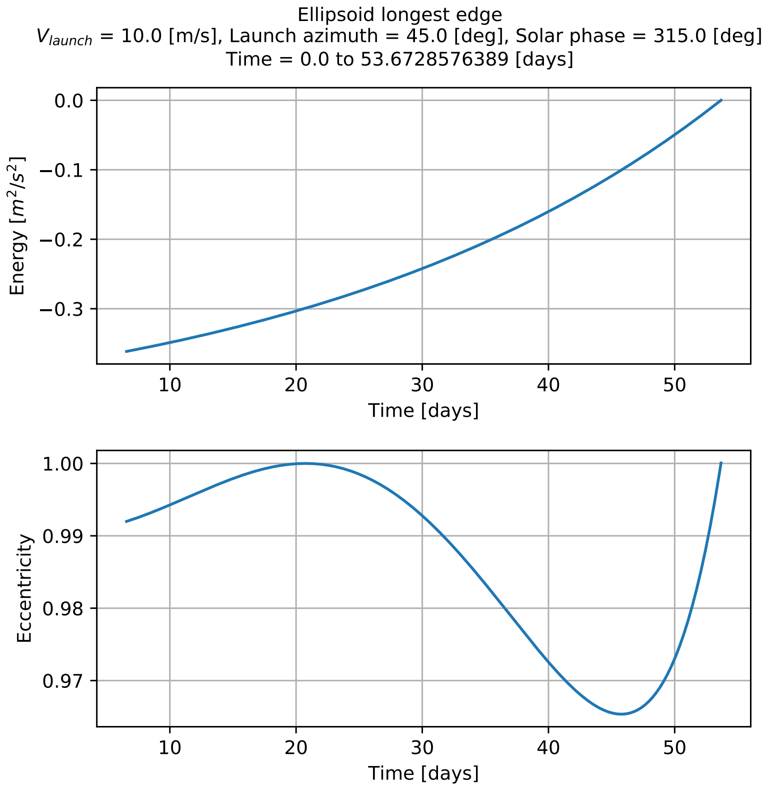

Figure 7.23: Evolution of total energy of the particle and its orbital eccentricity. Particle has the same initial conditions as that of capture case 5 in Table 7.2 except that only STBE was included in this simulation. The range of data points plotted is the same as that in Figure 7.25. Particle code LoGSP-1.

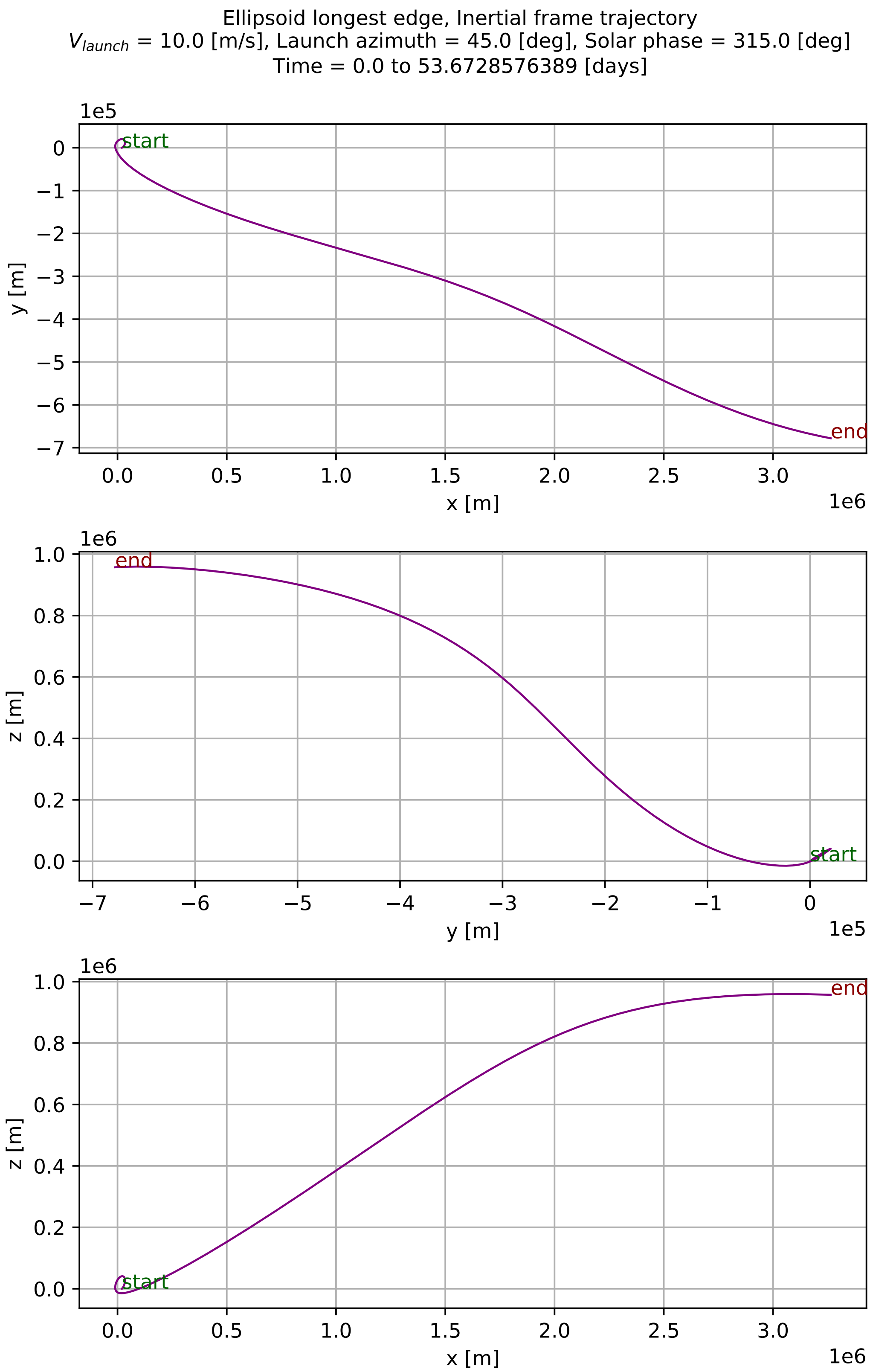

Figure 7.24: 2D trajectory of particle for same initial conditions as that of capture case 5 in Table 7.2 except that only STBE was included in this simulation. Particle code LoGSP-1.

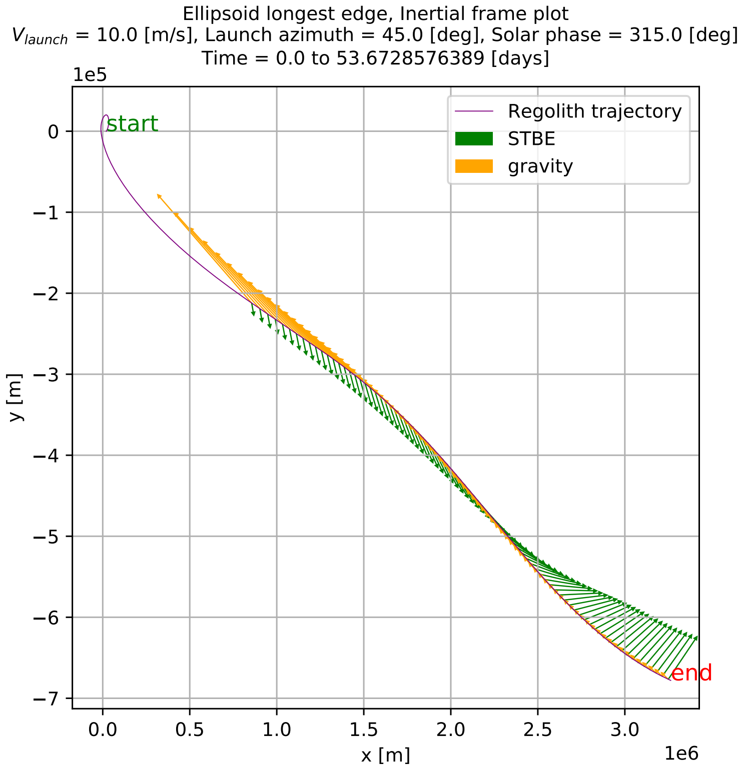

(a)

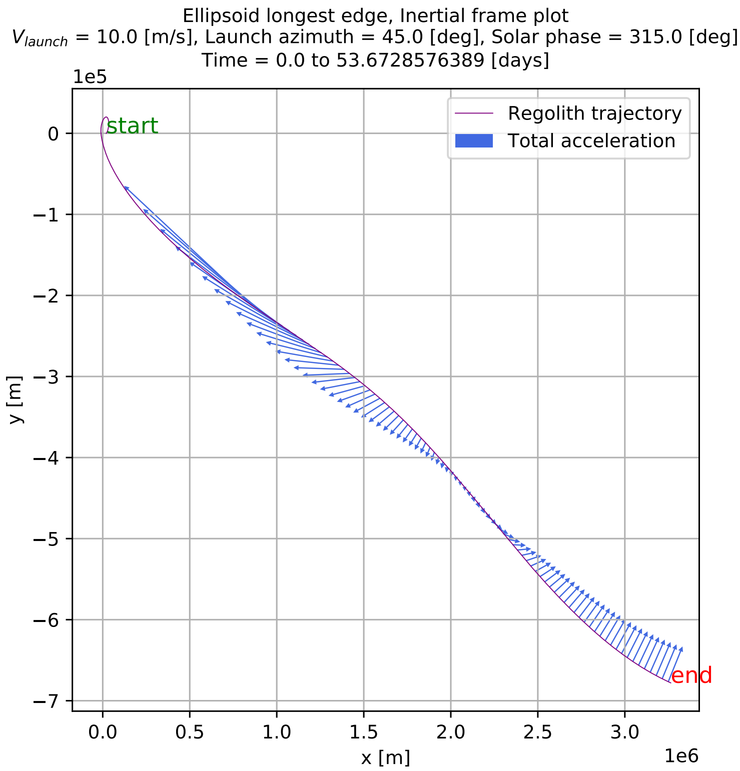

(b)

Figure 7.25: Inertial frame XY plane trajectory for same launch conditions as that of capture case 5 in Table 7.2: (a) showing direction of STBE acceleration and gravitational acceleration & (b) showing direction of the net acceleration acting on the particle. Vectors are shown only for those parts of trajectory where acceleration due to STBE is equal to gravitational acceleration or smaller than it by 1.0 order of magnitude. Note that SRP perturbation was not part of the simulation here. Particle code LoGSP-1.

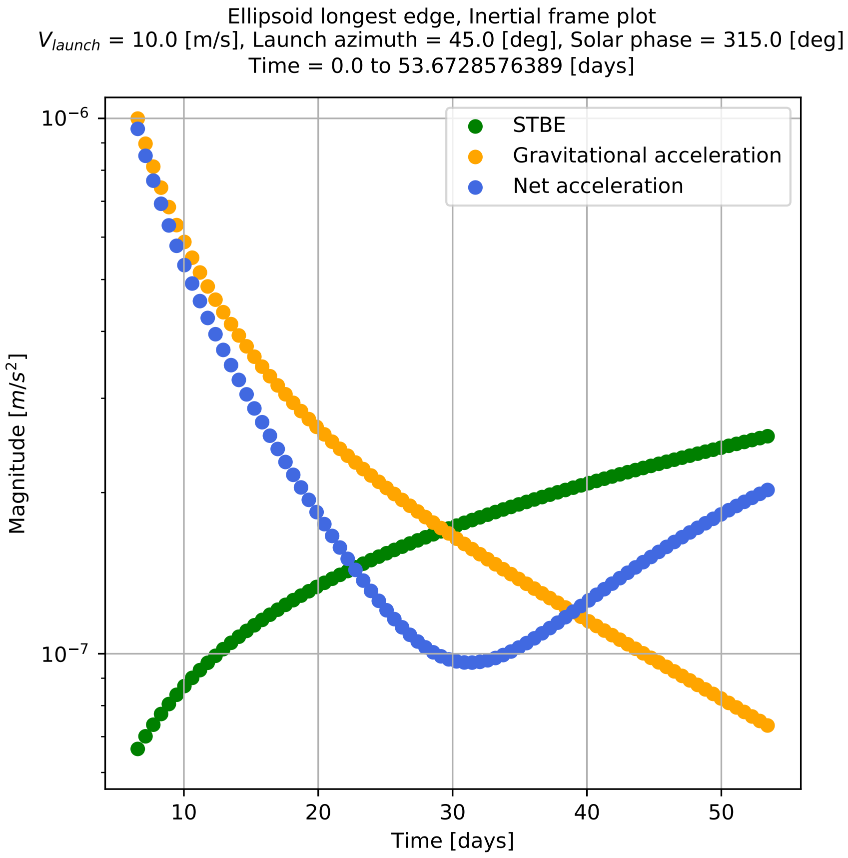

Figure 7.26: Magnitudes of acceleration due to gravity, STBE and the net effect of the two for the corresponding vectors as shown in Figure 7.25. Particle code LoGSP-1.

Figure 7.27 shows the 3D trajectory for completely different launch conditions (see capture case 8 in Table 7.2). The 3D trajectory as viewed from the asteroid centric body fixed frame is shown in Figure A.4. The 2D trajectory projections for the same, in inertial and body fixed frames, are shown in Figure 7.28 and Figure A.5 respectively. Just like in the previous case, we see from the animation (see Figure 7.32) and the 3D trajectory for current launch conditions, that the particle direction of motion is reversed twice in its course. These two locations are marked by numbers 1 and 2 in Figure 7.28. At location number 1 we see that the motion changes from anti-clockwise to clockwise direction in the XY plane. The case for location number 2 is exactly the opposite. If we look at Figure 7.30a, the change in direction of motion is consistent with the direction in which the net perturbing force is acting. Ultimately, when we look at the net acceleration acting on the particle in Figure 7.31, we can understand how exactly the particle would orbit around the asteroid. The net force, gravitational and perturbations combined, act in a direction such that the particle is forced to change its orbital motion direction at the two locations previously explained. The acceleration vectors in Figures 7.29 to 7.31 are plotted for points along the trajectory where the magnitude of acceleration due to SRP is of the same order of magnitude as the gravitational acceleration. Again, the magnitude of STBE is 1.0 order of magnitude smaller than the gravitational acceleration for the same data points along the trajectory.

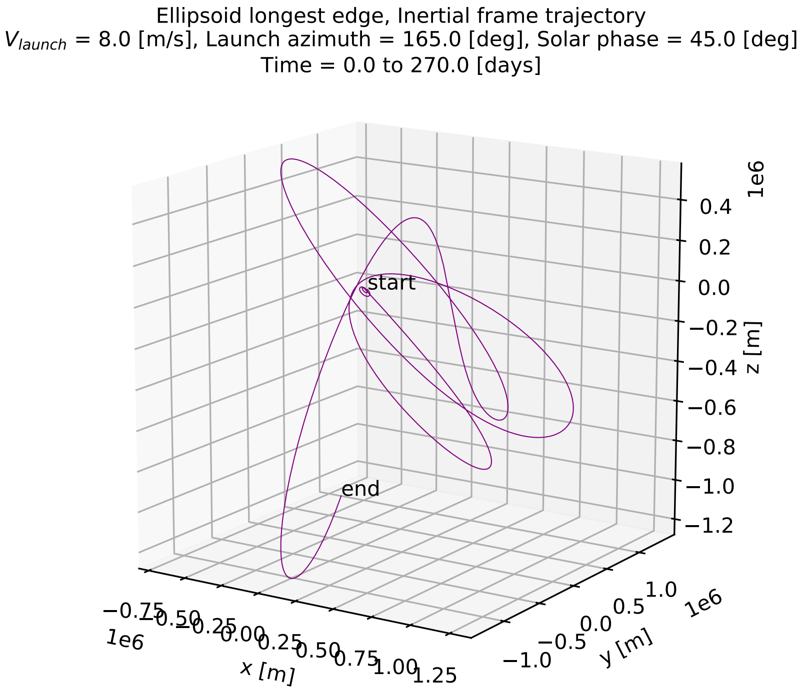

(a)

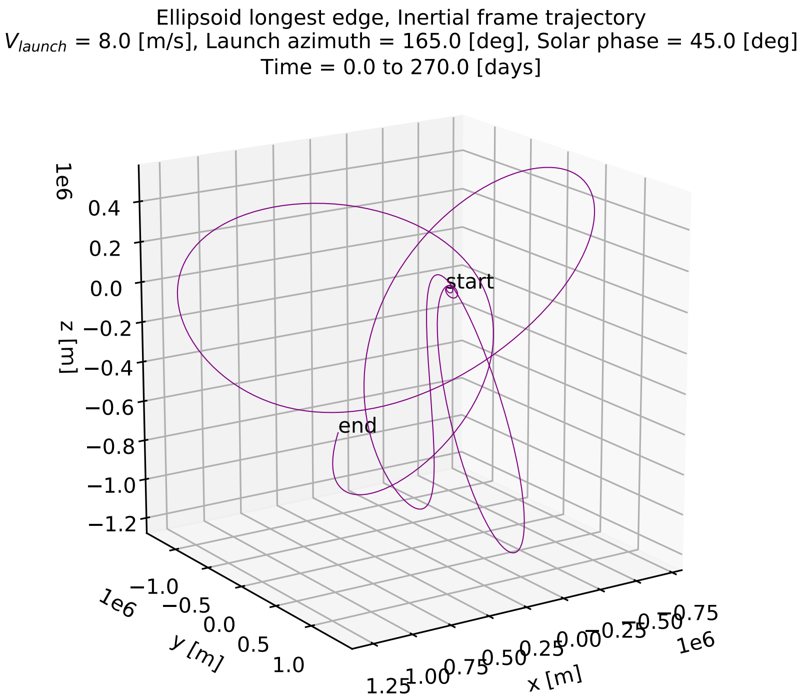

(b)

Figure 7.27: 3D inertial frame trajectory of capture regolith for case number 8 in Table 7.2 from two different viewing angles. Particle code LoGSP-1.

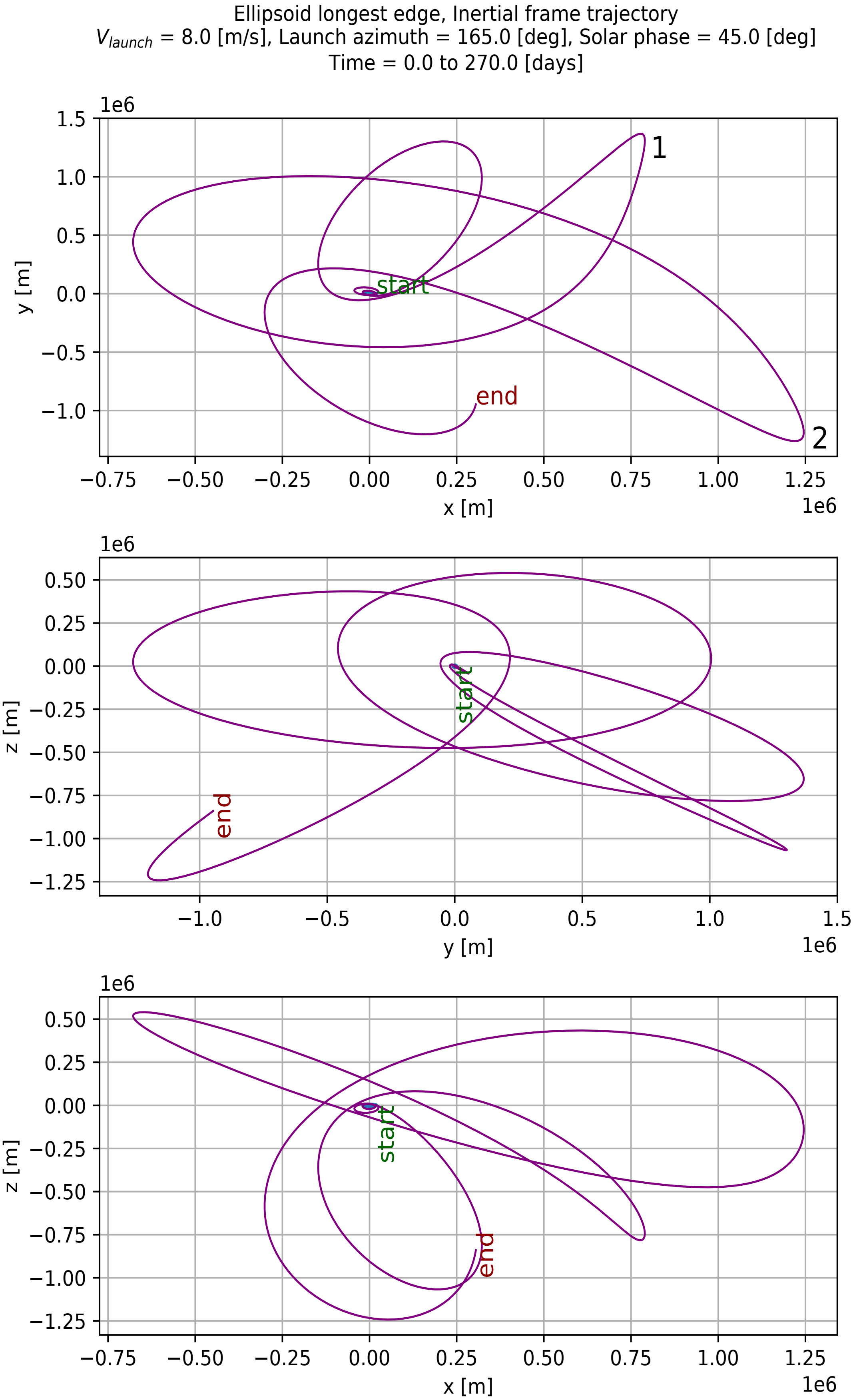

Figure 7.28: 2D inertial frame trajectory of capture regolith for case number 8 in Table 7.2. Particle code LoGSP-1.

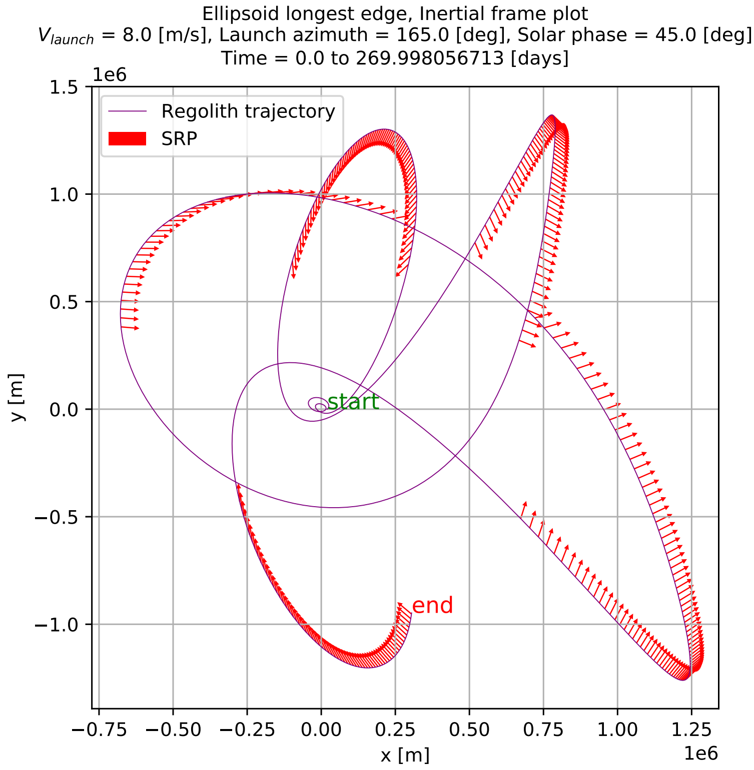

(a)

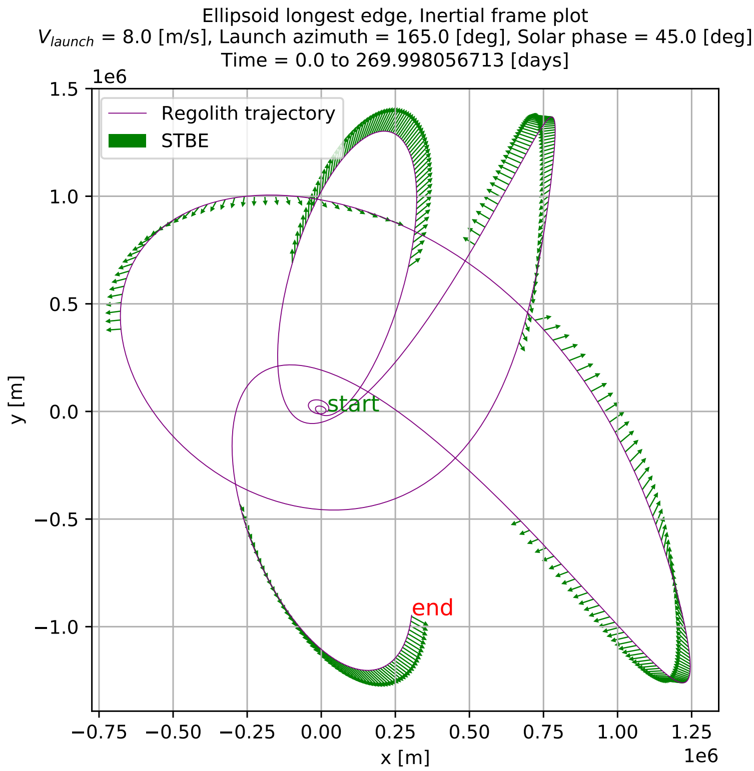

(b)

Figure 7.29: 2D trajectory of capture regolith for case number 8 in Table 7.2 with direction of SRP and STBE perturbation vectors. Note that the vectors are shown only for those parts of the trajectory where the SRP magnitude is of the same order as that of the asteroid's gravitational acceleration. For those very same points along the trajectory, the magnitude of the STBE is always 1.0 order of magnitude smaller than the gravitational acceleration. Particle code LoGSP-1.

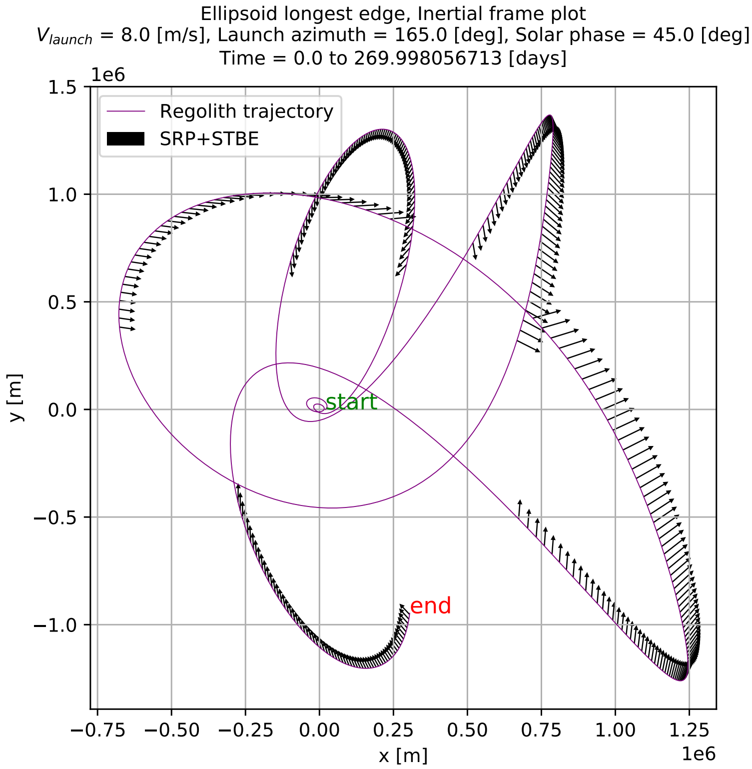

(a)

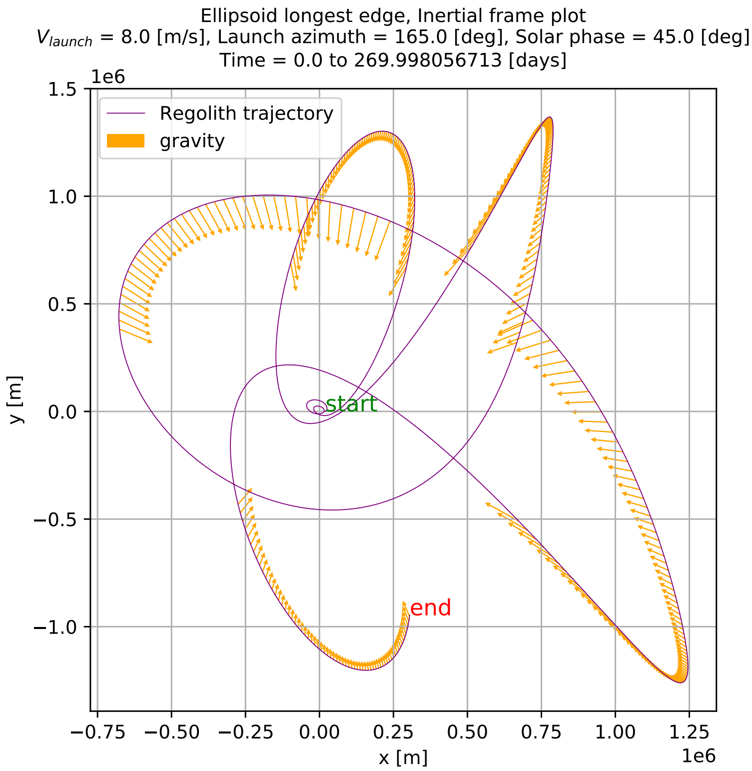

(b)

Figure 7.30: 2D trajectory of capture regolith for case number 8 in Table 7.2 with direction of the sum total of SRP and STBE perturbation vectors, and the direction of the gravitational acceleration vector for the same data points. Note that the vectors are shown only for those parts of the trajectory where the SRP magnitude is of the same order as that of the asteroid's gravitational acceleration. For those very same points along the trajectory, the magnitude of the STBE is always 1.0 order of magnitude smaller than the gravitational acceleration. Particle code LoGSP-1.

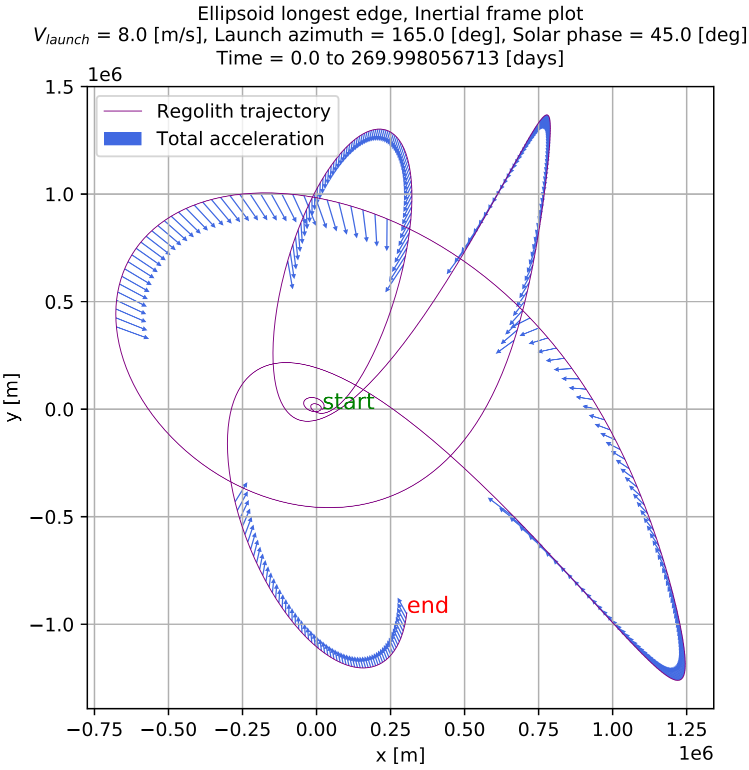

Figure 7.31: 2D trajectory of capture regolith for case number 8 in Table 7.2 with direction of the net acceleration vector. Note that the vectors are shown only for those parts of the trajectory where the SRP magnitude is of the same order as that of the asteroid's gravitational acceleration. For those very same points along the trajectory, the magnitude of the STBE is always 1.0 order of magnitude smaller than the gravitational acceleration. Particle code LoGSP-1.

Figure 7.32: 2D trajectory animation (XY Plane) of capture regolith for case number 8 in Table 7.2. Particle code LoGSP-1. Scan the QR code to view the animation or use the following web-link: `https://youtu.be/CceYRlNvAiM`

We saw in the analysis of capture case number 5 for particle LoGSP-1 that both SRP and STBE were necessary for getting that specific capture trajectory and removal of either of the perturbations resulted in a different final fate for the same particle. The next analysis that we present now, will tell us about how a capture scenario occurs, relative to a situation when all perturbations are removed, for the same initial launch conditions in both cases. We do the analysis for capture case number 8 from Table 7.2. Figure 7.34a shows two different trajectories for the particle launched with the same initial conditions. The one shown in dotted line is for the case when Solar perturbations were omitted from the simulation, which eventually results in the particle escaping the asteroid after 1.4 [days]. The one in the solid line shows the capture trajectory (actually a section of the entire capture trajectory as seen in Figure 7.28) when Solar perturbations were included in the simulation. Note that we show the perturbed trajectory (capture case) for the same amount of time (1.4 [days] instead of 270.0 [days]) as taken by the unperturbed trajectory (escape case) to be able to do a one-to-one comparison. The arrows plotted along this trajectory indicate the direction of the net perturbing acceleration due to SRP and STBE. Figure 7.33 directs to an animation for both the unperturbed and perturbed trajectory.

Figure 7.33: 2D trajectory animation (XY Plane) of capture regolith for case number 8 in Table 7.2, compared with that of its unperturbed counterpart. Particle code LoGSP-1. Scan the QR code to view the animation or use the following web-link: `https://youtu.be/CdFKKR3UDJ0`

From the animation we can see that even as the particle has just been lofted from the surface of the asteroid, there are very subtle and minute differences in the range to the particle and its velocity, between the perturbed and unperturbed trajectory. The first visible difference between the two trajectories becomes noticeable at point *"A"* in Figure 7.34a. It is easy to deduce the change in the perturbed trajectory from the direction of the net perturbing acceleration up until this point. The same point *"A"* is also marked in Figure 7.34b. It is from this point that we can see noticeable difference between the two trajectories as well as in their corresponding energies. A snippet from the trajectory animation, corresponding to the point *"A"*, is shown in Figure 7.38a which highlights the differences in range and velocity of the particles in the two trajectories. Note that in Figure 7.38a, the difference in the velocity between the perturbed and unperturbed cases is relatively small, compared to almost 1 [km] of a difference in range of the particles. The latter is significant since the particles have dimensions in the order of [cm]. From point *"A"* onwards these differences continue to grow and only get larger as the trajectory proceeds.

Similarly, at point *"B"* in Figure 7.34a, we see a much larger difference in the two trajectories. In Figure 7.34b, we see that around point *"B"* both trajectories have a positive energy which quickly comes down to a negative value for the perturbed trajectory, hence keeping it bounded which results in a capture scenario. However, this does not happen for the unperturbed trajectory, leading to an escape scenario. The difference in the state of the two particles at point *"B"* are relatively larger and can be seen in Figure 7.38b. The differences in the two trajectories, computed in the asteroid centric rotating frame, is shown in Figure 7.35. The plot on the bottom shows the trajectory for 1.4 [days] (i.e. until escape for the unperturbed trajectory) as viewed in the rotating frame, and the plot on the right zooms into a small part of this trajectory to show how Solar perturbations are responsible for changing the course of the particle. It is seen with a bit more clarity on how the net perturbation vector pulls the trajectory away from the trace of the unperturbed one.

So what we are seeing here is, that due to the inclusion of perturbations from the Sun, the motion of the particle changed from its unperturbed counterpart. This change was not drastic in terms of the initial shape of the trajectory as seen in Figure 7.34a. But the change was just enough for the particle to have a different phase with respect to the asteroid, relative to the unperturbed trajectory as seen in Figure 7.38. By phase, we refer to the location of the particle with respect to a given rotational state of the asteroid. So if two particles are at different locations, at any given epoch and for the same rotational state of the asteroid, they will have different magnitudes of forces acting on them which would ultimately lead to different final outcomes.

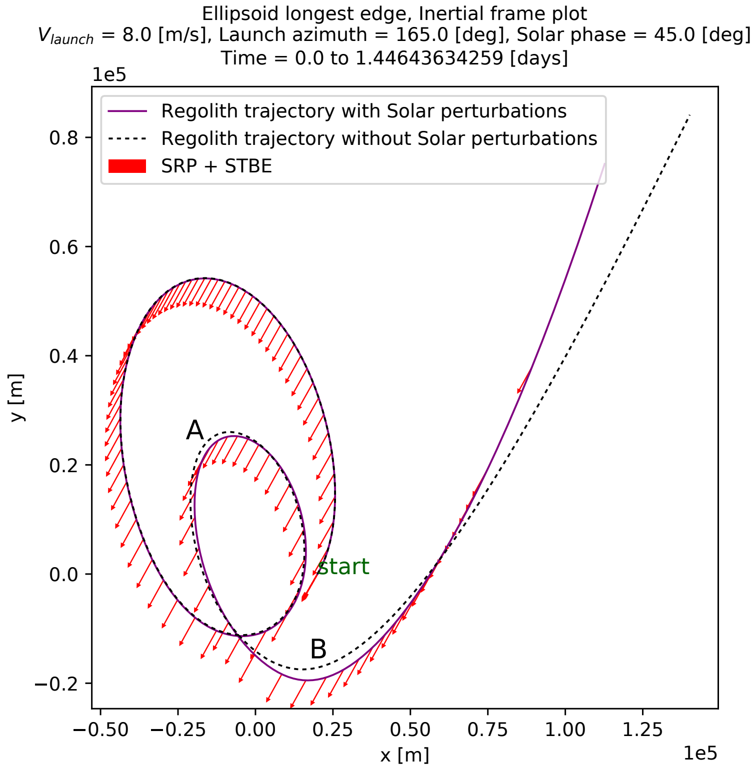

(a)

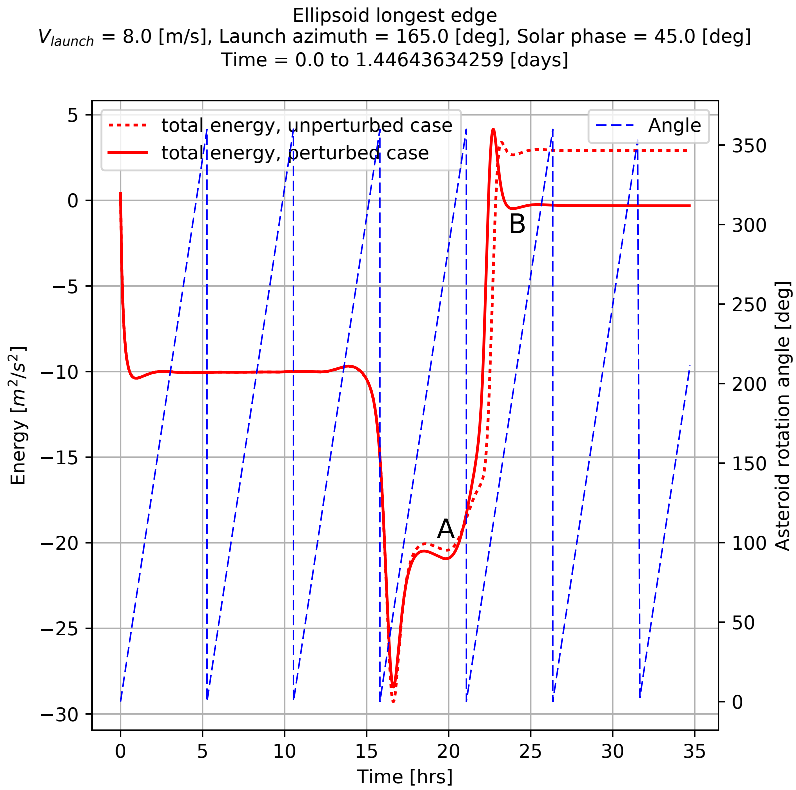

(b)

Figure 7.34: Comparative analysis of capture case 8 in Table 7.2 with a particle trajectory where the initial conditions are same as the former but the simulation was done without Solar perturbations. Figure 7.34a compares the XY plane trajectory & Figure 7.34b compares their total energy. Particle code LoGSP-1.

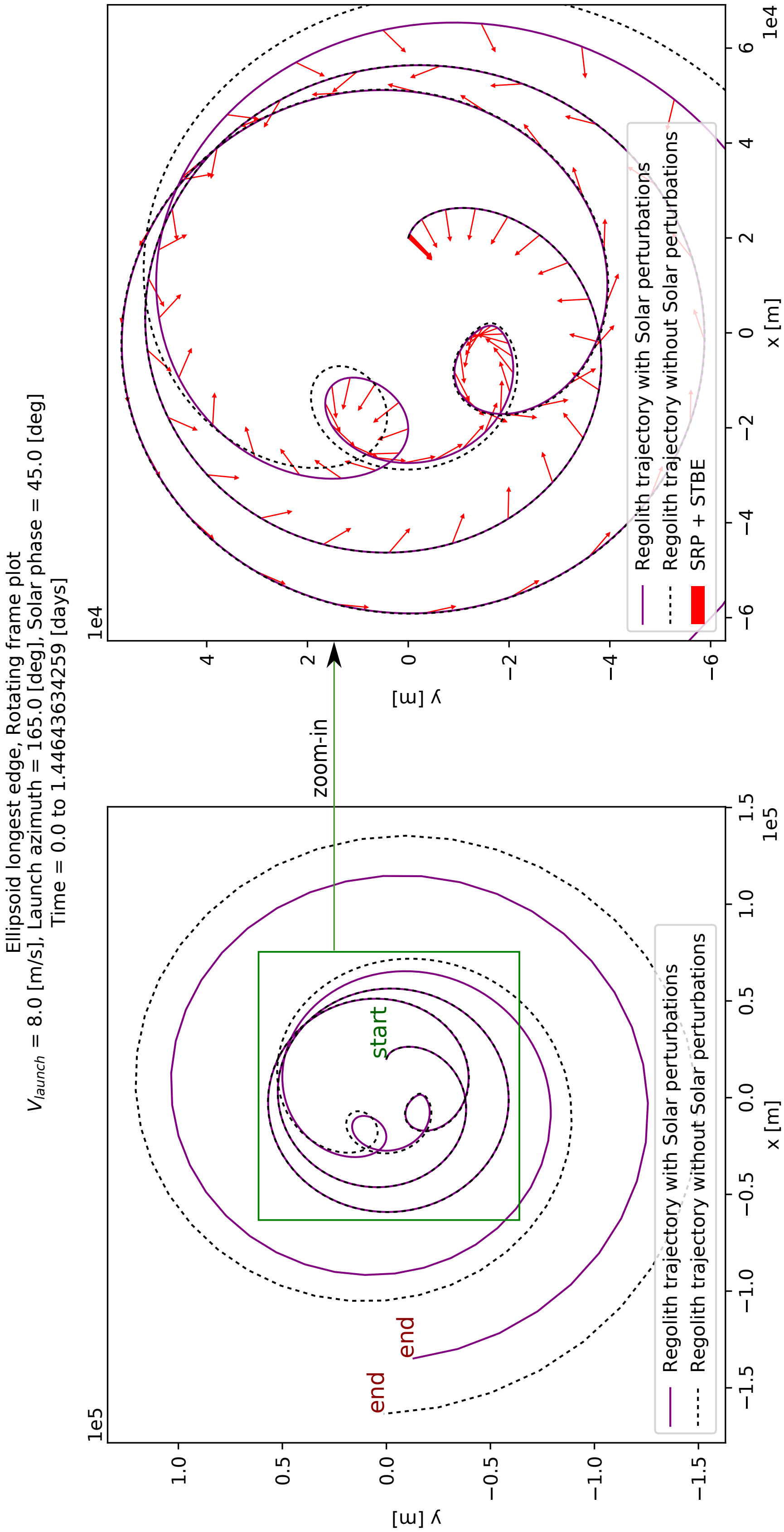

Figure 7.35: Rotating frame 2D trajectory (XY plane) of capture regolith for case number 8 in Table 7.2 with direction of the net perturbation vector, compared with the trajectory of a particle launched with the same initial conditions but in absence of Solar perturbations. Particle code LoGSP-1.

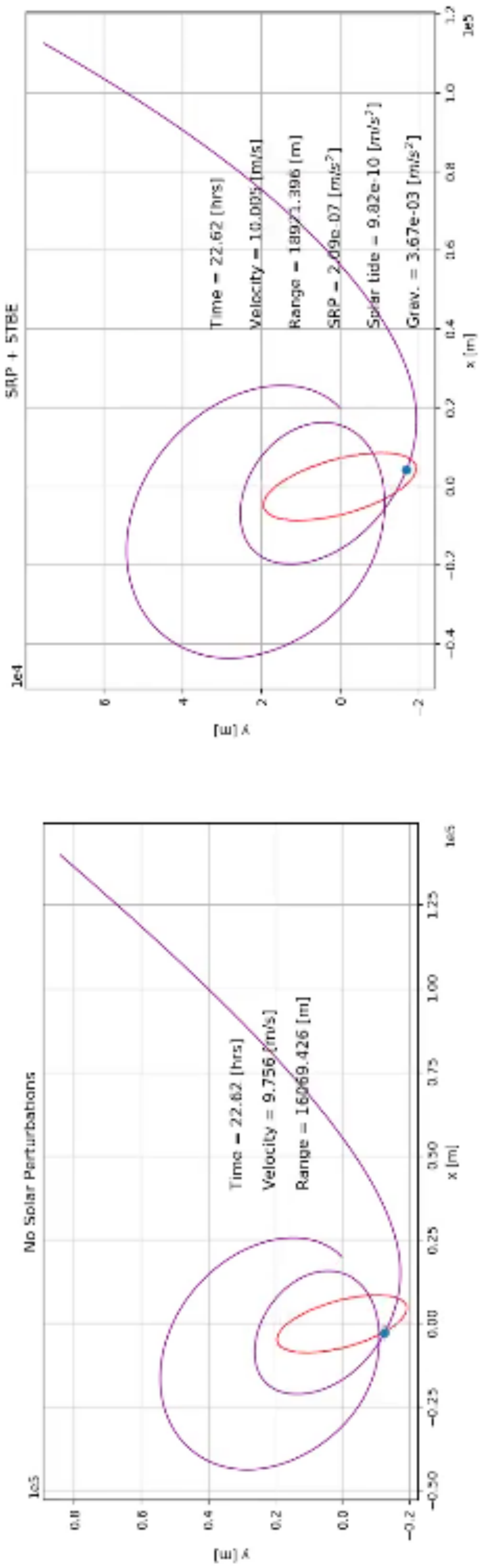

Figure 7.36: Snapshot from animation of the perturbed trajectory of capture case 8 in Table 7.2 compared with that of its unperturbed counterpart. The unperturbed trajectory is still being accelerated at the given instant however the particle in the perturbed trajectory is being decelerated. Particle code LoGSP-1.

If we look at the trajectory animation in Figure 7.33, one would notice that at around point *"B"*, the particle in the unperturbed trajectory is being accelerated by the gravitational pull of the asteroid while the particle in the perturbed trajectory is being slowed down. A snapshot of this scenario from the animation is shown in Figure 7.36. Although this situation does not happen for extended periods of time, but only while approaching point *"B"*, we see that the particle in the unperturbed trajectory has relatively higher velocity while moving forth of point *"B"* and leaving the vicinity of the asteroid, relative to the particle in the perturbed trajectory. The latter thus stays in a capture orbit while the former has enough velocity to escape. A plot for this is shown in Figure 7.37.

Note that in the capture case just discussed, the magnitude of the perturbing accelerations is much smaller than the gravitational acceleration. The effect of the perturbations on the particle's trajectory is not instantaneous and we can see that in the initial part of the trajectories up until point *"A"* in Figure 7.34a. Until this point, acceleration due to gravity is in the order of 10^{-4}, while accelerations due to SRP and STBE are in the orders of 10^{-7} and 10^{-9} respectively. Although the perturbing magnitudes are small, but the particles in question are extremely small as well and so over time, the perturbing accelerations add up, leading to a significant change in the trajectory from the unperturbed one.

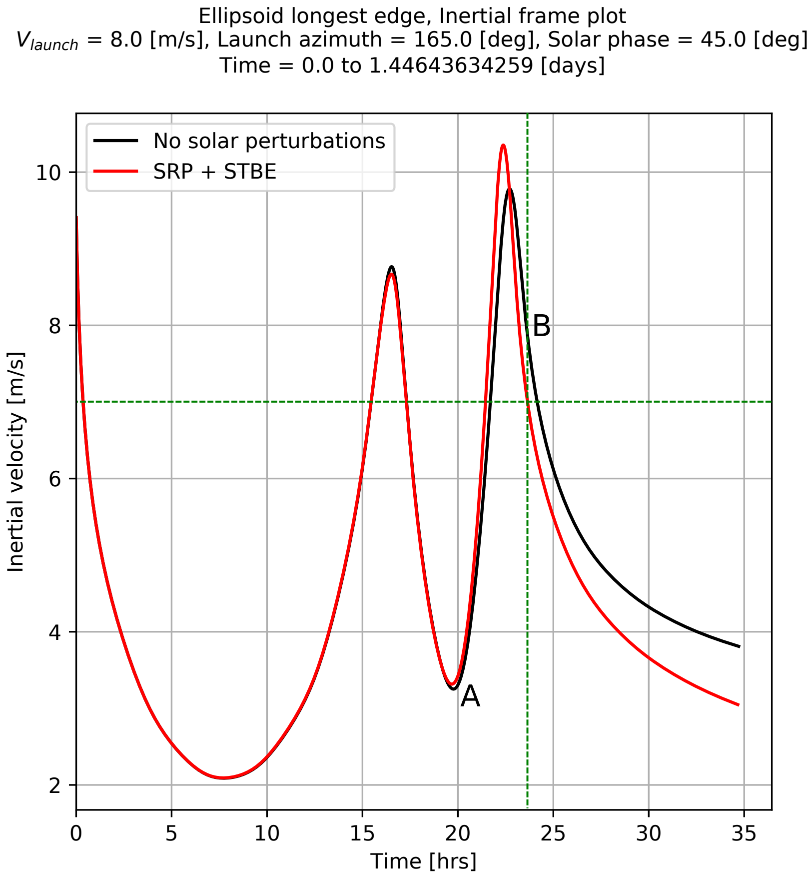

Figure 7.37: Inertial velocity of the perturbed trajectory of capture case 8 in Table 7.2 compared with that of its unperturbed counterpart. The trajectories are shown for the time it takes for the particle in the unperturbed trajectory to escape. Particle code LoGSP-1.

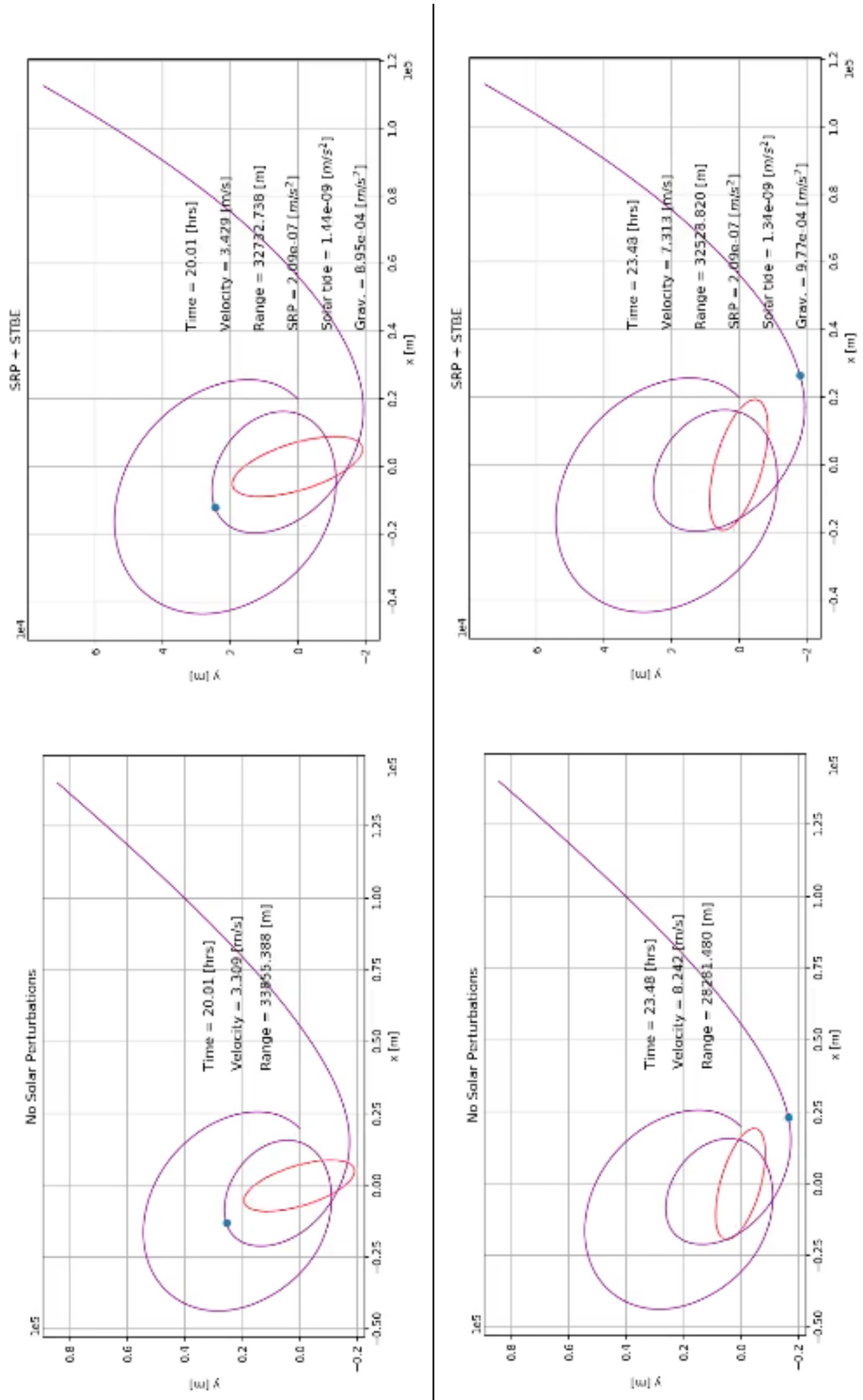

(a) (b)

Figure 7.38: Animation snippets of the inertial frame 2D trajectory (XY plane) of capture regolith for case number 8 in Table 7.2. The bottom two plots are for the case when Solar perturbations were omitted from the simulation and the top two plots includes them. Note the differences in the range to the particle and its velocity for the same time stamp and rotational state of the asteroid. Particle code LoGSP-1.

We see a similar effect when we look at capture case number 5 from Table 7.2. The inertial frame trajectory, both perturbed and unperturbed, for it are shown in Figure 7.39. With Solar perturbations removed from the simulation, the initial conditions for this particle result in it getting launched on a highly elliptical orbit and eventually crashing onto the surface of the asteroid after 96 days. The particle, however, avoids this fate when Solar perturbations are included in the simulation. In Figure 7.39, it can be clearly seen that the direction of the perturbing acceleration due to SRP and STBE is consistent with how the trajectory departs from its unperturbed counterpart. The trajectories are shown only for the time it takes for the particle in the unperturbed trajectory to re-impact the surface of the asteroid. We show this case to highlight the effect perturbations have on a trajectory destined for re-impact, unlike the escape scenario discussed previously. We see drastic changes in the perturbed trajectory from the unperturbed one because when the particle is far away from the asteroid, the perturbing acceleration magnitude is of the same order as that of the gravitational acceleration.

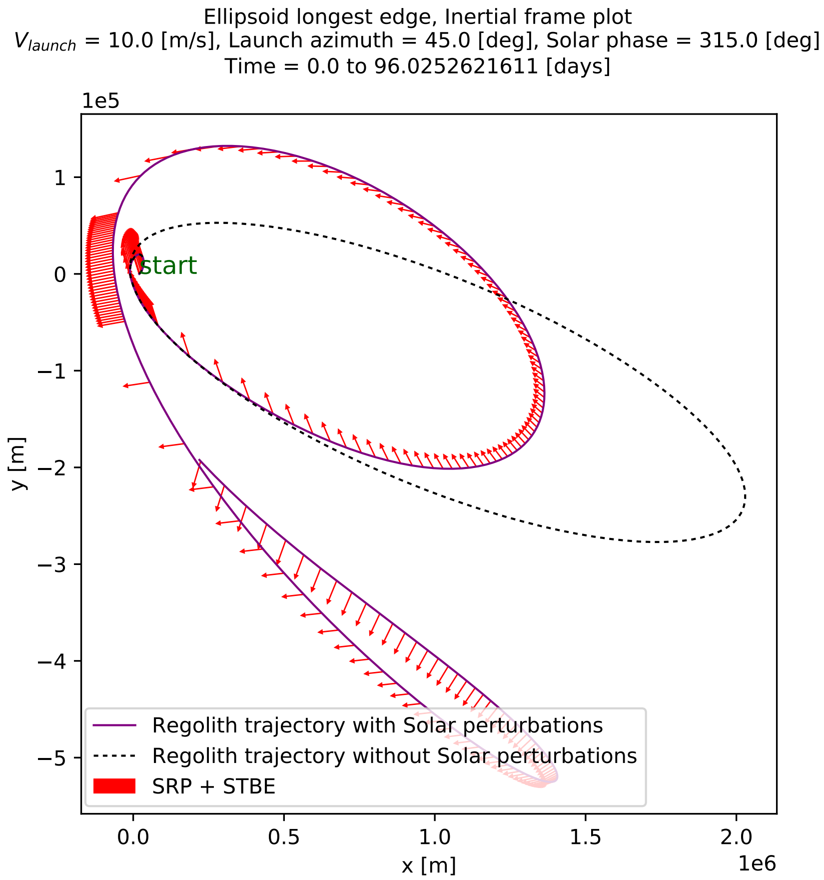

Figure 7.39: Inertial frame 2D trajectory (XY plane) of capture regolith for case number 5 in Table 7.2 with direction of SRP perturbation vector compared with the trajectory of a particle launched with the same initial conditions but in absence of Solar perturbations. Trajectories shown for as long as it takes the unperturbed trajectory Particle code LoGSP-1.

FINAL FATE BEHAVIOR OF DIFFERENT REGOLITH TYPES

For simulations accounting Solar perturbations, the discussion so far has been about how perturbations affect particle motion and specifically the capture scenario, relative to a particle in an unperturbed simulation. We did this detailed analysis for a single particle type only, namely LoGSP-1 from Table 7.1. We shall now look into the final fate behavior of all the regolith types mentioned in

Table 7.1 to understand how particle motion is affected for different densities and sizes. The simulations were conducted one-by-one for each regolith type, in the same manner as described earlier for particle LoGSP-1. All particles were launched from the longest edge of the asteroid.

Part IV

Conclusions & Recommendations

8

CONCLUSIONS

9

RECOMMENDATIONS FOR FUTURE WORK

BIBLIOGRAPHY

Berry, Kevin et al. (2013). “OSIRIS-REx touch-and-go (TAG) mission design and analysis”. In:

Biele, Jens and Ulamec, Stephan (2008). “Capabilities of Philae, the Rosetta lander”. In: *Space Science Reviews* 138.1, pp. 275–289.

Boost. *Numeric Integrators.* Accessed 30 December 2017. URL: `http://www.boost.org/doc/libs/1_66_0/libs/numeric/odeint/doc/html/boost_numeric_odeint/`.

Bottke, William Frederick (2002). *Asteroids III.* University of Arizona Press.

Broschart, Stephen B and Scheeres, Daniel Jay (2005). “Control of hovering spacecraft near small bodies: application to asteroid 25143 Itokawa”. In: *Journal of Guidance Control and Dynamics* 28.2, pp. 343–353.

Carlson, BC (1987). “A table of elliptic integrals of the second kind”. In: *Mathematics of Computation* 49.180, pp. 595–606.

Chobotov, Vladimir A (2002). *Orbital mechanics.* AIAA.

Cunningham, Clifford (2016). *The Discovery of Ceres.* Springer, pp. 25–39.

De Pater, Imke and Lissauer, Jack J (2015). *Planetary sciences.* Cambridge University Press.

Dechambre, D and Scheeres, DJ (2002). “Transformation of spherical harmonic coefficients to ellipsoidal harmonic coefficients”. In: *Astronomy & Astrophysics* 387.3, pp. 1114–1122.

ESA (European Space Agency) (2014). *Missions To Asteroids.* Accessed 31 October 2017. URL: `http://sci.esa.int/rosetta/54342-missions-to-asteroids/`.

Evans, Larry G et al. (2001). “Elemental composition from gamma-ray spectroscopy of the NEAR-Shoemaker landing site on 433 Eros”. In: *Meteoritics & Planetary Science* 36.12, pp. 1639–1660.

Fujiwara, Akira et al. (2006). “The rubble-pile asteroid Itokawa as observed by Hayabusa”. In: *Science* 312.5778, pp. 1330–1334.

Garcia-Yarnoz, Daniel, Sanchez Cuartielles, Joan-Pau, and McInnes, Colin R (2014). “Passive sorting of asteroid material using solar radiation pressure”. In: *Journal of Guidance, Control, and Dynamics* 37.4, pp. 1223–1235.

Garmier, Romain et al. (2002). “Modeling of the Eros gravity field as an ellipsoidal harmonic expansion from the NEAR Doppler tracking data”. In: *Geophysical Research Letters* 29.8.

Jedicke, Robert and Metcalfe, TS (1998). “The orbital and absolute magnitude distributions of main belt asteroids”. In: *Icarus* 131.2, pp. 245–260.

JPL (Jet Propulsion Laboratory). *SSD (Solar System Dynamics).* Accessed 17 November 2017. URL: `http://ssd.jpl.nasa.gov`.

Kargel, Jeffrey S (1994). “Metalliferous asteroids as potential sources of precious metals”. In: *Journal of Geophysical Research: Planets* 99.E10, pp. 21129–21141.

Kawaguchi, Jun’ichiro, Fujiwara, Akira, and Uesugi, Tono (2003). “Hayabusa (MUSES-C)–rendezvous and proximity operation”. In: *56th International Astronautical Congress.*

Keller, Lindsay P and Berger, Eve L (2014). “A Transmission Electron Microscope Investigation of Space Weathering Effects in Hayabusa Samples”. In:

Korycansky, DG and Asphaug, Erik (2004). “Simulations of impact ejecta and regolith accumulation on Asteroid Eros”. In: *Icarus* 171.1, pp. 110–119.

Kubota, Takashi et al. (2006). “Touchdown dynamics for sampling in hayabusa mission”. In: *Proceedings of AIAA/AAS Astrodynamics Specialist Conference and Exhibit 2006.*

Lauretta, Dante S and Team, OSIRIS-Rex (2012). “An overview of the OSIRIS-REx asteroid sample return mission”. In: *Lunar and Planetary Science Conference.* Vol. 43.

Lauretta, DS et al. (2015). “The OSIRIS-REx target asteroid (101955) Bennu: Constraints on its physical, geological, and dynamical nature from astronomical observations”. In: *Meteoritics & Planetary Science* 50.4, pp. 834–849.

Lee, Pascal (1996). “Dust levitation on asteroids”. In: *Icarus* 124.1, pp. 181–194.

MacMillan, William Duncan (1958). *The theory of the potential.* Dover.

Malhotra, Renu and Wang, Xianyu (2016). “Eccentricity distribution in the main asteroid belt”. In: *Monthly Notices of the Royal Astronomical Society* 465.4, pp. 4381–4389.

McCoy, TJ et al. (2001). “The composition of 433 Eros: A mineralogical—chemical synthesis”. In: *Meteoritics & Planetary Science* 36.12, pp. 1661–1672.

Miller, James K et al. (2002). “Determination of shape, gravity, and rotational state of asteroid 433 Eros”. In: *Icarus* 155.1, pp. 3–17.

Miyamoto, H et al. (2006). “Regolith on a tiny asteroid: Granular materials partly cover the surface of Itokawa”. In: *37th Annual Lunar and Planetary Science Conference.* Vol. 37.

Morbidelli, Alessandro et al. (2000). “Source regions and timescales for the delivery of water to the Earth”. In: *Meteoritics & Planetary Science* 35.6, pp. 1309–1320.

Morrow, Esther, Scheeres, Daniel J, and Lubin, Dan (2001). “Solar sail orbit operations at asteroids”. In: *Journal of Spacecraft and Rockets* 38.2, pp. 279–286.

Müller, TG et al. (2017). “Hayabusa-2 mission target asteroid 162173 Ryugu (1999 JU3): Searching for the object’s spin-axis orientation”. In: *Astronomy & Astrophysics* 599, A103.

NASA (National Aeronautics and Space Administration). *Asteroids: In depth.* Accessed 17 November 2017. URL: `https://solarsystem.nasa.gov/planets/asteroids/indepth`.

— *SKG (Strategic Knowledge Gaps).* Accessed 20 November 2017. URL: `https://www.nasa.gov/exploration/library/skg.html`.

Nittler, Larry R et al. (2001). “X-ray fluorescence measurements of the surface elemental composition of asteroid 433 Eros”. In: *Meteoritics & Planetary Science* 36.12, pp. 1673–1695.

Panou, Georgios (2014). “The gravity field due to a homogeneous triaxial ellipsoid in generalized coordinates”. In: *Studia Geophysica et Geodaetica* 58.4, pp. 609–625.

Prockter, L et al. (2002). “The NEAR shoemaker mission to asteroid 433 eros”. In: *Acta Astronautica* 51.1, pp. 491–500.

Reimond, Stefan and Baur, Oliver (2016). “Spheroidal and ellipsoidal harmonic expansions of the gravitational potential of small Solar System bodies. Case study: Comet 67P/Churyumov-Gerasimenko”. In: *Journal of Geophysical Research: Planets* 121.3, pp. 497–515.

Richter, K and Keller, HU (1995). “On the stability of dust particle orbits around cometary nuclei”. In: *Icarus* 114.2, pp. 355–371.

Robinson, MS et al. (2001). “The nature of ponded deposits on Eros”. In: *Nature* 413.6854, pp. 396–400.

Romain, Garmier and Jean-Pierre, Barriot (2001). “Ellipsoidal harmonic expansions of the gravitational potential: theory and application”. In: *Celestial Mechanics and Dynamical Astronomy* 79.4, pp. 235–275.

Schaub, Hanspeter and Junkins, John L (2003). *Analytical mechanics of space systems.* AIAA.

Scheeres, Daniel J (2016). *Orbital motion in strongly perturbed environments: Applications to asteroid, comet and planetary satellite orbiters.* Springer.

Scheeres, Daniel J et al. (1996). “Orbits close to asteroid 4769 Castalia”. In: *Icarus* 121.1, pp. 67–87.

Scheeres, DJ and Marzari, F (2000). “Temporary orbital capture of ejecta from comets and asteroids: Application to the Deep Impact experiment”. In: *Astronomy and Astrophysics* 356, pp. 747–756.

Scheeres, DJ, Durda, DD, and Geissler, PE (2002). “The fate of asteroid ejecta”. In: *Asteroids III*, pp. 527–544.

Tsuda, Yuichi et al. (2013). “System design of the Hayabusa 2—Asteroid sample return mission to 1999 JU3”. In: *Acta Astronautica* 91, pp. 356–362.

Veverka, J et al. (2001a). "Imaging of small-scale features on 433 Eros from NEAR: Evidence for a complex regolith". In: *Science* 292.5516, pp. 484–488.

Veverka, J et al. (2001b). "The landing of the NEAR-Shoemaker spacecraft on asteroid 433 Eros". In: *Nature* 413.6854, pp. 390–393.

Weisstein, Eric W. *Cubic Formula*. Accesed on 4 December 2017. MathWorld–A Wolfram Web Resource. URL: `http://mathworld.wolfram.com/CubicFormula.html`.

Werner, Robert A and Scheeres, Daniel J (1996). "Exterior gravitation of a polyhedron derived and compared with harmonic and mascon gravitation representations of asteroid 4769 Castalia". In: *Celestial Mechanics and Dynamical Astronomy* 65.3, pp. 313–344.

Yano, H et al. (2004). "Sampling Strategy and Curation Plan of" Hayabusa" Asteroid Sample Return Mission". In: *Lunar and Planetary Science Conference*. Vol. 35.

Yano, Hajime et al. (2006). "Touchdown of the Hayabusa spacecraft at the Muses Sea on Itokawa". In: *Science* 312.5778, pp. 1350–1353.

Yárnoz, D García, Cuartielles, JP Sánchez, and McInnes, Colin R (2014). "Passive sorting of asteroid material using solar radiation pressure". In: *Journal of Guidance, Control, and Dynamics*.

Yu, Yang and Baoyin, Hexi (2012). "Orbital dynamics in the vicinity of asteroid 216 Kleopatra". In: *The Astronomical Journal* 143.3, p. 62.

Appendices

A
EXTRA FIGURES

This appendix contains figures which are used to support the explanation of certain results, arguments and conclusions in the main part of the Thesis report.

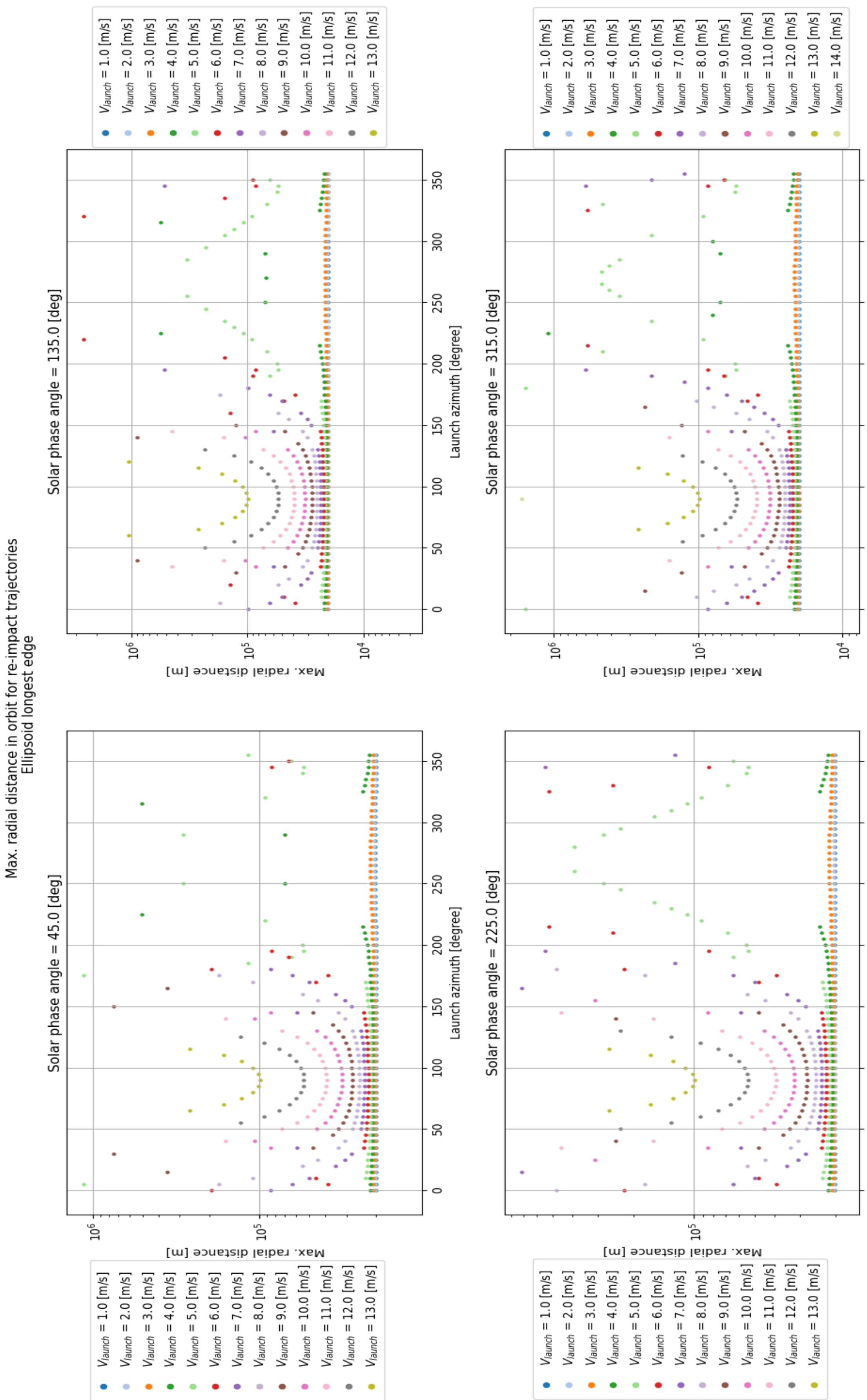

Figure A.1: Maximum radial distance (from the centre of the asteroid) attained by the regolith in orbit for different launch velocities and launch azimuths. The particles were launched from the longest edge of the ellipsoid (asteroid). Plots are for particle code LoGSP-1 and only for the re-impact scenario.

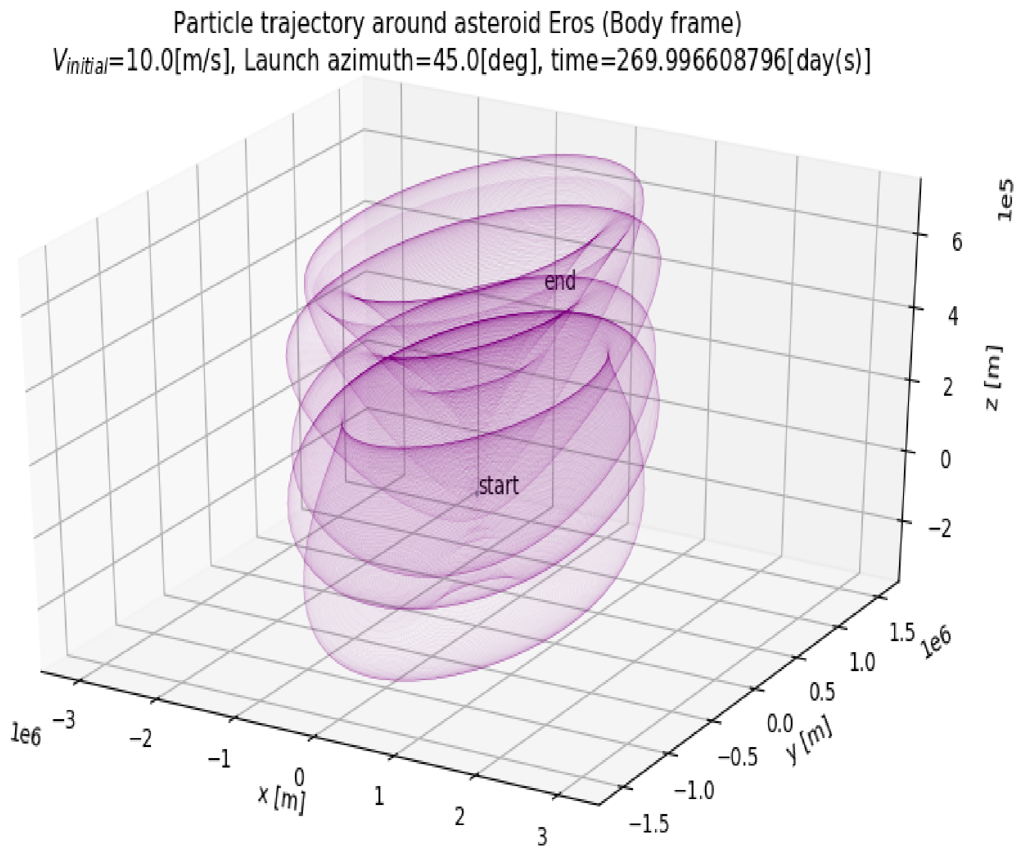

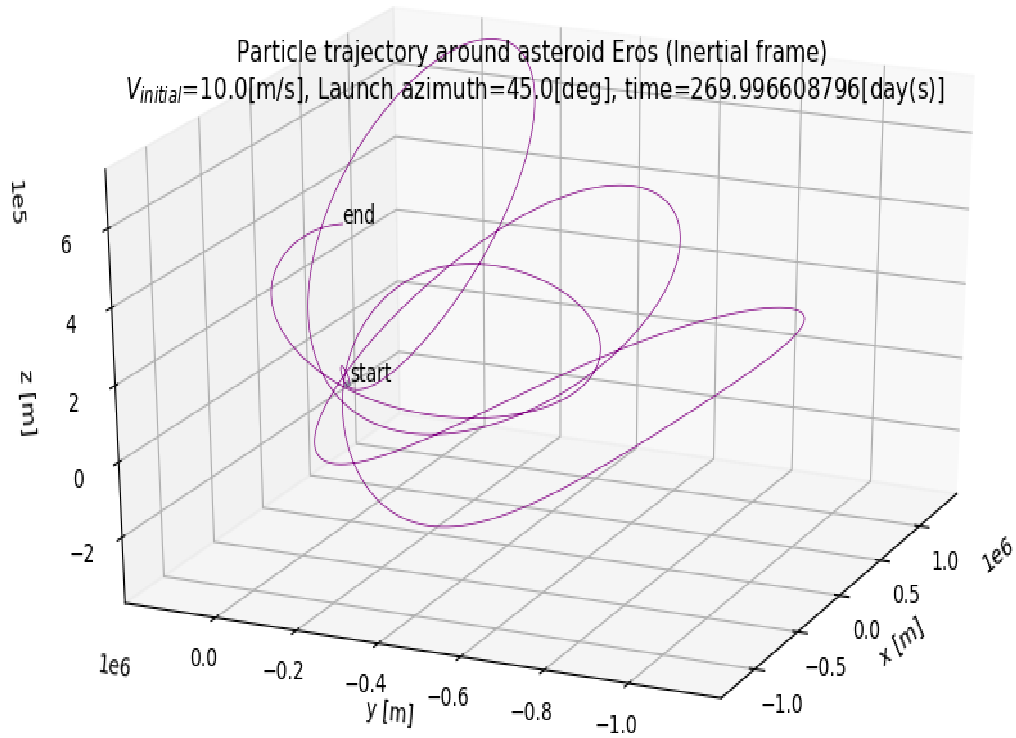

Figure A.2: 3D trajectory of capture regolith for case number 5 in Table 7.2. Particle code LoGSP-1.

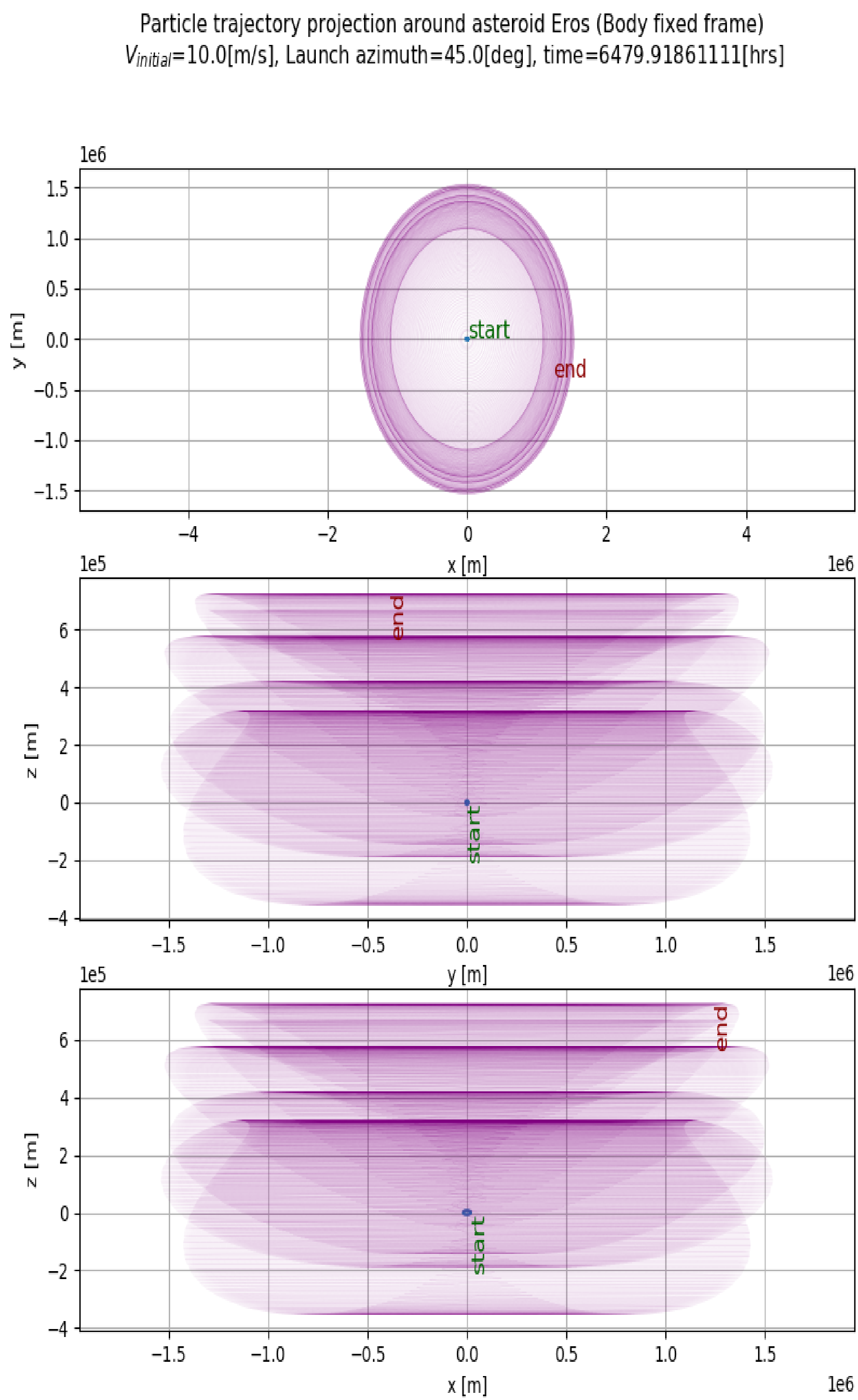

Figure A.3: 2D rotating frame trajectory of capture regolith for case number 5 in Table 7.2. Particle code LoGSP-1.

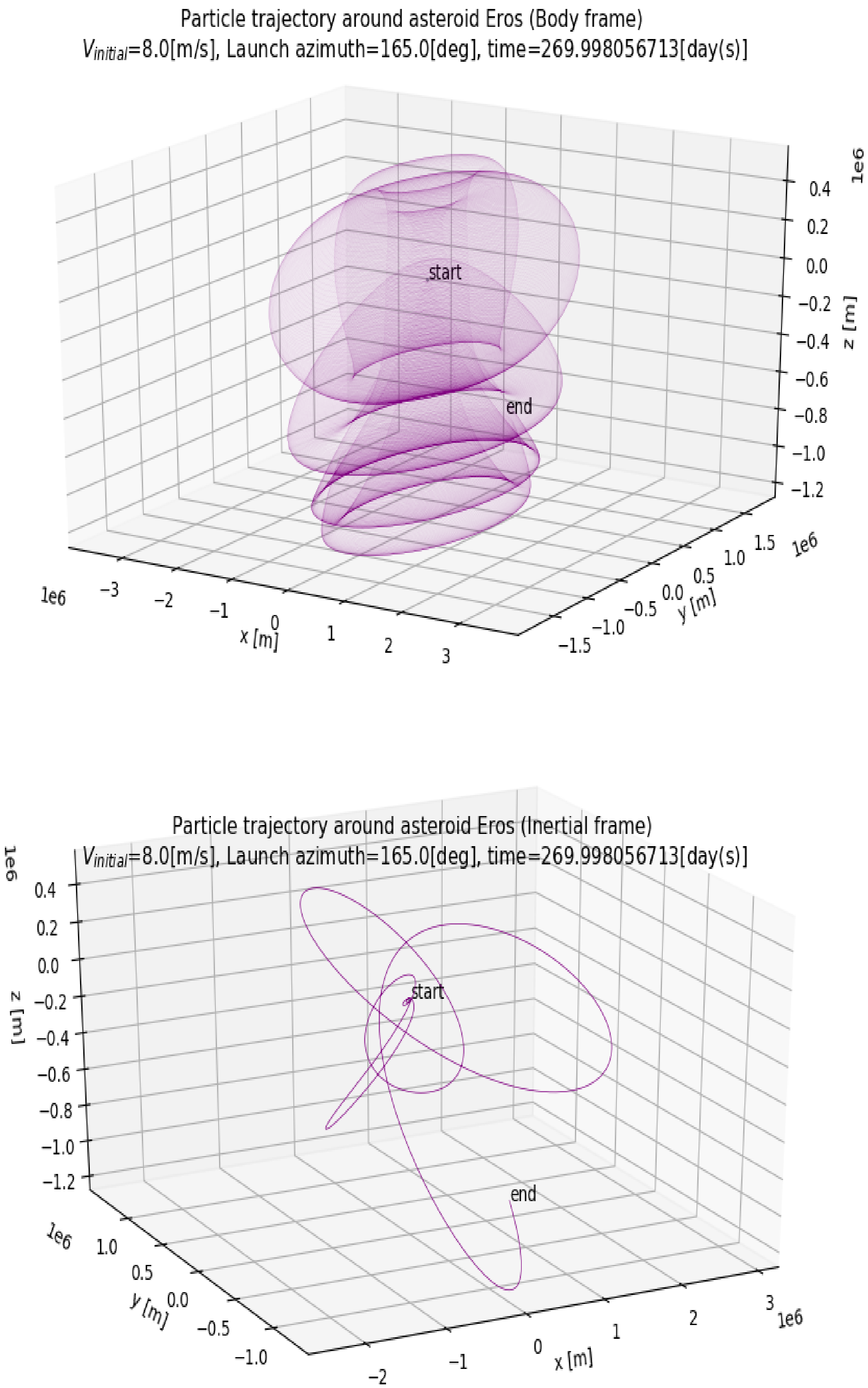

Figure A.4: 3D trajectory of capture regolith for case number 5 in Table 7.2. Particle code LoGSP-1.

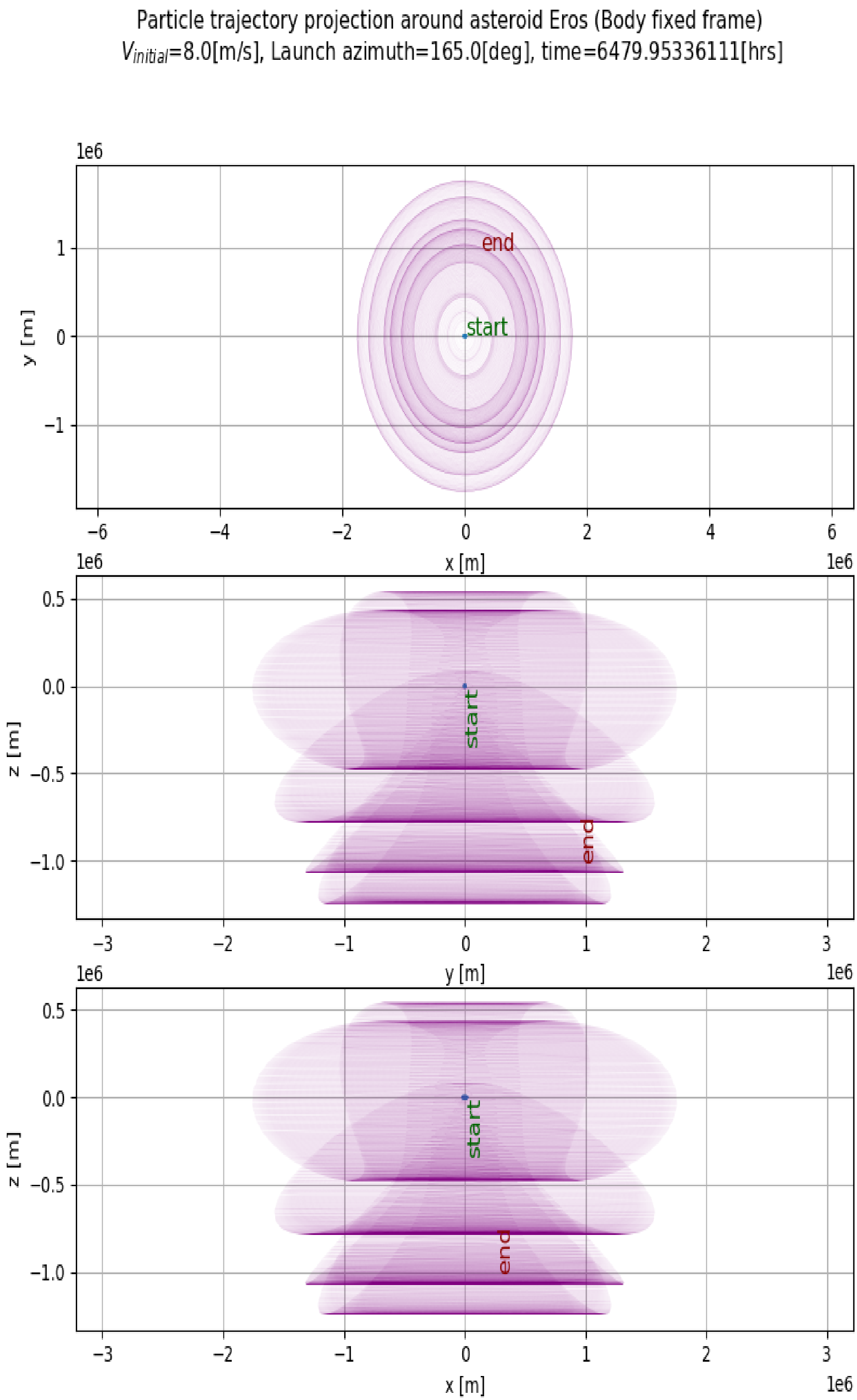

Figure A.5: 2D rotating frame trajectory of capture regolith for case number 8 in Table 7.2. Particle code LoGSP-1.